Title

Pre-Assembly of Shape-Designed Colloidal Crystals and Polymers in Fluctuating Brownian Monolayers

Author

YU, Tianren

Publication Date

2023

UNIVERSITY OF CALIFORNIA

Los Angeles

Pre-Assembly of Shape-Designed Colloidal Crystals and Polymers in Fluctuating Brownian Monolayers

A dissertation submitted in partial satisfaction of the requirements for the degree Doctor of Philosophy in Chemistry

by

Tianren Yu

2023

ABSTRACT OF THE DISSERTATION

Pre-Assembly of Shape-Designed Colloidal Crystals and Polymers in Fluctuating Brownian Monolayers

by

Tianren Yu
Doctor of Philosophy in Chemistry
University of California, Los Angeles, 2023
Professor Thomas G. Mason, Chair

Many natural systems are assembled from the ordering of complex shapes. Understanding the role of shapes of fundamental building blocks is crucial in elucidating both microscopic and macroscopic behavior of condensed matter, such as polymers and crystals. We study pre-assembly of colloidal particles as model systems for molecules. These colloidal particles are large enough to be readily available for real-time observation using optical microscopy with high enough resolution for sub-particle image processing and particle tracking, yet small enough to undergo significant entropic Brownian fluctuations. Top-down pre-assembly provides several advantages over self-assembly since patterns are highly customizable, massively producible and have low defect rates. We use photolithography to produce pre-configured colloidal lithographic tiles. These tiles have nearly hard interactions, undergo 2D Brownian motion in monolayers when released in liquid dispersion and stabilized via surfactants. Such monolayer is maintained by depletion attraction. In particular, we design and fabricate lithographic polymers that are coupled together by lock-and-key steric linkages both in experiments and in simulation. These steric bonds exhibit unusual extensibilities and chiralities depending on custom-design. We also make 2D seven-fold quasi-crystals consisting of three different kinds of tiles. This quasi-crystal pattern undergoes a new heptatic liquid crystal phase, and shows heterogeneity of order and dynamics of different constituent particles. Our findings enrich understanding in shape-structure relationship for new types of polymers having steric bonds and hierarchical assemblies with unusual symmetries.

The dissertation of Tianren Yu is approved.

Louis-Serge Bouchard

William M. Gelbart

Jose Alfonso Rodriguez

Thomas G. Mason, Committee Chair

University of California, Los Angeles

2023

To my family, friends, and people who have supported me.

TABLE OF CONTENTS

Chapter 3 – Shape-Controlled Extensibility and Chirality of Semi-Flexible Steric Lock-and-Key Polymers……………………………………………47

LIST OF FIGURES

Acknowledgements

This painstaking yet joyful journey towards completing the dissertation and Ph. D. degree cannot be possible without the support and encouragement of many individuals and organizations. I would like to express my sincere appreciation to those who have helped me during the past five years.

Most importantly, I would like to thank my Ph.D. advisor, Prof. Thomas G. Mason. I am privileged for having spent one of the best periods of time in my life working with Prof. Mason on curiosity-driven scientific research. As an experienced scientist and a great advisor, he provides invaluable practical and intellectual advice not only in research but also in life. With his exceptional guidance and support, I always feel encouraged and motivated while I am pursuing my Ph. D. at UCLA.

I would like to thank my committee members, Prof. William Gelbart, Prof. Louis Bouchard, and Prof. Jose Rodriguez who provided precious academic advice and strong support in committee meetings and towards dissertation.

I would like to thank Dr. Lorna Tokunaga and other CNSI staff who opened the door to and guided me through the fascinating world of microfabrication. I greatly appreciate their expertise as skillful engineers and patience as persuasive mentors.

It is my pleasure to work with Dr. Yixuan Xu, Dr. Ha Seong Kim, Dr. Matthew Pagenkopp, Edgar Elias and Shang-Lin Tsai in Prof. Mason’s lab. I have learnt a lot from and enjoyed the chemistry with all of you. We will always be proud as members of ‘Team Mason’

in our lives.

I would like to thank Dr. Yung-Ya Lin who was my advisor in my first year. I would not have the chance to study at UCLA without his extraordinary support. I am also grateful to Prof. Gelbart, Prof. Schwartz, and Prof. Bouchard for their help and advice when I was seeking a new lab.

I would like to thank the hospitality of UCLA and the people in this country, especially during the pandemic when we were physically isolated. I believe that science promotes mutual understanding and welfare for all.

I would like to thank the financial support from China Scholarship Council (CSC) and National Science Foundation (NSF).

The following chapters are versions of the corresponding publications: Chapter - 2, T. Yu and T. G. Mason, Brownian lithographic polymers of steric lock-and-key colloidal linkages. *Sci. Adv.* **7**, eabg3678 (2021); Chapter - 3, T. Yu and T. G. Mason, Shape-controlled extensibility and chirality of semi-flexible steric lock-and-ley polymers, *submitted*; Chapter – 4, T. Yu and T. G. Mason, Heptatic liquid seven-fold quasi-crystals by lithographic colloidal pre-assembly, *submitted*. Portions of this dissertation have been copyrighted previously by the authors in these listed works and are used with permission. Anyone wishing to reproduce any portion of the herein dissertation that is also found in one of these works should contact the respective journals and authors to obtain appropriate permission.

VITA

2018	Bachelor of Science, Nanjing University, Jiangsu, China
2022	Dissertation Year Fellowship, University of California, Los Angeles, CA, USA.

PUBLICATIONS

1. T. Yu and T. G. Mason, Brownian lithographic polymers of steric lock-and-key colloidal linkages. *Sci. Adv.* **7**, eabg3678 (2021)
2. T. Yu and T. G. Mason, Shape-controlled extensibility and chirality of semi-flexible steric lock-and-ley polymers, *submitted.*
3. T. Yu and T. G. Mason, Heptatic liquid seven-fold quasi-crystals by lithographic colloidal pre-assembly, *submitted*

Chapter 1 – Introduction

The importance of direct imaging and real-time tracking of individual atoms and molecules cannot be overstated by virtue of understanding the underlying mechanisms of phase and dynamical behavior. Examples such as grain boundary deformation in metals (1) and the glass transition in silica (2) have been reported using aberration-corrected transmission electron microscopy (ac-TEM) in recent years. However, a very thin layer of conductive substrate is required, and high energy electron beam damage is a pressing concern especially for soft, morphologically diverse molecules. As a result, an alternative way to circumvent these limitations, and also go beyond existing examples to shape-designed crystals and polymers, by studying larger particles but with structural similarities – colloids – is both feasible and insightful.

Colloidal particles typically have sizes from a few nanometers to about 10 microns. This size range offers unique advantages for assemblies and dispersions of colloids as model systems to study similar phenomena of their molecular counterparts, such as polymers and crystals (3). First, colloidal particles are large enough that they can be treated by classical theories, and those larger than a few hundred nanometers can be observed using an optical microscopy (4). Although numerous methods, such as electron (5), X-ray (6), and stimulated emission-depletion microscopy (7), have been implemented to overcome the diffraction limit of visible light, these methods still suffer from either low frame acquisition rates or small fields of view. Second, colloidal particles are also small enough that they undergo significant random Brownian motion in dispersion while exploring accessible microstates that maximize the system's entropy by the second law of thermodynamics. According to Einstein's theory, the root-mean-square displacement of a colloidal particle (~1 μm) subject to Brownian fluctuations is about 1 μm in one second (8). Therefore, this spatial and temporal scale of dynamics for colloids about micrometer size enable readily accessible, real-time tracking of each individual particle using optical microscopy over a large field of view and a long period of time. It is now possible to track many particles simultaneously with the help of computer-based image analysis.

In this dissertation, we will focus on the equilibrium and non-equilibrium properties of shape-designed colloidal polymers and crystals that both mimic and go beyond their molecular counterparts. We study the lock-and-key steric bonding between constituent colloidal monomers both in experiments and simulations. These highly controllable and flexible linkages provide unconventional extensibilities as well as chiralities. We also reveal a new heptatic phase, and heterogenous dynamics and order in seven-fold quasi-crystals consisting of three different rhombic building tiles. These new colloidal polymers and crystals rely on top-down photolithographic pre-assembly of prism-like tiles in monolayers; these tiles have effectively hard in-plane interactions. Modern wide- and flat-field, high-resolution, time-lapse optical digital microscopy make post-processing particle tracking of hundreds to thousands of particles in a dense monolayer at sub-particle resolution practicable.

1.1 Shape-Designed Colloids with Hard Interactions

Nature is ubiquitously filled with and assembled from a diverse variety of complex shapes. Minerals form beautiful geometric shapes according to lattice structures; cells have particular shapes, such as dendritic neurons, which facilitate certain biological functions; Scientists have also fabricated numerous nano- and micro-scale assemblies with different shapes (9-13). Understanding the role of shapes in formation and properties of these assemblies are crucial, yet challenging because these processes are often coupled together with other factors, such as attractive forces. As a result, hard interactions between building blocks are desirable when one wishes to isolate and study the effects of core-shape and geometry (14, 15).

Charge-stabilized colloidal dispersions are subject to both van der Waals attractive and electrical repulsive forces, as explained by Derjaguin-Landau-Vervey-Overbeek (DLVO) theory (16). Initially uncharged polymeric colloids can be stabilized in dispersions using an adsorbed charged surfactant, such as dodecyl sulfate surfactant anions (DS-). The adsorption of DS- on the surface of colloids effectively increases the strength of the repulsive energy barrier. In practical scenarios, such screen-charged repulsions are typically short-ranged, having Debye lengths of a few nanometers. Therefore, the interactions among colloids having sizes of a few microns can typically be considered as nearly hard.

Hard interactions are implemented by particle-overlap collision detection, which enforces volume exclusion in colloidal assemblies. In condensed phases such as colloidal crystals and liquids, the shapes of constituent building blocks, as well as particle volume/area fraction ϕ, which is analogous to the inverse temperature in molecular systems (3), strongly affect the behavior of a given particular system. Various models, such as the translational-rotational cage model for crosses (11, 14), x-oid model for regular polygons (17), local polymorphic configuration (LPC) model for Penrose kites (18), and entropic directional forces calculation (19) have been proposed to explain phase behavior based on geometry and density analysis. In free-standing dynamical colloidal polymers of steric linkages, bonding potentials can be deduced from accessible phase space by collision detection depending on the geometric design (20). In addition, non-equilibrium behaviors may also depend on other factors, such as the rate of crowding (18) or initial configuration (20).

Investigations on different shapes of building blocks have revealed crucial roles of geometry both during assembly process and in assembled systems having nearly hard interactions. Comprehensive experimental and simulation work have shown the dependence of melting transitions of 2D colloidal crystals on the shapes of constituent regular *n*-polygon tiles (21). Assemblies of concave shapes show interesting phase behavior upon dense packing (22). Sub-particle protrusions such as arms in square crosses (11), or even shape-complementary dimerization interactions such as annular sector particles (23), are critical in these processes. The translational entropy gain from more accessible space as a result of alignment supersedes the rotational entropy loss because of alignment by shape complementary or corrugation towards crystallization. Less regular shapes, such as Penrose kites, are trapped in glass state upon crowding because of structural frustration by diverse LPCs (18); whereas, pre-assembled Penrose kites and darts show a new pentatic liquid quasi-crystal phase (24). Even more complex, multi-particle, hierarchical assemblies, such as seven-fold quasi-crystals consisting of three types of building blocks, could show richer dynamical and structural phenomena, although such seven-fold quasi-crystals have not been achieved experimentally prior to the studies that we present herein. Similarly, studies of free-standing colloidal polymers, connected by pre-assembled, geometrically designed, steric linkages exhibiting hard interactions were likewise limited before this dissertation. Such steric lock-and-key colloidal polymers can serve as model systems for understanding the role that shape plays in mechanically interlocked molecules (MIMs) (25). Therefore, we have developed colloidal polymers with lock-and-key steric linkages that rely on purely hard interactions to study the effect of shapes on polymeric properties both in experiments and simulations.

1.2 Colloidal Assembly

Bottom-up self-assembly and top-down directed-assembly are two distinctly different yet potent methods for creating multi-scale materials. Until the work that we present herein, self-assembly has been the primary method used to form colloidal polymers. In this self-assembly scenario, colloidal monomers diffuse, contact, and form multimers via attractive force of various origins; multimers continue to proliferate to form polymers. For instance, microscopic artificial swimmers have been assembled from specific non-covalent biotin–streptavidin interaction that couple the dibiotin-DNA bridge and streptavidin-coated magnetic particles together (26). Assembly of gold nanorods has been induced by photoactive covalent bonding reactions of macromolecular tethers on both ends of each nanorod (27). Entropic forces, such as the depletion attraction (28), also can facilitate self-assembly of colloidal polymers.

The depletion attraction is a force that primarily exists in colloidal multi-component dispersions, where larger particles experience an effective attractive force because of the presence of smaller particles, known as depletants or depletion agents (**Fig. 1.1A**). The depletion attraction can be understood as an entropy maximization process. Larger particles (cyan) have excluded volume (gray) within which the presence of smaller particles (orange) is prohibited sterically. When larger particles approach each other, their excluded volumes overlap, creating an overlapping excluded volume (purple). The presence of overlapping

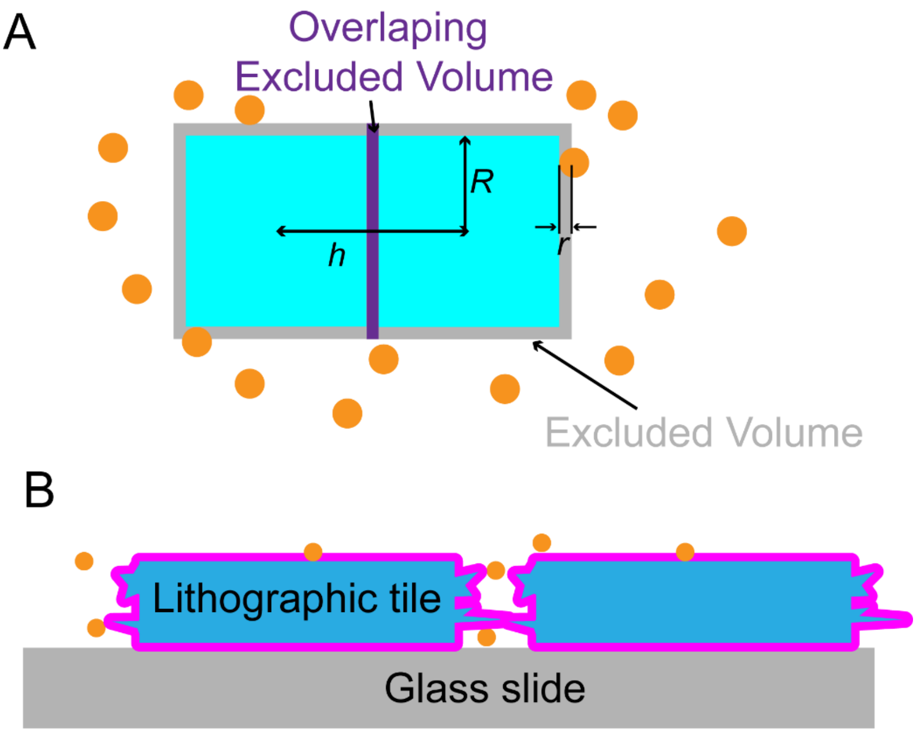

Figure 1. 1. Classic depletion attraction between spheres and roughness-controlled depletion attraction (RCDA) of prismatic lithographic tiles in a monolayer. (A) Illustration of depletion attraction in binary colloidal dispersions of hard spheres. In such dispersion, larger particles (square, cyan) with edge length $2R$ have excluded volume (gray) where smaller particles (orange) with radius r cannot enter. Larger particles tend to approach each other (distance $h < 2R+2r$) to create overlapping excluded volume (purple) that increases the free space for smaller particles to explore for entropy maximization purposes. (B) Strength of depletion attraction depends on surface roughness. When in-plane rough surfaces approach each other, less overlapping excluded volume is created, compared with two smooth surfaces that approach each other vertically. Therefore, in-plane attraction is suppressed while vertical attraction is enhanced. As a result, the platelet (blue) stays above the smooth glass slide in a monolayer without in-plane aggregation.

excluded volume increases free space for smaller particles to explore, so the system's entropy is maximized (29).

The strength of the depletion attraction depends on both the shape and surface roughness of larger particles. For example, for flat-convex colloidal disks and concave-convex pac-man like concave building colloidal dispersions, depletion attractions between shape-complementary sites are stronger (30). Therefore, lock-and-key colloids are self-assembled as a result of anisotropic attractive forces (31, 32). Also, rough surfaces exhibit smaller overlapping excluded volumes when they approach each other, compared with smooth surfaces (**Fig. 1.1B**). Therefore, the depletion attraction is typically stronger between smooth surfaces compared to surfaces with random sparse asperities, although periodic shape-complementary corrugations on surfaces have been demonstrated to enhance the depletion attraction, as compared to smooth surfaces. Custom-shaped microscale platelets having smooth horizontal sides but rough vertical sides can form columnar stacks through roughness-controlled depletion attractions (33). Overall, in prior work, colloidal polymers have not been pre-configured in top-down manner but rather through self-assembly from dispersed components through induced attractions.

Beyond colloidal polymers, colloidal crystals can be self-assembled from soft particles via attractive interactions. For example, each building block contains a nanocrystal core and surface ligands; they order into superlattice through van der Waals attraction between ligands when solvent is evaporated or destabilized (34). The lattice structure is dependent on the shape of the nanocrystal core, such as a sematic-like superlattice from rod-shaped Au particle (35), and inter-locking network structure from octa-pod shaped CdSe-CdS particle (36). Rich variety of crystal structures can be assembled from programmable DNA-coated colloids via complementary base pairing (37). For hard particles, the self-assembly into crystals are dominated by entropy through slow crowding process, which only depends on the concentration and shape, such as the isotropic-nematic transition of rod-like particles (38).

Still, self-assembly has several limitations in forming colloidal crystals, especially for complex shaped, multi-component, or hierarchical structures. The production rate is slow, the crystalline area is small, and defects are common. Alternatively, top-down directed assembly methods have been developed to address these limitations. Magnetic (39), electric (40), and optical (41) fields have been applied to manipulate the delicate directed assembly of colloidal crystals.

1.3 Lithographically Pre-Assembled Monolayers (Litho-PAMs)

Modern optical stepper lithography provides a way of precisely custom-designing colloidal-scale assemblies down to sub-particle nanoscopic features. Here, we use the method of lithographically pre-assembled monolayers (litho-PAMs) (24) to create shape-designed 2D colloidal crystals and polymers of mobile pre-configured tiles that undergo Brownian fluctuations after release from the lithographic substrate. The photolithographic procedure is as follows **(Fig. 1.2A**). First, digitally designed patterns are converted into a photomask using computer-aided-design software. Second, a substrate, such as a smooth, double-polished glass wafer, is spin-coated with a thin sacrificial layer of Omnicoat and subsequently a thicker photoresist layer of SU-8. Third, UV light shines through the photomask in a 5x reduction stepper (*e.g.* ASML Hg i-line stepper) onto the wafer, inducing a photo-chemical cross-linking reaction in the exposed photoresist. Fourth, such photo-chemical crosslinking reaction is enhanced during a post-bake step (making the exposed area insoluble in the developer solution), and the unexposed area is removed in the development process, yielding the desired pattern formed out of photoresist on the sacrificial layer above the wafer's surface. Finally, a descumming process using an oxygen plasma is applied to remove residues of SU-8 between particles and to modify the particle area fraction through erosion.

Per the method of litho-PAMS, to release the SU-8 particle tiles from the Omnicoat, we

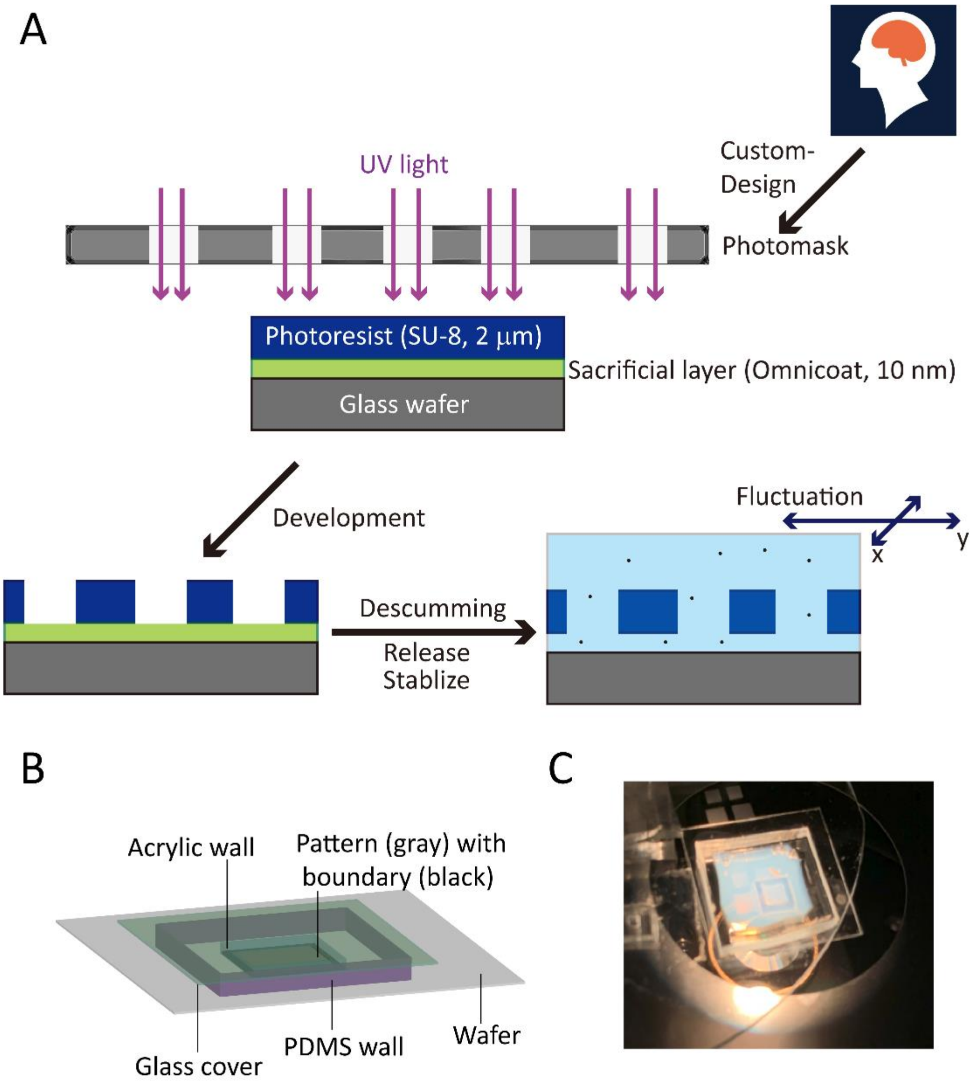

Figure 1. 2. Lithographically Pre-Assembled Monolayers. (A) Lithographic production and release in 2D. Digitally designed pattern are transformed onto a photomask. A glass wafer is first coated with Ominicoat as a sacrificial layer (10 nm thick) and subsequently with SU-8 2002 (2 μm thick) as the photoresist. UV light shines through the photomask, transferring the pattern from the photomask onto the wafer by inducing photo-chemical reactions on the exposed area of the photoresist. After post bake, exposed areas of SU-8 become insoluble. Therefore, unexposed areas are dissolved and removed by SU-8 developer, leaving the patterned SU-8 tiles on the wafer. Mild descumming procedure is applied to remove any residue. Lithographic tiles are released by dissolving the sacrificial layer with TMAH, stabilized with SDS and kept in 2D by RCDA with polystyrene spheres (~40nm dia.) because of the roughness difference on the vertical and horizontal sides (**Fig. 1.1B**). (B) A schematic illustration of experimental set-up. The releasing area is confined by a PDMS wall and covered by a glass cover to prevent evaporation. An acrylic wall is put on the pattern boundary to preserve the area fraction for 7-fold quasi-crystal. (C) Experimental set-up with inverted optical microscope. Time-lapse is taken by a high-resolution camera.

use a release solution-dispersion (RSD). This RSD achieves several different purposes simultaneously. It releases the pre-assembled tiles from the wafer in a region confined by PDMS wall, by dissolving the sacrificial layer using a base, stabilizes the interparticle interactions by adsorption of DS- onto particle surfaces, and keeps the tiles in 2D plane by RCDA induced by nanoscale spheres, because the vertical surface is inherently rougher than the bottom surface of the lithographic tiles and also the surface of the polished glass wafer. We use an additional acrylic wall to pin the printed photoresist boundary down to keep the designed area fraction in certain experiments involving a seven-fold quasi-crystal (**Figs. 1.2B** and **1.2C**).

1.4 Summary

In this dissertation, we use litho-PAMs to fabricate pre-assembled colloidal polymers and quasi-crystals having unusual geometries, structures, and properties that would otherwise be extremely difficult or impossible to synthesize using molecular counterparts. We study how pre-assembled, shape-designed particles would affect the behavior of these many-particle systems through real-time visualization of Brownian fluctuations using optical microscopy. Our findings enrich the understanding of shape-structure relationships of new types of polymers with steric bonds and of hierarchical quasi-crystals with unusual symmetries. This dissertation is organized as follows.

In chapter 1, we create colloidal polymers consisting of custom-shaped, mobile microscale tiles that are connected by steric lock-and-key structure, forming flexible bonds between separate tiles. This versatile method enables us to produce and examine various complex structures such as curved, branching, spiral-bridged, dendrimer-like, and mesh-like polylithomers with adjustable pre-assembled features like dimensions, topologies, configurations, intrinsic local curvatures, persistence lengths, and bond extensibilities. By monitoring the dynamics in the polylithomers due to Brownian fluctuations at the monomer level, we discover remarkably high bond extensibilities that are directly dependent on the particle design.

In chapter 2, through simulations we further investigate polylithomers having a more diverse range of steric lock-and-key bonds, which can be designed to have extensional sliding, chiral asymmetry, and even split bond angles. We determine phase spaces of bond angles and insertion distances of these hard-interacting monomers by collision detection. We analyze and measure conformational statistics of these colloidal polymers generated by self-avoiding Monte Carlo growth, and compute their equilibrium polymeric properties, such as chiral-corrected persistence length, end-to-end distances, and radii of gyration, extensibility-correlated spatial pair correlation function, and bifurcation-correlated conformational fluctuations. Our simulations demonstrate that this broad spectrum of steric bonds can result in unconventional conformations that extend the scope of polymer behavior beyond traditional molecular polymers.

In chapter 3, we design and fabricate pre-configured 2D seven-fold quasi-crystal with distinct area fractions through different lithographic and descumming process. This quasi-crystal consists of three different types of rhombic tiles. This quasi-crystal pattern exhibits a new heptatic phase, and shows heterogeneity in dynamics and degree of order of different constituent particles at different scales. We observe rich tile dynamics and motif dynamics, such as collective rotation of non-corrugated motifs assembled from corrugated particles that partially destroy the long-range orientational superstructural order even at very high density. We also develop a edge-proximity tessellation method based on the equal distance to edges instead of centers to analyze the evolution of nearest neighbors during melting for non-compact particles.

Reference

1. L. Wang *et al.*, Tracking the sliding of grain boundaries at the atomic scale. *Science* **375**, 1261-1265 (2022).
2. P. Y. Huang *et al.*, Imaging atomic rearrangements in two-dimensional silica glass: Watching silica's dance. *Science* **342**, 224-227 (2013).
3. K. Zhao, T. G. Mason, Assembly of colloidal particles in solution. *Rep. Prog. Phys.* **81**, 126601 (2018).
4. D. H. Van Winkle, C. A. Murray, Layering transitions in colloidal crystals as observed by diffraction and direct-lattice imaging. *Phys. Rev. A* **34**, 562-573 (1986).
5. X. Ye *et al.*, Single-particle mapping of nonequilibrium nanocrystal transformations. *Science* **354**, 874-877 (2016).
6. L. Yu *et al.*, Quantitatively *in situ* imaging silver nanowire hollowing kinetics. *Nano Lett.* **16**, 6555-6559 (2016).
7. V. Westphal *et al.*, Video-rate far-field optical nanoscopy dissects synaptic vesicle movement. *Science* **320**, 246-249 (2008).
8. A. Einstein, Über die von der molekularkinetischen theorie der wärme geforderte bewegung von in ruhenden flüssigkeiten suspendierten teilchen. *Ann. Phys.* **322**, 549-560 (1905).
9. S. Sacanna, D. J. Pine, Shape-anisotropic colloids: Building blocks for complex assemblies. *Cur. Opin. Colloid Interf. Sci.* **16**, 96-105 (2011).
10. B. Senyuk *et al.*, Topological colloids. *Nature* **493**, 200-205 (2013).
11. K. Zhao, T. G. Mason, Self-organized chiral colloidal crystals of Brownian square

crosses. *J. Phys.: Condens. Matter* **26**, 152101 (2014).

12. A. R. Tao, S. Habas, P. Yang, Shape control of colloidal metal nanocrystals. *Small* **4**, 310-325 (2008).
13. P. Li *et al.*, Assembly of a porous supramolecular polyknot from rigid trigonal prismatic building blocks. *J. Am. Chem. Soc.* **141**, 12998-13002 (2019).
14. K. Mayoral, T. Mason (2013) Entropic self-organization of tri-star colloids. (Electrum Publishing, Los Angeles).
15. E. S. Harper, G. van Anders, S. C. Glotzer, The entropic bond in colloidal crystals. *Proc. Natl. Acad. Sci. U.S.A.* **116**, 16703-16710 (2019).
16. B. Derjaguin, L. Landau, Theory of the stability of strongly charged lyophobic sols and of the adhesion of strongly charged particles in solutions of electrolytes. *Prog. Surf. Sci.* **43**, 30-59 (1993).
17. K. Zhao, R. Bruinsma, T. G. Mason, Local chiral symmetry breaking in triatic liquid crystals. *Nat. Commun.* **3**, 801 (2012).
18. K. Zhao, T. G. Mason, Shape-designed frustration by local polymorphism in a near-equilibrium colloidal glass. *Proc. Natl. Acad. Sci. U.S.A.* **112**, 12063-12068 (2015).
19. G. van Anders, D. Klotsa, N. K. Ahmed, M. Engel, S. C. Glotzer, Understanding shape entropy through local dense packing. *Proc. Natl. Acad. Sci. U.S.A.* **111**, E4812-E4821 (2014).
20. T. Yu, T. G. Mason, Brownian lithographic polymers of steric lock-and-key colloidal linkages. *Sci. Adv.* **7**, eabg3678 (2021).
21. J. A. Anderson, J. Antonaglia, J. A. Millan, M. Engel, S. C. Glotzer, Shape and

symmetry determine two-dimensional melting transitions of hard regular polygons. *Phys. Rev. X* **7**, 021001 (2017).

22. J. de Graaf, R. van Roij, M. Dijkstra, Dense regular packings of irregular nonconvex particles. *Phys. Rev. Lett.* **107**, 155501 (2011).

23. P.-Y. Wang, T. G. Mason, Colloidal lock-and-key dimerization reactions of hard annular sector particles controlled by osmotic pressure. *J. Am. Chem. Soc.* **137**, 15308-15314 (2015).

24. P.-Y. Wang, T. G. Mason, A Brownian quasi-crystal of pre-assembled colloidal penrose tiles. *Nature* **561**, 94-99 (2018).

25. Q. Wu *et al.*, Poly[n]catenanes: Synthesis of molecular interlocked chains. *Science* **358**, 1434-1439 (2017).

26. R. Dreyfus *et al.*, Microscopic artificial swimmers. *Nature* **437**, 862-865 (2005).

27. A. Lukach, K. Liu, H. Therien-Aubin, E. Kumacheva, Controlling the degree of polymerization, bond lengths, and bond angles of plasmonic polymers. *J. Am. Chem. Soc.* **134**, 18853-18859 (2012).

28. S. Asakura, F. Oosawa, On interaction between two bodies immersed in a solution of macromolecules. *J. Chem. Phys.* **22**, 1255-1256 (2004).

29. P. Y. Wang, *Self-assembly, pre-assembly, and configurational reactions of shape-designed colloids in fluctuating brownian monolayers* (University of California, Los Angeles, 2017).

30. T. G. Mason, Osmotically driven shape-dependent colloidal separations. *Phys. Rev. E* **66**, 060402 (2002).

31. D. J. Ashton, R. L. Jack, N. B. Wilding, Self-assembly of colloidal polymers via depletion-mediated lock and key binding. *Soft Matter* **9**, 9661-9666 (2013).

32. S. Sacanna, W. T. M. Irvine, P. M. Chaikin, D. J. Pine, Lock and key colloids. *Nature* **464**, 575-578 (2010).

33. K. Zhao, T. G. Mason, Directing colloidal self-assembly through roughness-controlled depletion attractions. *Phys. Rev. Lett.* **99**, 268301 (2007).

34. M. A. Boles, M. Engel, D. V. Talapin, Self-assembly of colloidal nanocrystals: From intricate structures to functional materials. *Chem. Rev.* **116**, 11220-11289 (2016).

35. X. Ye *et al.*, Improved size-tunable synthesis of monodisperse gold nanorods through the use of aromatic additives. *ACS Nano* **6**, 2804-2817 (2012).

36. K. Miszta *et al.*, Hierarchical self-assembly of suspended branched colloidal nanocrystals into superlattice structures. *Nat. Mater.* **10**, 872-876 (2011).

37. W. B. Rogers, V. N. Manoharan, Programming colloidal phase transitions with DNA strand displacement. *Science* **347**, 639-642 (2015).

38. L. Onsager, The effects of shape on the interaction of colloidal particles. *Ann. N.Y. Acad. Sci.* **51**, 627-659 (1949).

39. J. Yan, S. C. Bae, S. Granick, Rotating crystals of magnetic janus colloids. *Soft Matter* **11**, 147-153 (2015).

40. A. Yethiraj, A. van Blaaderen, A colloidal model system with an interaction tunable from hard sphere to soft and dipolar. *Nature* **421**, 513-517 (2003).

41. M. T. Sullivan *et al.*, An electric bottle for colloids. *Phys. Rev. Lett.* **96**, 015703 (2006).

Chapter 2 – Brownian Lithographic Polymers of Steric Lock-and-Key Colloidal Linkages

Reprinted with permission from T. Yu, T. G. Mason, Brownian lithographic polymers of steric lock-and-key colloidal linkages. *Sci. Adv.* **7**, eabg3678 (2021). Modifications are made to comply with formatting requirements. CC BY-NC 4.0 International Public License.

2.1 Introduction

The compositions and structures of monomers, as well as the nature of bonds and other interactions between them, influence the resulting properties of molecular polymers. Beyond naturally occurring biopolymers, synthetic organic chemistry has provided access to an impressive array of flexible and semi-flexible polymers that have different structures, shapes, functionalities, and morphologies based primarily on covalent bonds between constituent atoms through a variety of polymerization or self-assembly reactions (1). Examples of these include branched (2), star (2), and brush polymers (3), as well as larger-scale dendrimers (2), DNA origami (4), copolymers (2, 5) and thermally responsive cross-linked micro-gel beads (6). In addition, remarkably, mechanically interlocked super-molecular polymer systems with complex topologies, such as smaller rings that can slide along a larger ring, have also been synthesized (7, 8). While the routes of bottom-up chemical syntheses of organic molecular polymers and the control over their structures, yields, and polydispersities are continuing to advance, there are also opportunities for expanding the frontiers of polymer science through alternative routes, including those involving colloidal mimics of polymers that can be more readily visualized down to the monomer scale. Such colloidal mimics enable experimental studies of polymer dynamics that can be imaged to make real-space movies using optical microscopy; this approach overcomes the limitations of imaging much smaller molecular polymers that have significantly faster dynamics by other means.

Among the first studies of colloidal mimics of polymers have been the collapse of flexible chains of fractionated microscale ferrofluid droplets initially formed by a magnetic field and held together by temperature-controlled salt-induced attractions between constituent droplet interfaces (9), systems of active 'swimmers' that have chains of droplets bridged by flexible polymers (10), as well as self-assembled columnar chains of wax microdisks that have long persistence lengths via shape-controlled anisotropic depletion attractions (11, 12) induced by nanoscale surfactant micelles. Depletion attractions have also been used to create more flexible chains of convex-concave pac-man-like particles (13-15). Other systems of colloidal mimics of polymers include chains held together by programmable interactions such as between ss-DNA oligomerically functionalized colloids (16, 17), and size-controlled self-assembly of colloidal building blocks into various polymer architectures such as networks induced by magnetic forces (18). Similar colloidal systems with programmed interactions have been used to self-assemble a wide range of dense crystalline structures, too (19). However, none of these colloidal systems that mimic polymers have relied upon steric bonding between solid interlocking shape-designed structures that have effectively hard interactions between their surfaces. Such steric bonds between colloids are unusual because no attractions and no molecular connections are used to connect the shape-complementary substructures of adjacent lock-and-key colloids. Instead, the pre-inserted head of one rigid lock-and-key colloid is constrained within the tail of an adjacent rigid lock-and-key colloid in a manner that sterically (*i.e.* geometrically) prohibits the two colloids from separating. Moreover, none of the existing self-assembly approaches offer the extremely low defect rate and high yield of the precisely desired structures in parallel as that which can be achieved through top-down lithography, particularly optical stepper lithography.

The advent of lithographically pre-assembled monolayers (litho-PAMs) opens up a new avenue for fabricating and studying new kinds of dense two-dimensional (2D) systems of shape-designed colloids that have pre-configured positions and orientations with low defects over wide areas (20). Until now, the litho-PAMs approach has only been used to create and study dense monolayers of microscale Penrose P2 kite and dart tiles that form a fluctuating 5-fold quasi-crystal, experience Brownian excitations, and are confined within enclosing walls. This dense Penrose quasi-crystal system has been demonstrated to melt, and the tiles lose memory of their initial configuration when a wall is removed, since the in-plane interactions between the tiles is effectively hard. While studying the melting of dense systems of shape-designed hard-interacting tiles is interesting in its own right, finding a way to create long-lived many-body dynamical colloidal systems without confining walls and without inducing in-plane attractions would be highly desirable, too.

Here we show that this desirable goal can be achieved by advancing litho-PAMs (20) to fabricate complex fluctuating colloidal chain-like lock-and-key lithographic mimics of polymers. Doing so empirically is non-trivial, since the limitations of optical diffraction must be respected and yet complete separation between all interlocking colloidal particles must be obtained robustly. By programming designer lock-and-key tile shapes and their relative positions and orientations in the lithographic mask using computer-aided-design and also by optimizing lithographic production and lift-off techniques, we produce interconnected and sterically interlocked yet reconfigurable architectures of colloidal tiles that are long-lived in the absence of confining walls. Moreover, these architectures, which we call polylithomers (PLMs), are lithographically pre-assembled and therefore not made by resorting to programmable molecular attractions between the surfaces of the colloidal lithomer (LM) tiles. Upon release from the substrate, Brownian excitations cause these mobile PLMs to exhibit conformational fluctuations; so, entropic considerations are important just as they are for molecular polymers. Such interconnected colloidal structures could be viewed from a chemical perspective as mimics of polymers that can be designed top-down to have considerable morphological complexity. Equivalently, these dynamic interconnected structures could also be viewed from a statistical mechanical perspective as Brownian systems of colloidal linkages, since linkages are mechanical assemblies composed of discrete rigid objects that have joints which couple microstates of constituent tiles.

Among models of polymers, two of the most well-known are the freely jointed chain (FJC) and worm-like chain (WLC) (21). One key assumption, common to both of these models, is that the bonds linking monomers within the polymers are inextensible. While this assumption is reasonable for most molecular polymers, in some cases under large applied force, scientists have observed (22, 23), and theoretically studied (24) the extensibility (*i.e.* elasticity) of polymeric bonds. Typically, it is much easier to cause a conformational change by rotating bonds that lack torsional rigidity within a molecular polymer than it is to alter the bond-distance between adjacent monomers. However, so far, there is no experiment that directly visualizes the extensibility of individual bonds, which is different than overall extensibility of a flexible polymer chain. Therefore, controlling and visualizing bond extensibility in new kinds of polymer systems would be interesting. To explore this, we use optical stepper lithography to produce a wide variety of PLMs, including structures that have not yet been synthesized through other bottom-up methods. Moreover, we show that changing the designed shapes of sub-tile features in LMs provides a means of controlling the degree of extensibility of bonds within colloidal linkages. Our experimental advances in lithographic pre-assembly, real-space visualization using optical microscopy, and lock-and-key particle tracking reveal distinct longitudinal fluctuations related to bond extensibility even under only equilibrium Brownian excitations.

2.2 Materials and Methods

2.2.1 Designing lithomer shapes and initial conformations of polylithomers

Simple mono-head, mono-tail lithomers (see **Fig. 2.1A**) are designed to have a convex rounded-rectangular head (6.0 μm in width and 2.5 μm in length), a slender rectangular neck (1.0 μm in width and 4.0 μm in length), and a tail (outer width: 13.0 μm; outer length: 7.0 μm) having a rounded-rectangular internal concave cavity with an opening (inner width: 8.0 μm; inner length: 4.5 μm for NC-type and 5.0 μm for LC-type). To create a design of a chain-like polylithomer, the head of a given lithomer is positioned inside the internal cavity of the tail of a neighboring lithomer, and this is repeated as additional lithomers are added. In order to design various 1D, quasi-2D, and 2D PLM patterns, we not only copy and translate standard LMs but

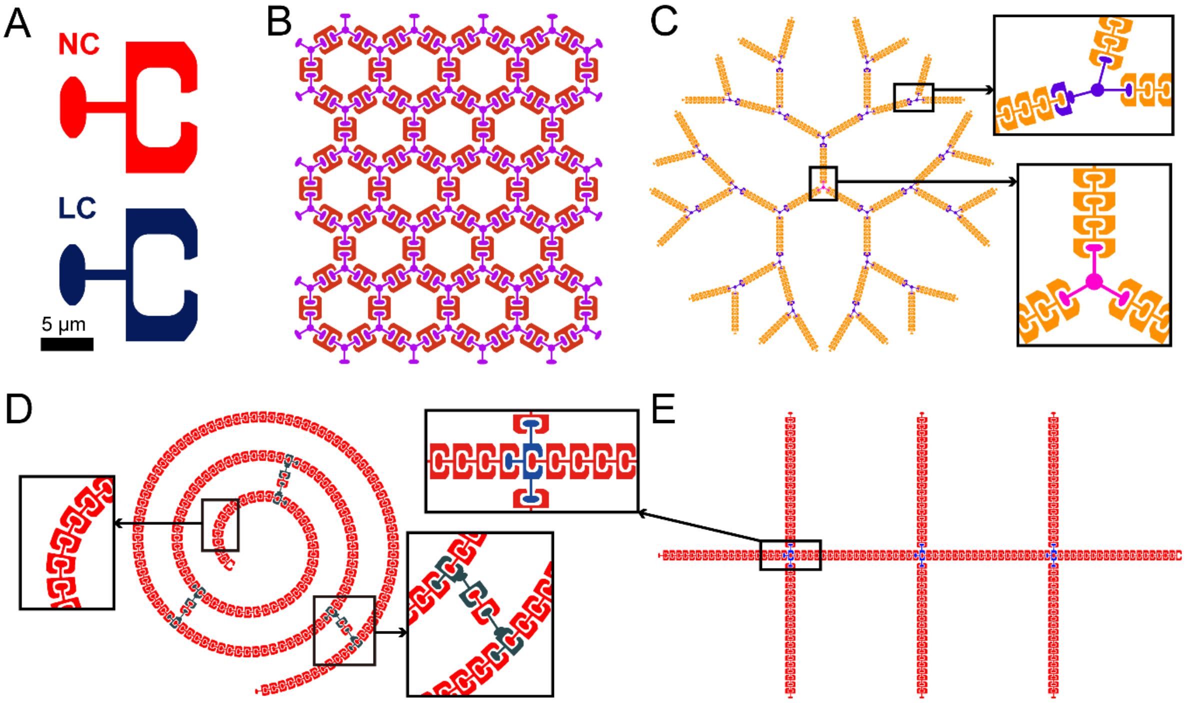

Figure 2. 1. Designs of lithographic monomers (lithomers, LMs) and sterically bonded lock-and-key polylithomers (PLMs). (A) Basic LMs designed to have convex heads and tails with concave cavities: normal cavity (NC; red, top); larger cavity (LC, dark blue, bottom). Internal cavity lengths are 4.5 μm for NC and 5.0 μm for LC. Scale bar: 5 μm in wafer scale. (B) Quasi-2D honeycomb mesh PLM composed of di-cavity LMs (dark red) and tri-head LMs (purple). (C) 3-2-2-2 dendrimer PLM. Insets: mono-cavity, di-head branched LM (blue, top box) and tri-head LM (magenta, bottom box). (D) 3-Bridged chiral(-) spiral PLM. The LMs here have intrinsic curvatures that vary along the spiral. Insets: LMs designed to have non-zero intrinsic curvature (left box); Crosslinking LMs (right box). (E) Symmetric branched PLM having 3 pairs of symmetric side chains off a central backbone. Inset (box, arrow): detail showing multi-headed branching LM (blue) at a branching point.

also mutate, fuse, or modify their shapes, particularly at junctions and nodes. For example, the 2D mesh (**Fig. 2.1B**) is composed of two differently shaped lithomers that result from: (1) the fusion of three heads with necks into an equilateral tri-star shape, and (2) the fusion of two tails with cavities. Alternatively, the junctions in polylithomeric dendrimers are made of one tail and the fusion of three heads with necks (**Fig. 2.1C**). Through a different type of modification, the spiral's intrinsic curvature has been designed to change from 0.014 μm^{-1} (interior terminal end) to 0.0046 μm^{-1} (exterior terminal end), primarily by continuously varying the angle between necks and tails, as well as by mutating the tail structure including the cavity. A wide variety of branched PLMs can be designed by varying the structures of junction LMs, which can have controllable numbers of bonds, bond lengths, and bond angles; as an example, we fuse an extra head with a neck onto a tail (**Fig. 2.1D**). As another example, the junctions of the branched polymer are created by fusing two additional side-heads onto the tail of a standard NC-type LM (**Fig. 2.1E**).

2.2.2 Fabrication by photolithography

To facilitate imaging and ensure a negatively charged, flat, smooth substrate below the fabricated polylithomers, we use a transparent glass wafer (University Wafer, polished borosilicate 33, 500 μm thick, 100 mm dia., prime). After pre-baking this wafer at 200 °C for 3 min and cooling back to 25 °C on aluminum foil to remove any adsorbed moisture, we spin-coat (500 rpm for 5 s with acceleration of 100 rpm s^{-1}, and then 3000 rpm for 30 s with acceleration of 300 rpm s^{-1} (Headway Research, PWM32 Spin-Coater) a release layer of Omnicoat (Microchem Inc.) onto the glass wafer. After baking at 200 °C for 1 min, the Omnicoat forms a solid transparent thin (≈15 nm) release layer. The wafer is then cooled to 25 °C. We spin-coat and bake this Omnicoat layer a second time using the same procedure to ensure that the entire wafer is fully coated and thereby achieve complete particle release. Onto the layer of Omnicoat, we spin-coat a layer of epoxy SU-8-2002 (Microchem Inc.) negative photoresist and subsequently bake at 95 °C for 90 s. A solid, transparent, ≈2 μm-thick layer of un-cross-linked SU-8 is formed, and the wafer is cooled to 25 °C. This coated wafer is then loaded into the stepper and exposed using the quartz-chrome mask to patterned UV light (energy dose of 140 mJ cm^{-2}), which selectively cross-links the SU-8 photoresist into the desired pre-configured PLMs on the wafer. After post-exposure baking at 95 °C for 75 s and cooling to 25 °C, any remaining unexposed and un-cross-linked SU-8 is removed by SU-8 Developer (Microchem Inc., 1-methoxy-2-propyl acetate) for 3 min through continuous agitation. Next, we rinse the wafer in isopropyl alcohol and dry it with a flow of nitrogen gas to remove any residual uncrosslinked SU-8, yielding disconnected, transparent pre-assembled PLMs attached to the release layer of Omnicoat.

2.2.3 Release and imaging of polylithomer

Before releasing, we first build an elastomeric PDMS well, which confines a release solution-dispersion (RSD) within a certain volume. We first mix a PDMS elastomer and its curing agent (Sylgard 184) at a weight ratio of 10:1 on a clean Petri dish; leave it at 25 °C for de-gassing overnight; and put it in a vacuum oven at 80 °C for 2 h. Then we cut this disk-like layer of PDMS into a square-frame well that is about 3 mm high and has a 1.3 cm outer edge length and a 1 cm inner edge length. Next, we clean the region around the selected PLM on the glass wafer with deionized water using a cotton-tipped applicator, thereby removing Omnicoat, carefully attach the PDMS well onto this region and bake at 80 °C for 2 hours to form a water-impermeable bond with the glass surface.

The composition of the RSD is vital not only to gradually dissolve the Omnicoat release layer, but also to keep the released PLMs stable against aggregation and close to the surface of the glass wafer. Therefore, besides tetramethylammonium hydroxide (TMAH; Sigma-Aldrich, 0.5% w/v) as a basic release agent that dissolves Omnicoat, we also include sodium dodecyl sulfate (SDS; MP Biomedicals, ultrapure, 25 mM) as a stabilizing agent, and polystyrene spheres (carboxylate-stabilized, surfactant-free; Magsphere, 52-nm diameter, 1.5% w/v solids) as a depletion agent that strongly inhibits the lower faces of all released LM-particles from leaving the vicinity of the plane. Gravitational forces normal to the plane, caused by the density difference between the crosslinked SU-8 and the RSD, also act in concert with the depletion forces to provide additional stabilization of the PLMs against breakup over long times after release by further suppressing out-of-plane motion of constituent LMs. A highly screened short-range charge repulsion, provided by negative charges on the glass wafer and on the surfaces of the SU-8 particles (via adsorbed dodecyl sulfate anions), ensures lubrication and mobility of all particles after release. Because the RSD when first made may contain some small aggregates, we filter the RSD using a 2.5 μm filter, centrifuge it in a 1.5 mL conical tube at 500 rpm for 4 minutes, and withdraw all but the lowest ≈50 μL. We completely fill the PDMS well with this RSD and immediately put a cover slip over it to reduce evaporation.

We place the wafer with RSD-filled PDMS well onto an inverted optical microscope (Nikon TE2000, 10x or 20x CFI plan achromat objectives, Nikon Z7 and D5300 cameras, silent mode). Brightfield transmission images, taken through the wafer, are recorded every 15 seconds using Camera Control Pro software (Nikon), yielding *in-situ* high-resolution time-lapse movies of fluctuating Brownian PLMs.

2.2.4 Image analysis and particle tracking

To analyze these movies, we have gone beyond prior particle tracking routines that merely tracked vertices of polygonal objects (e.g. square tiles or dart tiles) (20, 25). As a first step, we batch process image sequences in Photoshop using built-in functions: grayscale, rotate, crop, 2x image scale, invert, and magic wand to select and remove background a color range selection/expansion. Using Mathematica (Wolfram Research Inc.), for each LM, we extract a bright region corresponding to each head and two bright regions corresponding to both sides of each tail. We then obtain the centroids of these bright regions to calculate the position and orientation of each LM (routines used: *MorphologicalComponents*, *SelectComponents*, and *ComponentMeasurements*). We also calculate the bond length, bond angles and, assuming a Boltzmann probability, extract an effective bonding potential from the resulting distributions. For the case of steady-state fluctuations of PLMs around an equilibrium conformation, independent members of equilibrium ensembles are approximately obtained by sampling every 500 frames. Each ensemble contains approximately 95 individual lithomers. Terminal lithomers that are within three monomer units of ends and junctions are excluded from the ensemble, so average bond properties reflect the behavior of monomers within the linear chain.

To calculate the evolution of curvature from a non-equilibrium initial ring-like PLM conformation of LMs that have been designed to have no intrinsic curvature, we first skeletonize the contour of this PLM using Photoshop and Mathematica. We discretize the contour into a set of 400 points and fit these points to circles in groups of 5 points, yielding local curvature which is mapped into color. In this analysis, the ends of the PLM are truncated (by about ≈3 LMs), so the analyzed colored contour is slightly shorter than the actual PLM.

2.3 Results

2.3.1 Design and fabrication of polylithomers

We design and fabricate a wide variety of self-integral polylithomeric linkage systems by extending litho-PAMs (20), which until now has only been used to create preconfigured 2D systems of unlinked mobile colloidal tiles confined by an outer wall. Using a quartz-chrome lithographic mask (150 mm x 150 mm, Digidat Inc.), we employ optical stepper lithography to manufacture microscale lock-and-key PLMs, which we have digitally designed (L-Edit, Tanner Research). Because the minimum trench feature between the head and the tail is 0.8 μm, imposed by the type of photoresist and the diffraction limit of the stepper (ASML stepper, PAS 5500/200, 5X reduction, ultraviolet (UV) i-line 365 nm, ≈250 nm minimum feature size), the overall dimensions of individual LMs are near the upper limit of the colloidal scale (≈10 μm).

Individual LMs are designed to have a variety of shapes; PLMs can be made of one or more types (*i.e.* shapes) of LMs. A simple PLM chain can be made of just a single LM-shape (see *e.g.* the normal cavity (NC) type LM in **Fig. 2.1A**-top): a convex rounded-rectangular head, a slender rectangular neck, and a tail having a rounded-rectangular internal concave cavity into which the head of a neighboring lithomer can also be printed (see Materials and Methods for exact dimensions of sub-particle features). We customize the flexibility of junctions by adjusting the designed parameters of the head, tail, cavity and neck; for instance, the cavity can be enlarged somewhat (see the large cavity (LC) type LM in **Fig. 2.1A**-bottom). More complex PLMs are made using two or more different LM-shapes and appropriate junctions. We then copy, translate, rotate and, if necessary, mutate shapes of LMs to form PLMs that mimic and go beyond classic molecular polymer architectures. We have made a porous quasi-2D honeycomb mesh that represents systems with a high level of coupling (**Fig. 2.1B**), a dendrimer with several hierarchical levels of branching (**Fig. 2.1C**), a spiral with flexible bridges (**Fig. 2.1D**), and branched polymers (**Fig. 2.1E**). On an individual glass wafer (100 mm diameter, 500 μm thickness), we print 16 different regions, each containing several PLMs, in a 4x4 array. Printed PLMs can be individually released using a release solution-dispersion (RSD) containing a depletion agent that inhibits lift-off of LMs, and the evolution of a PLM's conformation is then recorded as an image sequence and later analyzed. Additional details associated with design, fabrication, release, and imaging are provided in the **Materials and Methods** section.

2.3.2 Real-time visualization of release and fluctuation

We demonstrate the versatility of our lithographic method for making free-standing polymer-like colloidal chain structures having a wide variety of pre-assembled dimensions, topologies, configurations, and intrinsic local curvatures. We have successfully produced and released a 4-arm star (**Movie 2.1**), branched polymers (**Figs. 2.2A** and **2.2B**, **Movie 2.2**) and bridged spiral polymers with varying intrinsic curvature **(Figs. 2.2C** and **2.2D**, **Movie 2.3**), dendrimers with multiple branching levels (**Figs. 2.2E** and **2.2F**, **Movie 2.4**), and quasi-2D mesh-particles (**Figs. 2.2G** and **2.2H**, **Movie 2.5**). In **Fig. 2.2**, we display grayscale optical micrographs of PLMs, as well as zoomed-in insets, both before and long after release (≈30 h). By performing time-lapse high-resolution video optical microscopy, we record movies of the collective dynamics of these colloidal linkages that reveal positions and orientations of all individual LMs. Our experiments effectively provide real-space visualization of entropically excited conformations of many analogs of molecular polymers, yielding sub-monomer resolution of the positions and orientations of all constituent LMs.

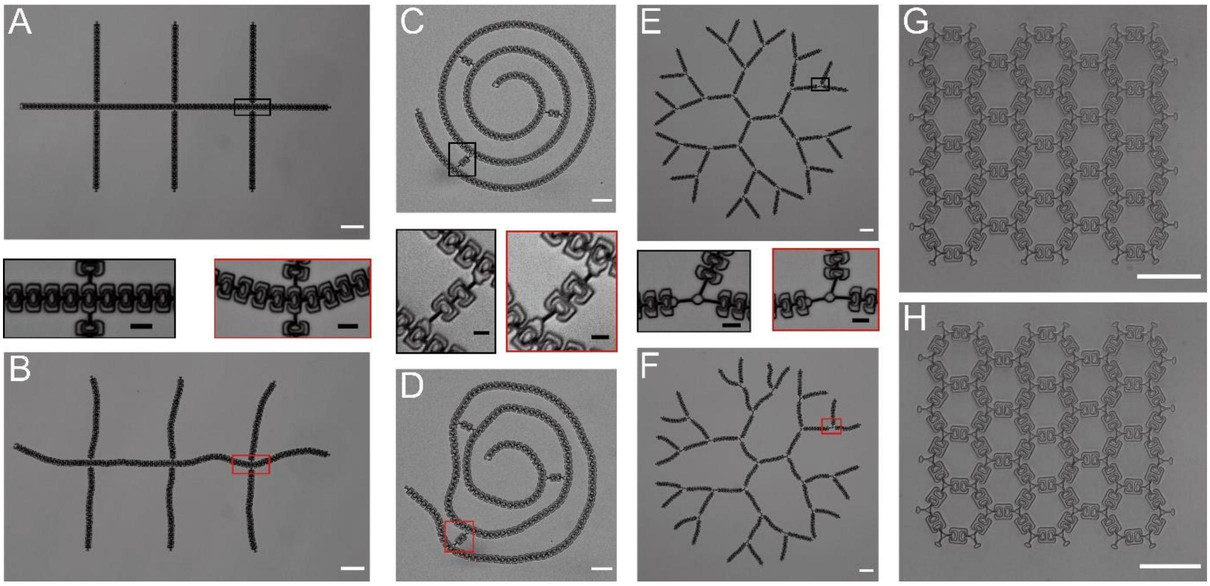

Figure 2. 2. Pre- and post-release transmission brightfield microscopy images of fabricated polylithomers immersed in a release solution-dispersion (RSD). Symmetric branched PLM: (A) before release and (B) 30 h after release. 3-Bridged chiral(-) spiral PLM: (C) before and (D) 30 h after release. 3-2-2-2 Dendrimer PLM: (E) before and (F) 30 h after release. Quasi-2D honeycomb mesh PLM: (G) before and (H) 30 h after release. Corresponding zoomed images (between parts A and B, C and D, and E and F) show branching points: pre-release (black boxes) and post-release (red boxes). Brownian excitations cause fluctuations in conformations of post-release PLMs. Scale bars: 50 µm (white), 10 µm (black).

2.3.3 Particle tracking and statistical properties

To go beyond a qualitative description of dynamics and fluctuations, we have advanced and refined an image analysis and particle tracking method, which works for complex lock-and-key shapes in close proximity, in order to determine the positional and angular coordinates of each individual NC-type lithomer (**Figs. 2.3A**, **2.3B**, and **2.3C**). Using these coordinates, we then calculate inter-LM spacings, l, and inter-LM angles, α, between adjacent lithomers. This method provides an accuracy within ≈ 0.5% for inter-LM spacing and ≈ 0.2 deg for inter-LM angles using a pre-configured chain with known parameters before

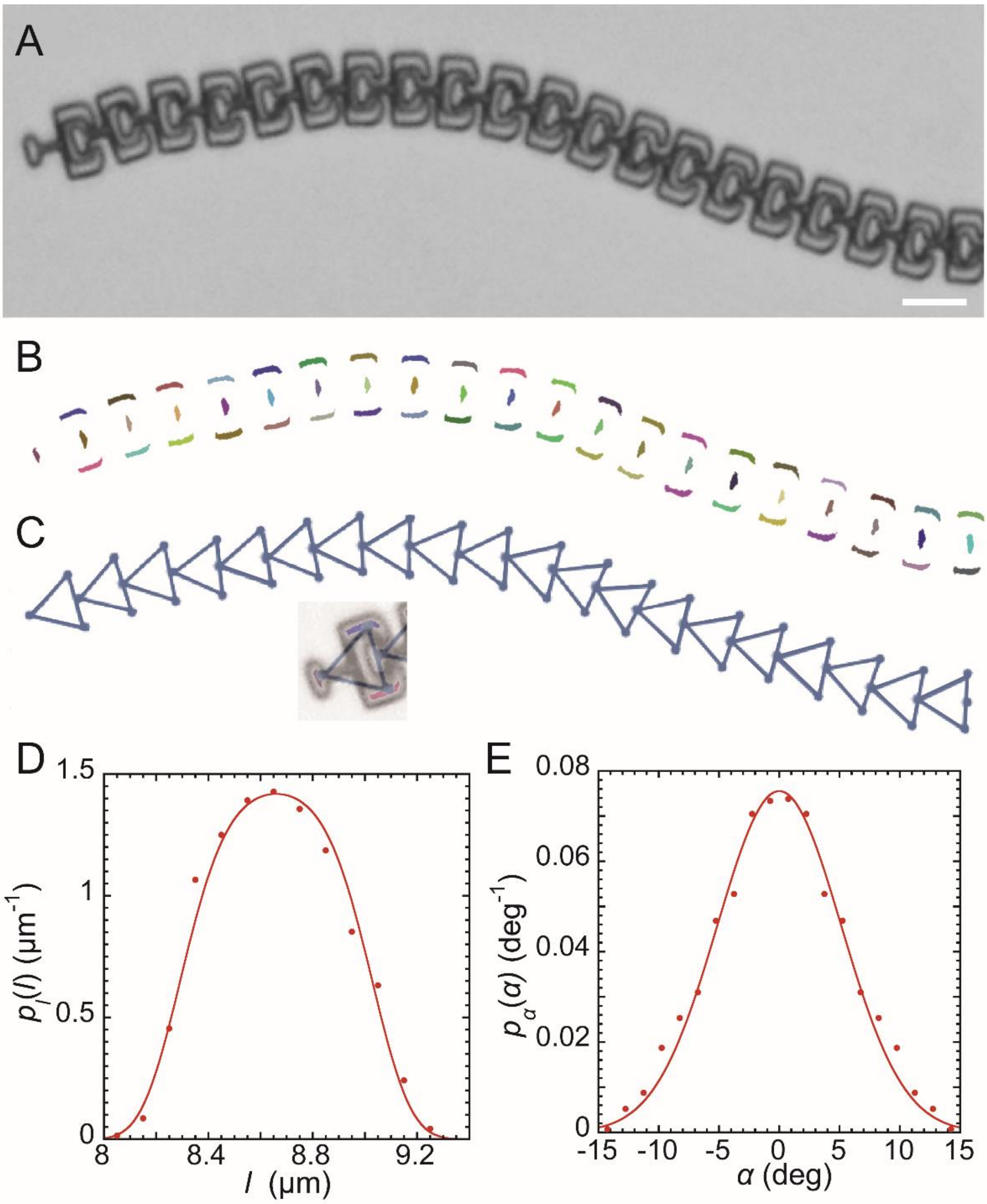

Figure 2. 3. Particle tracking and statistical properties of linear chains of PLMs obtained from arms of branched PLMs. (A) Transmission micrograph of an arm of NC-type LMs (grayscale from RGB color). Scale bar: 10 µm. (B) Extracted morphological components of part A, yielding head and tail sub-particle features (colored regions). Each head produces one colored region; each tail produces two colored regions, one on each side of the cavity. (C) Triangles represent extracted positions and orientations of LMs from centroids of morphological components in part B. Inset: overlay of (A)-(C) onto one monomer. (D) Observed probability density of interparticle (*i.e.* inter-LM) centroid spacing, l, defined as the distance between the centers of two adjacent triangles, of PLM_{NC}s irrespective of the inter-LM bond angle α. Fit: quartic potential in a Boltzmann distribution (line, see text, $R^2 = 0.98$). (E) Observed probability density of α, defined by the relative orientation between two adjacent triangles of PLM_{NC}s, assuming even symmetry about $\alpha = 0$ and irrespective of l. Fit: quadratic potential in a Boltzmann distribution (line, see text, $R^2 = 0.98$).

releasing as a reference. To obtain an approximate sampling of independent members of an equilibrium ensemble of Brownian conformations after release, we analyze images separated by many frames (*i.e.* ≈500 frames, ≈2 h).

Using this ensemble, we calculate statistics of polymeric properties such as the normalized probability density functions (PDFs) of inter-LM spacing, $p_l(l)$, (**Fig. 2.3D**) and inter-LM angle, $p_\alpha(\alpha)$ (**Fig. 2.3E**). The shapes of the observed peaks for $p_l(l)$ and $p_\alpha(\alpha)$ are substantially different. The peak for $p_l(l)$ in **Fig. 2.3D** is obviously non-Gaussian and has a flattened top; whereas, the observed peak for $p_\alpha(\alpha)$ in **Fig. 2.3E** is nearly Gaussian. Therefore, we attempt to fit $p_l(l)$ and $p_\alpha(\alpha)$ to Boltzmann distributions that assume quartic and quadratic potential energies, respectively. These fits well describe the measured distributions (see lines in **Figs. 2.3D** and **2.3E**, respectively); the quartic term is essential for capturing the non-Gaussian nature of $p_l(l)$. Correspondingly, in **Figs. 2.4A** and **2.4B**, we display the measured potential for inter-LM spacing, $U_l(l)$, and angle, $U_\alpha(\alpha)$, extracted from **Figs. 2.3D** and **2.3E**, respectively, assuming Boltzmann statistics (NC-type LMs: red points), and we also show the fits to these extracted potential energies (NC-type LMs: red lines).

2.3.4 Comparison between PLMs with different cavities

To demonstrate that we can design and fabricate PLMs having different types of steric lock-and-key bonds that yield different resulting properties and behavior, we compare the potentials, persistence lengths, and extensibilities of linear PLM segments made using two differently designed lithomers, one with a normal cavity (NC-type, $\mathrm{LM_{NC}}$) and the other with a larger cavity (LC-type, $\mathrm{LM_{LC}}$).

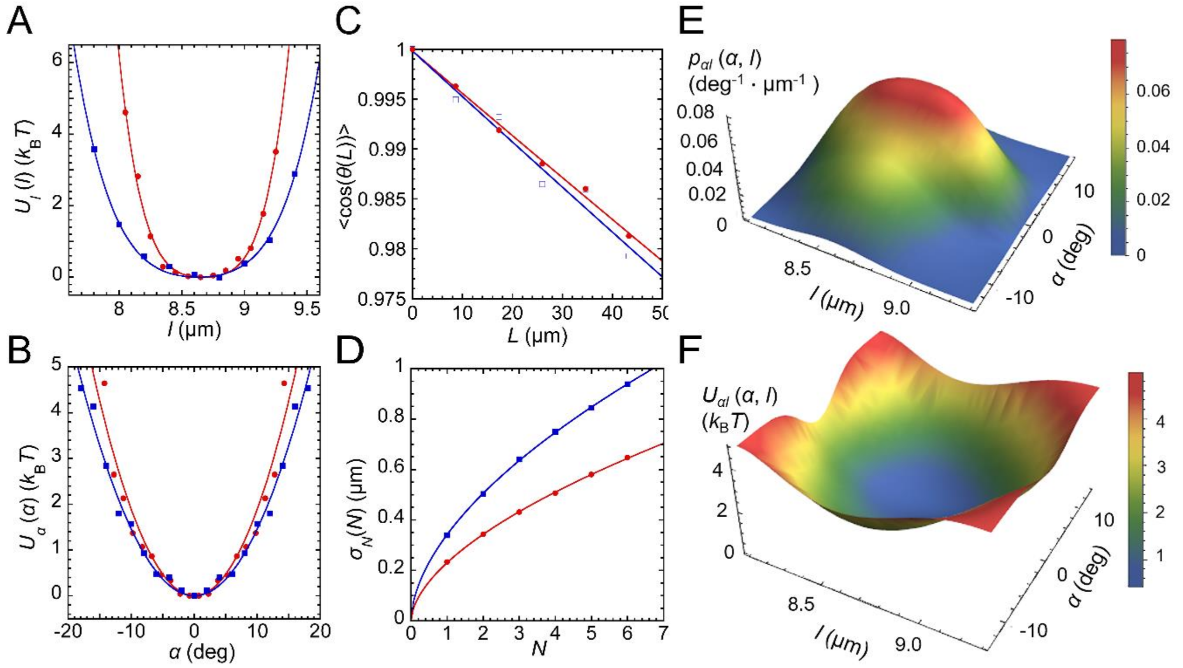

Figure 2. 4. Equilibrium bond characteristics of PLM$_{NC}$s and PLM$_{LC}$s: designer bond extensibility and semi-flexibility. (A) Extracted potential of interparticle centroid spacing, $U_l(l)$, between adjacent LMs, assuming Boltzmann statistics, irrespective of bond angle α: PLM$_{NC}$ (red circles) and PLM$_{LC}$ (blue squares). Solid lines: fits to quartic potentials for NC-type (red, $R^2 = 0.993$) and LC-type (blue, $R^2 = 0.998$). Fitted most probable spacing l_0 between LMs for both NC and LC types of PLMs are nearly the same: $l_0 \approx 8.65$ μm. (B) Extracted potential of bond angle, $U_\alpha(\alpha)$, assuming Boltzmann statistics and U_α even in α, irrespective of l. Solid lines: fits to quadratic potentials for NC-type (red, $R^2 = 0.94$) and LC-type (blue, $R^2 = 0.98$). (C) Persistence length L_p is obtained by fitting observations of <cos(θ)> (symbols same as in part A) as a function of length along the contour, L, to exp($-L/L_p$): NC-type (red line, $R^2 = 0.994$); LC-type (blue line, $R^2 = 0.966$). (D) Standard deviation σ_N of spacing between N LMs along a PLM chain (symbols same as in part A). Fits to power law functions: NC-type (red line, $R^2 = 0.9997$); LC-type (blue line, $R^2 = 0.9998$). Surface plots for NC-type PLMs: (E) 2D probability density function, $p_{\alpha l}(\alpha,l)$, assuming even symmetry for α, and (F) extracted 2D inter-LM potential $U_{\alpha l}(\alpha,l)$ from part E assuming Boltzmann statistics.

First, we co-plot the potentials related to inter-LM spacing for both types of PLMs (**Fig. 2.4A**). We fit the potential associated with inter-LM spacing with $U_l(l) = U_{l2}[(l/l_0) - 1]^2 + U_{l4}[(l/l_0) - 1]^4$, where l_0 represents the most probable spacing, and U_{l2} and U_{l4} represent potential coefficient values related to quadratic and quartic terms, respectively; each type of LM can have different values of l_0, U_{l2}, and U_{l4}. After performing the fitting, we find that in the immediate vicinity of l_0 ($l_{0,\mathrm{NC}} = 8.674 \pm 0.004$ μm, $l_{0,\mathrm{LC}} = 8.629 \pm 0.005$ μm), where the second order term (U_{l2}) dominates, both fitted U_{l2} parameters are similar ($U_{l2,\mathrm{NC}}/(k_\mathrm{B}T) = 187 \pm 57$, $U_{l2,\mathrm{LC}}/(k_\mathrm{B}T) = 143 \pm 27$). However, for values of l that are further away from l_0, the quartic term dominates, and we find a large difference in the associated fit parameters: $U_{l4,\mathrm{NC}}/(k_\mathrm{B}T) = (1.39 \pm 0.14) \times 10^5$ and $U_{l4,\mathrm{LC}}/(k_\mathrm{B}T) = (2.66 \pm 0.36) \times 10^4$, such that $U_{l4,\mathrm{NC}} > U_{l4,\mathrm{LC}}$, which is consistent with the smaller designed cavity of the NC-type LM as compared to the LC-type LM.

Next, for each type of LM, we fit the measured potential as a function of inter-LM angle, $U_\alpha(\alpha)$, in **Fig. 2.4B** to $U_\alpha(\alpha) = U_{\alpha 2}\,\alpha^2$, where $U_{\alpha 2}$ represents a potential coefficient value related to this quadratic form. The observed $U_\alpha(\alpha)$ of NC-type and LC-type PLMs can both be captured well by the same quadratic form, and the $U_{\alpha 2}$ fit parameters are also distinguishably different: $U_{\alpha 2,\mathrm{NC}}/(k_\mathrm{B}T\ \mathrm{deg}^{-2}) = 0.0190 \pm 0.0008$ and $U_{\alpha 2,\mathrm{LC}}/(k_\mathrm{B}T\ \mathrm{deg}^{-2}) = 0.0146 \pm 0.0003$. All observed values of l and α are within the designed limits ($7.5\ \mu\mathrm{m} < l_\mathrm{NC} < 9.5\ \mu\mathrm{m}$, $7.2\ \mu\mathrm{m} < l_\mathrm{LC} < 9.7\ \mu\mathrm{m}$; $|\alpha_\mathrm{NC}| < 24.5$ deg, and $|\alpha_\mathrm{LC}| < 26.5$ deg) for both types of LMs.

In addition, we calculate $<\cos(\theta(L))>$, where $\theta(L)$ represents an angle between a first LM and a second LM that is N particles away, such that $L = Nl_0$, and averaging over the ensemble is performed (**Fig. 2.4C**). By fitting to a decaying exponential function, $<\cos(\theta(L))> = \exp(-L/L_\mathrm{p})$, we find that the resulting persistence lengths for NC-LMs and LC-LMs are nearly the same within one-standard-deviation uncertainties: $L_{\mathrm{p,NC}} = (267 \pm 5)\ l_{0,\mathrm{NC}}$, $L_{\mathrm{p,LC}} = (250 \pm 12)\ l_{0,\mathrm{LC}}$. This is consistent with the very similar potentials in angle for these two types in **Fig. 2.4B**.

We have also measured the extensibilities of both NC-type and LC-type steric lock-and-key bonds, and through analysis we show that these different designs lead to markedly different extensibilities. Here, the bond extensibility, an intrinsic property between two adjacent LMs related to their shapes, is differently defined than classic extensibility of molecular polymers. We quantify the extensibility between adjacent LMs by making histograms of contour length for different N between the centroids of an i-th LM and (i+N)-th LM in the same linear chain, where the index i is varied to cover the chain. We find that the average contour length $<L(N)>$ is simply linear and nearly identical for both NC-type and LC-type PLMs; this is consistent with their overall designed lengths, which are the same. Using these histograms at each N, we also calculate the standard deviation of contour length (*i.e.* spacing), σ_N. If all constituent LMs in a PLM chain would be statistically independent, under Brownian excitations, we would expect σ_N to be proportional to the square root of N. However, different cavity sizes of LMs offer different accessible microstates for NC- and LC-type PLMs, so $\sigma_{N,\mathrm{NC}}$ and $\sigma_{N,\mathrm{LC}}$ (*i.e.* widths of their respective distributions of contour length) are noticeably different. We have tried fitting these σ_N to square root of N behavior, but the quality of fit is not nearly as good as a fit with a power law of the form $\sigma_N = aN^b$ (**Fig. 2.4D**). The power law exponents controlling the growth in σ_N are similar ($b_{\mathrm{NC}} = 0.564 \pm 0.005$, $b_{\mathrm{LC}} = 0.574 \pm 0.006$); yet, the overall magnitudes are quite different ($a_{\mathrm{NC}} = 0.230 \pm 0.002$ μm, $a_{\mathrm{LC}} = 0.342 \pm 0.002$ μm), consistent with the larger cavity design and greater extensibility of the LC-type bond as compared to the NC-type bond.

By making a discrete 2D histogram of the observed inter-LM probability as a function of l and α assuming even behavior in α and fitting it using a 2D cubic spline function, we obtain a smoothed surface plot of normalized probability density $p_{\alpha l}(\alpha,l)$ for bonds between NC-type LMs obtained via particle tracking (**Fig. 2.4E**). Similarly, we also display the corresponding smoothed potential surface $U_{\alpha l}(\alpha,l)$ for NC-type bonds (**Fig. 2.4F**) obtained from the

Boltzmann factor using this probability density. Our measurements indicate that there is a nearly flat region in $U_{\alpha l}$ along the l-axis that reflects the broad anharmonic well in **Fig. 2.4A**. This 2D surface potential also provides a more complete picture of the limits of the NC-type lock-and-key junction's allowed internal degrees of freedom than the simplified 1D projections in **Figs. 2.4A** and **2.4B**.

2.3.5 Evolution from out-of-equilibrium conformations

By pre-configuring NC-type LMs having inter-LM bonds with zero intrinsic curvature into an open ring-like initial PLM conformation and releasing this far-from-equilibrium PLM, we show that the curvature distribution evolves through Brownian excitations towards equilibrium. To obtain local curvature as a function of contour length as well as distributions of local curvature, we skeletonize the observed contour associated with the centers of the LMs within the evolving PLM (**Figs. 2.5A-F**). We calculate the local curvature and colorize the backbone skeleton accordingly to encode positive (blue) and negative (red) curvature (see Materials and Methods). The single curvature of the pre-configured PLM before release is reflected initially by a delta function (red arrow) in the distribution, and this peak rapidly spreads out during a short period of time associated with partial release (*i.e.* from ≈2.4 h to ≈2.6 h) (**Fig. 2.5G**).

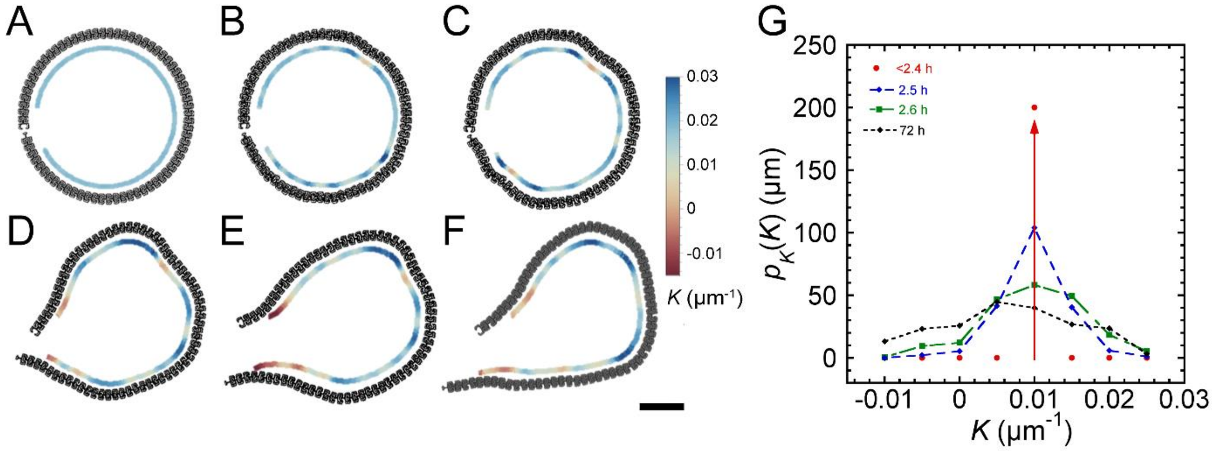

Figure 2. 5. Temporal evolution of local curvature in a linear NC-type polylithomer (PLM$_{NC}$) after release in a far-from-equilibrium initial conformation. Designed intrinsic bond curvature is zero: 71 straight-neck NC-type LMs have initial relative orientations of 5° between two adjacent LMs. Grayscale images show evolving PLM conformations at different times after adding the release solution-dispersion (RSD): (A) before onset of release: 0 h to 2.4 h; (B) partial release: 2.5 h; (C) just after total release: 2.6 h; (D) 11 h; (E) 24 h; and (F) 72 h. Scale bar for A-F: 50 μm. Inner colored lines in (A)-(F): corresponding calculated curvatures K (see text, color scale at right). (G) Probability density of curvature, $p_K(K)$, for different times after adding RSD (see inset legend). The pre-release distribution of curvature is spike-like for 0 h to 2.4 h; after complete release, the curvature becomes distributed over a wider range of K as the system evolves slowly towards $<K> = 0$.

After 24 h, there is a higher percentage of gray (*i.e.* nearly zero curvature) along the chain, as well as some small regions of red (*i.e.* negative curvature). After 72 h, even longer gray regions of nearly zero curvature can be seen (**Fig. 2.5F**). Also, curvature appears to become concentrated in a few local regions along the chain; these are separated by mostly straight regions. Because the overall size of this PLM chain exceeds the colloidal scale, its evolution towards the equilibrium conformation of a completely straight chain is very slow, and the time scale for Brownian excitations to straighten out the remaining localized regions of higher curvature is longer than our observation time (216 h).

2.4 Discussion and Conclusions

We have designed and lithographically fabricated polylithomers as dynamically interesting and readily visualizable colloidal mimics of a wide variety of polymers, wherein constituent lithomers are connected by steric lock-and-key linkages without any need for programmable complex attractive interactions through patchy molecular functionalization of particle surfaces. Beyond existing synthetic molecular polymer structures, such as highly branched polymers and dendrimers, our top-down approach has enabled us to access new types of polymer structures, such as a crosslinked chiral spiral, that have not been previously synthesized in either molecular or colloidal form to the best of our knowledge. Thus, without inducing in-plane attractions between lithographic particles and instead by pre-configuring steric lock-and-key shapes with effectively hard in-plane interactions, we have shown that litho-PAMs is not limited only to densely patterned non-sterically-interlocking particles, such as a quasi-crystal of Penrose kites and darts, that otherwise melt and lose memory of their initial configurations if external confining walls are removed. From a micro-mechanical point of view, PLMs are effectively mobile colloidal linkages that fluctuate and exhibit a superposition of damped transverse and longitudinal wavelike motions as a consequence of LM coupling in the presence of broadband Brownian excitations.

In order to obtain such a wide variety of PLM structures, we have designed different sub-particle features into LMs, conferring different types of LMs that can have shape-controlled steric bonding characteristics. These sub-particle features are reminiscent of secondary structures of folded proteins. For example, crosslinking-LMs at branching points can give rise to LMs having multiple heads and/or multiple tails, rather than the most basic and prevalent single head-tail LM design. As an illustration of this, the fluctuating 2D mesh (**Fig. 2.2H**) is composed of 3-head LMs and 2-tail LMs. Also, even regarding the single head-tail LM design, we have varied the angle between the head and the tail through the connecting neck, thereby imposing a lithographically pre-designed intrinsic curvature, which can be spatially varied, into linear chains of LMs, as we have shown with the crosslinked chiral spiral. Beyond this, by controlling the size of the cavity in the tail of single head-tail LMs, as we have demonstrated through particle tracking microscopy experiments after release, even relatively small differences in the cavity lengths can result in readily measurable differences in the extensibilities of PLMs composed of NC-type and LC-type LMs. Thus, lithographic design and pre-assembly of shapes of LMs can be used to control the nature of inter-LM bonding, including aspects of multi-valency, chirality, extensibility, flexibility, and intrinsic curvature. This degree of control goes well beyond the topology and overall structures of different types of PLMs, which could be extended to include self-similar 'fractal' polymers.

Our experiments involving NC-type and LC-type PLMs show that PLMs offer access to an interesting and unusual range of polymer structures that have extensible bonds which can be controlled by top-down design. The nearly-hard interactions between the head of one LM and the cavity of an adjacently bonded LM lead to a flattened, dominantly quartic, rather than quadratic, inter-LM potential associated with longitudinal extension and compression. Whereas molecular polymer systems have covalent bonds between atoms that are effectively inextensible, even larger extensibility in inter-LM bonds within PLMs could be programmed through the design of even longer cavity features in constituent LMs. Thus, through PLMs, it is possible to make and study polymers that are semi-flexible yet have significant extensibility; this is especially interesting in 2D systems for which Brownian excitations between noninterlocking particles at high densities are known to give rise to long-wavelength Mermin-Wagner fluctuations. In general, the influence that extensible steric lock-and-key bonds can have on Kosterlitz-Thouless phenomena (26) and Goldstone modes (27) in dense 2D Brownian systems of mobile tiles remains intriguing, and our approach now makes such systems accessible.

Beyond equilibrium fluctuations, our example of the evolution of local curvature in a ring-like initial PLM conformation of lock-and-key LMs, which are all connected by steric bonds that have zero intrinsic curvature, highlights the potential for making and studying the behavior of local entropy flux (*i.e.* caliber (28, 29)) in far-from-equilibrium systems. Because the best forms of modern stepper lithography can achieve minimum feature sizes more than an order of magnitude below the limit of the 5x-reduction Hg i-line optical stepper that we have used, we anticipate that it will be possible to construct systems that are composed of much smaller LMs and therefore have much more rapid temporal evolution under Brownian excitations. Moreover, we also anticipate that linear and non-linear responses of individual PLMs to externally applied fields, particularly flow fields and electromagnetic fields, will be interesting to study.

While the conceptual development and experimental demonstrations of PLMs herein represent major advances in interconnected dynamic systems of mobile linkages that are small enough for entropic effects (*i.e.* Brownian excitations) to be important, as they are for molecular polymers, there are some limitations in the current examples that future work would could potentially overcome. Reducing the persistence length and approaching the limit of flexible polymers could potentially be achieved through differently designed LMs and their interconnections. Other nanolithography techniques, not just optical stepper lithography, could be used to make PLMs, and these could be used to reduce the sizes of LMs and the overall PLMs in order to speed up conformational dynamics resulting from Brownian excitations. For such smaller PLMs, using simple brightfield microscopy would not necessarily yield high quality tracking information about sub-particle features, so measuring dynamics using a real-time or high-speed visualization method that offers higher spatial resolution would likely also be necessary. The visualization of such smaller PLMs to sub-LM detail could involve the use of fluorophores or other molecular markers in the composition of the LMs, and it might involve alternative techniques such as dark-field, super-resolution, or scanning probe microscopies.

We expect that our findings will spark new efforts in several different directions. Theories and simulations of polymer dynamics will need to be extended in order to treat anharmonic extensible inter-LM steric bonds. Related to this, longer wavelength longitudinal modes of motion are readily observable in the systems of semi-flexible PLMs that we have already generated, and these need further theoretical statistical characterizations. Different head and cavity designs would enable a more thorough exploration of the dynamics of extensible polymers, both in experiments as well as in theory. Interactions between locally proximate PLMs would also be possible and interesting to study. Confinement of PLMs within certain shapes of rigid confining walls could also be accomplished to see how this confinement influences conformations. Tuning in-plane interactions between the surfaces of LMs to be other than hard, for instance through size and concentration of other depletion agents, would also be possible and could significantly influence the inter-LM potentials. Overall, the future is bright in regards to expanding the variety and scope of experimentally realizable colloidal mimics of molecular polymer systems and polymer dynamics based on the approaches herein.

Appendix A. Description for supplementary movies

Movie 2.1. Equilibrium Brownian fluctuations of a 4-arm star polylithomer. A set of steric lock-and-key lithomer tiles, made of crosslinked SU8 and preconfigured as a 4-arm star polylithomer by optical stepper lithography, are attached initially to a solid Omnicoat release layer on a glass wafer. After adding a basic aqueous release solution–dispersion (RSD) containing a depletion agent (see Materials and Methods), the Omnicoat begins to dissolve. Individual lithomers begin to release and become mobile after about one hour. Time-lapse transmission optical microscopy reveals equilibrium Brownian fluctuations of this semi-flexible polylithomer star after full release. This star polylithomer remains intact in a monolayer just above the wafer and does not disassemble as a consequence of the in-plane pre-assembled structure of lock-and-key lithomer tiles and also the out-of-plane induced depletion attraction between each tile and the wafer. The coupled dynamics of these steric lock-and-key tiles lead to a superposition of wavelets along the arms, which are evident in response to the ongoing Brownian excitations. Acquisition: 1 frame every 120 s. Acquisition time interval: 480-1100 min (*i.e.* 310 frames), where 0 min corresponds to the addition of the RSD. Video playback: duration 31 s at 10 frames per second (FPS). Scale bar: 50 μm. Camera: Nikon D5300.

Movie 2.2. Release kinetics of a branched polylithomer. A branched polylithomer, composed of a linear backbone and six symmetric side-arms preconfigured as interdigitating lock-and-key lithomer tiles, is initially attached to a solid Omnicoat release layer on a glass wafer. After adding RSD, dissolution of the Omnicoat layer mobilizes these tiles, and a depletion agent keeps these tiles in a monolayer just above the wafer; lithomer release begins to happen after about 10 min. Time-lapse transmission optical microscopy reveals the initial release and later equilibrium Brownian fluctuations of this semi-flexible branched polylithomer, providing the resolution necessary to determine positions and orientations of all monomer tiles precisely and accurately by video particle tracking. See **Figs. 2A** and **2B** for details. Acquisition: 1 frame every 120 s. Acquisition duration: 0-30 h (*i.e.* 900 frames). Video playback: duration 90 s at 10 FPS. Scale bar: 50 μm. Camera: Nikon Z7.

Movie 2.3. Brownian fluctuations of a 3-bridge chiral(-) spiral polylithomer. A spiral polylithomer is composed of lock-and-key lithomer tiles, which have been designed with intrinsic curvatures that vary gradually along the primary chain. Three semi-flexible bridges, resembling secondary structures, couple different selected lithomers within this spiral together. Tile release begins to happen about 6 h after adding RSD. Time-lapse transmission optical microscopy reveals the initial release and later equilibrium Brownian fluctuations of this semi-flexible 3-bridge chiral-spiral polylithomer; the designed intrinsic curvatures of lithomers and interconnecting bridges maintain the spiral's overall conformation and inhibit its straightening. See **Figs. 2C** and **2D** for detailed steric pictures. Acquisition: 1 frame every 120 s. Acquisition duration: 260-880 min (*i.e.* 310 frames). Video playback: duration 31 s at 10 FPS. Scale bar: 50 μm. Camera: Nikon D5300.

Movie 2.4. Brownian fluctuations of a polylithomeric 3-2-2-2 dendrimer. This highly branched polylithomer, inspired by dendrimers, is composed of short chains of simple head-tail, lock-and-key polylithomer tiles that are linked together at junction points by mono-cavity, di-head branched tiles and a central tri-head tile. Tile release begins to occur about 15 h after adding RSD. Time-lapse transmission optical microscopy reveals a greater degree of spatial motion of terminal end-chains as compared to central core-chains. See **Figs. 2E** and **2F** for details. Acquisition: 1 frame every 120 s. Acquisition duration: 860-1540 min (*i.e.* 340 frames). Video playback: duration 34 s at 10 FPS. Scale bar: 50 µm. Camera: Nikon Z7.

Movie 2.5. Release kinetics of a 2D mesh polylithomer. This two-dimensional honeycomb mesh polylithomer is made of highly interdigitating lock-and-key di-cavity and tri-head lithomer tiles. Release begins to happen about 3.3 h after adding RSD. Time-lapse transmission optical microscopy reveals the initial release and later equilibrium Brownian fluctuations of this mesh. See **Figs. 2G** and **2H** for details. Acquisition: 1 frame every 120 s. Acquisition duration: 2-30 h (*i.e.* 840 frames). Video playback: duration 84 s at 10 FPS. Scale bar: 50 µm. Camera: Nikon Z7.

References

1. R. J. Young, P. A. Lovell, *Introduction to polymers* (CRC press, 2011).
2. A. Hirao *et al.*, Precise syntheses of chain-multi-functionalized polymers, star-branched polymers, star-linear block polymers, densely branched polymers, and dendritic branched polymers based on iterative approach using functionalized 1,1-diphenylethylene derivatives. *Prog. Polym. Sci.* **30**, 111-182 (2005).
3. S. T. Milner, Polymer brushes. *Science* **251**, 905 (1991).
4. P. W. K. Rothemund, Folding DNA to create nanoscale shapes and patterns. *Nature* **440**, 297-302 (2006).
5. Z. Li, Y. Zhang, P. Fullhart, C. A. Mirkin, Reversible and chemically programmable micelle assembly with DNA block-copolymer amphiphiles. *Nano Lett.* **4**, 1055-1058 (2004).
6. K.-F. Arndt, T. Schmidt, R. Reichelt, Thermo-sensitive poly(methyl vinyl ether) micro-gel formed by high energy radiation. *Polymer* **42**, 6785-6791 (2001).
7. P. Li *et al.*, Assembly of a porous supramolecular polyknot from rigid trigonal prismatic building blocks. *J. Am. Chem. Soc.* **141**, 12998-13002 (2019).
8. M. T. Nguyen, D. P. Ferris, C. Pezzato, Y. Wang, J. F. Stoddart, Densely charged dodecacationic [3]- and tetracosacationic radial [5]catenanes. *Chem* **4**, 2329-2344 (2018).
9. T. G. Mason, J. Bibette, D. A. Weitz (1998) Relaxation of linear chains of attractive colloidal droplets. in *APS March Meeting Abstracts*.
10. R. Dreyfus *et al.*, Microscopic artificial swimmers. *Nature* **437**, 862-865 (2005).

11. K. Zhao, T. G. Mason, Directing colloidal self-assembly through roughness-controlled depletion attractions. *Phys. Rev. Lett.* **99**, 268301 (2007).
12. T. G. Mason, Osmotically driven shape-dependent colloidal separations. *Phys. Rev. E* **66**, 060402 (2002).
13. D. J. Ashton, R. L. Jack, N. B. Wilding, Self-assembly of colloidal polymers via depletion-mediated lock and key binding. *Soft Matter* **9**, 9661-9666 (2013).
14. H.-Y. Chang *et al.*, Assembly of lock-and-key colloids mediated by polymeric depletant. *Langmuir* **31**, 13085-13093 (2015).
15. Y. Wang *et al.*, Three-dimensional lock and key colloids. *J. Am. Chem. Soc.* **136**, 6866-6869 (2014).
16. C. A. Mirkin, R. L. Letsinger, R. C. Mucic, J. J. Storhoff, A DNA-based method for rationally assembling nanoparticles into macroscopic materials. *Nature* **382**, 607-609 (1996).
17. S.-J. Park, A. A. Lazarides, J. J. Storhoff, L. Pesce, C. A. Mirkin, The structural characterization of oligonucleotide-modified gold nanoparticle networks formed by DNA hybridization. *J. Phys. Chem. B* **108**, 12375-12380 (2004).
18. M. B. Bannwarth *et al.*, Colloidal polymers with controlled sequence and branching constructed from magnetic field assembled nanoparticles. *ACS Nano* **9**, 2720-2728 (2015).
19. S. Y. Park *et al.*, DNA-programmable nanoparticle crystallization. *Nature* **451**, 553-556 (2008).
20. P.-Y. Wang, T. G. Mason, A brownian quasi-crystal of pre-assembled colloidal penrose

tiles. *Nature* **561**, 94-99 (2018).

21. S. M. Bhattacharjee, A. Giacometti, A. Maritan, Flory theory for polymers. *J. Phys.: Condens. Matter* **25**, 503101 (2013).

22. T. Hugel *et al.*, Elasticity of single polyelectrolyte chains and their desorption from solid supports studied by afm based single molecule force spectroscopy. *Macromolecules* **34**, 1039-1047 (2001).

23. X. Liu, G. H. Pollack, Mechanics of F-actin characterized with microfabricated cantilevers. *Biophys. J.* **83**, 2705-2715 (2002).

24. F. Manca *et al.*, Elasticity of flexible and semiflexible polymers with extensible bonds in the Gibbs and Helmholtz ensembles. *J. Chem. Phys.* **136**, 154906 (2012).

25. K. Zhao, R. Bruinsma, T. G. Mason, Entropic crystal–crystal transitions of Brownian squares. *Proc. Natl. Acad. Sci. U.S.A.* **108**, 2684-2687 (2011).

26. J. Kosterlitz, D. Thouless, Odering, metastability and phase transitions in two-dimensional system. *J. Phys. C: Solid State Phys.* **6**, 1181 (1973).

27. J. Goldstone, Field theories with « superconductor » solutions. *Il Nuovo Cimento (1955-1965)* **19**, 154-164 (1961).

28. M. J. Hazoglou, V. Walther, P. D. Dixit, K. A. Dill, Communication: Maximum caliber is a general variational principle for nonequilibrium statistical mechanics. *J. Chem. Phys.* **143**, 051104 (2015).

29. E. T. Jaynes, The minimum entropy production principle. *Annu. Rev. Phys. Chem.* **31**, 579-601 (1980).

Chapter 3 – Shape-Controlled Extensibility and Chirality of Semi-Flexible Steric Lock-and-Key Polymers

3.1 Introduction

The structures and properties of molecular polymers depend on the types of monomers, on bonding structures, and also on the nature of the chemical bonds (1). While many different molecular polymers have been synthesized exclusively using bottom-up routes over many decades, polymers made of colloidal building blocks have been created either by bottom-up self-assembly (2, 3) or top-down pre-assembly (4). Colloidal polymers can be customized to have interesting structures and properties that are difficult to access in molecular polymers, thereby offering opportunities for scientific studies that go beyond their molecular counterparts.

Such colloidal polymers also offer certain advantages experimentally since these can be visualized optically down to the monomer scale. For example, in colloidal polymers composed of top-down, lithographic monomers in pre-configured lock-and-key morphologies, steric bonds between monomers can lead to unusual extensibility and longitudinal chain fluctuations (4). These mobile Brownian colloidal tiles, known as polylithomers, can be pre-designed to have a wide variety of structures, including chiral spirals, dendrimers, and brushes. Moreover, the steric bonds are effectively designed through sub-particle geometrical features of the particles' interlocking heads and tails, leading to control over persistence length, intrinsic curvature, and extensibility, which are not available to other colloidal polymers from self-assembly. While there are some limited examples in this initial experimental work, through simulations it is possible to create and assess a wider range of bond possibilities rapidly. So, performing simulations on a broadly diverse set of designed colloidal steric lock-and-key polymers represents an interesting direction that has the potential for revealing unusual and interesting polymer behavior beyond what is already commonly known for semi-flexible molecular polymers.

The classic freely jointed chain (FJC) and worm-like chain (WLC) models assume that the covalent chemical bonds between monomers are inextensible; the extensibility of the polymer chain results from rotations of bond angles. This rotational flexibility causes different chain rigidity, characterized by persistence length, as can be revealed from exponentially decaying orientational correlation functions. Computer simulations have been carried out using symmetric potentials based on the WLC model and have re-examined the orientational correlation function, revealing regimes that follow different, non-exponential decays (5, 6).

While simulations of more complex coarse-grained models of chiral polymers, such as DNA, have been reported to be in accord with the WLC model (7), and their colloidal mimics have been synthesized (8), an asymmetric bonding potential within the simple WLC model has not yet been thoroughly investigated. Although extensibilities of chemical bonds have been observed under large applied forces (9-11), such high-load extensibilities are not of primary importance for free-standing polymers subjected only to gentle Brownian excitations. In molecules, mechanical bonds are linkages between sets of molecular motifs in chains (12) and networks (13) of mechanically interlocked molecules (MIMs) (14, 15) such as polycatenanes. Molecular dynamics simulations using coarse-grained bead-spring Rouse model (16) have revealed their mechanical and dynamical properties such as stiffness (17), strength (18), and relaxation time (19). Strikingly, lithographically designed steric bonds, which may be alternatively classified as topological or mechanical bonds, can also possess both longitudinal and orientational degrees of freedom. All of these advances call for a more detailed and general study of polymer systems having diverse bonds or linkages with a wider range of extensibilities and symmetries, dictated by top-down lithographic design, not by chemical bonding.

Here, through Monte Carlo (MC) simulations, we demonstrate that sterically bonded colloidal polylithomers provide access to a broader range of polymer properties that lie beyond conventional molecular polymers as a consequence of geometrically controllable, complex, lock-and-key linkage-structures. Such steric bonds are a direct consequence of the designed shapes and sizes of the heads and cavities of the monomers; these sub-particle steric lock-and-key features have been tailored specifically to prevent adjacent monomers from disassembling through Brownian excitations from their initially interlocked state. These steric lock-and-key polylithomers could alternatively be called mechanically interlocked colloids (MICs). Because the shapes of mononers cover an enormous range of possibilities, and because monomer bond-valencies can likewise be controlled, we restrict our attention to linear homopolymers composed of one type of monomer having a singlehead and a single tail. Through Monte Carlo simulations, we efficiently generate self-avoiding conformations and study equilibrium ensembles of a wide variety of colloidal polymers having extensible, chiral, and bifurcated angular bonds that are atypical of molecular polymers. We show that the chirality of a polymer chain can be de-coupled from its persistence length by subtracting the mean accumulated value of relative orientation when calculating the orientational pair correlation function. In addition, we show that chiral bonds, arising from asymmetry in the cavity-designs, cause more frequent coil-like conformations, characterized by shorter end-to-end distances and radii of gyration. We also quantify the fluctuations in local orientation along the chain by the standard deviation and show that bonds associated with bifurcated cavity designs result in larger fluctuations of local orientations and curvatures. Also, more longitudinally extensible bonds result in more rapid decays of pair correlation functions along the contour of a given chain. Overall, our simulations indicate that an interesting and broad range of polymer behavior can be anticipated in future experimental systems of polylithomers that include higher levels of complexity in the designs of lock-and-key monomers.

3.2 Materials and Methods

3.2.1 Determining phase space

As shown in **Fig. 3.1A**, each monomer is a polygon of 20 or 23 (NCS2) vertices. The neck is designed to be long enough that the relative motion of two nearby monomers will not be restricted by the collision of their two tails. The tail is designed to have a concave cavity with an opening that is slightly larger than the width of the neck, so that when a second monomer is inserted, approximately the neck only has two degrees of freedom, which are the separation (l) and the orientation (α). We ignore the change of vertical distance by different orientations (Strictly speaking, the contact and relative motion of a nearby neck and the tip-like terminals should be made of a bearing with a channel. The bearing can rotate while the neck can slide in the channel). We sample the phase space (l, α) by fixing l and decreasing α from 1 (rad) until there is no possible intersection between two monomer polygons (we do not check the intersection of the neck and the terminals). For NCS2, we also increase α from 0 because of the bifurcate shape. We repeat this process for different l in a reasonable region.

3.2.2 Monte Carlo simulation of chain conformations

Molecular dynamics and Brownian dynamics simulation are commonly implemented in computational studies (20-22), but to study equilibrium properties Monte Carlo methods are usually sufficient. Inside the corresponding phase space, we generate a sequence of random number pairs (l, α) according to which a new monomer is placed. If there is no intersection along the existing chain, this new monomer position is accepted; otherwise a new random pair is generated and tested. To avoid infinite loop because of spiral-like conformations, the existing chain will be reset after several unsuccessful trials. Accepted (l, α) pairs are recorded for further analysis. Each chain consists of 100 monomers. This procedure is repeated 5000 times for each monomer type.

3.3 Results

3.3.1 Design and phase space

To show different polymeric conformations and properties resulting from steric lock-and-key linkages having extensibility, fore-and-aft symmetry, chirality, and bifurcated angles, we have designed eight different monomers (see shapes and labels in **Fig. 3.1A**). Each monomer (*i.e.* lithomer) is made of a rectangular head, a slender rectangular neck, and a tail having a concave cavity that is larger than the head and has an opening that is slightly larger than the width of the neck. We vary only the internal shapes of the cavities; the head and neck are the same for all designs. The high degree of confinement of the inserted neck of one monomer through the tail-opening of an adjacent monomer allows only relative extensional-compressional sliding and rotation of the adjacent monomer (see **Materials and Methods** for details). Therefore, each bond between monomers has two degrees of freedom (**Fig. 3.1B**): (i) the separation, l, between adjacent monomers, which is related to a monomer's length, L, and the insertion distance, s, of the head into the tail of the adjacent monomer by: $l = L - s$, and (ii) the relative orientation, α, between these adjacent monomers. We customize the set of accessible states (l, α) in phase space by changing the sizes and shapes of the cavity; for example, the NC> monomer has more accessible states at longer insertion distances compared with NC= **(Fig. 3.1C**). Monomers with chiral cavities, NC/ and NC\, can be thought of as being

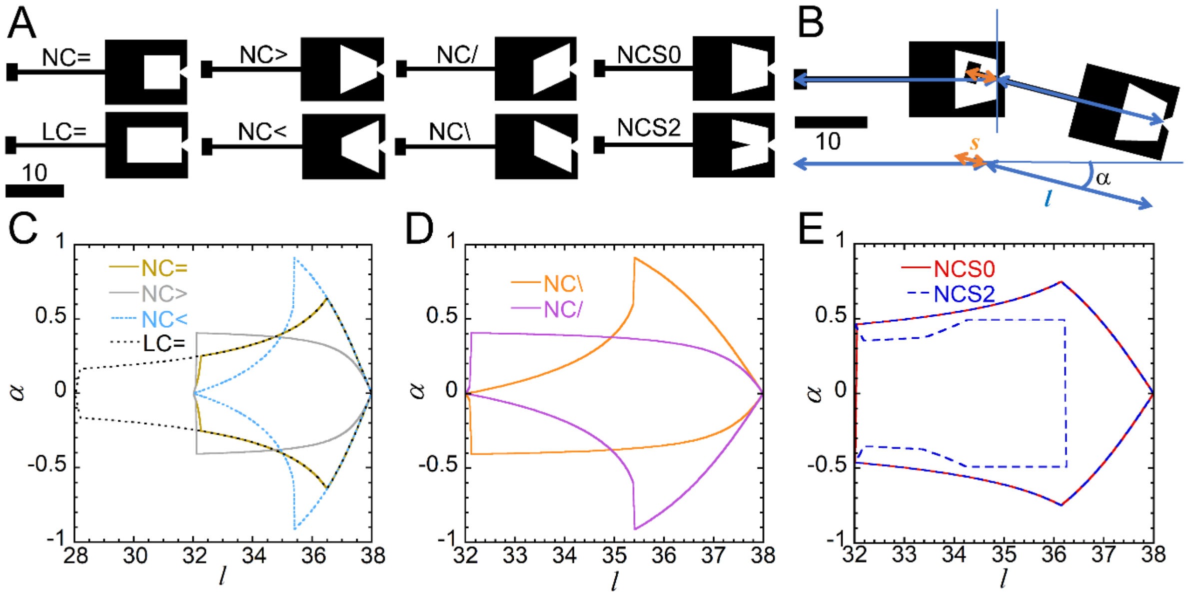

Figure 3. 1. Lithomer designs and accessible states of lock-and-key lithomer pairs determined by collision detection. (A) Eight lithomer designs showing differences in (from left to right): cavity length, fore-aft asymmetry, chirality, and split orientations. Scale bar: 10 dimensionless units. (B) Each lithomer-bond has two degrees of freedom: (i) separation (l) and (ii) relative orientation (α). The lithomer length is $M = s+l$, where s is the insertion distance. The minimum s is the width of the head. (C) Accessible states of NC=, NC>, NC< and LC= (regions inside corresponding lines: see legend). (D) Accessible states of chiral NC/ and NC\. The lines of the same color are mirror reflections of the other. (E) Accessible states of NCS0 and NCS2. NCS2 is designed to create a split distribution of angles and an accessible region that resembles a horse-shoe by bifurcation.

composed of half of NC> and half of NC<. Consequently, the shapes of their phase spaces reflect such combination (**Fig. 3.1D**). NCS2 has a split phase space resulting from the exclusion of some accessible states at shorter l; an internal protrusion has been inserted into the middle of the cavity to create the bifurcation. By contrast, NCS0 lacks this protrusion (**Fig. 3.1E**).

Alternatively, we directly calculate the 2D phase-space from designed geometries of the head and the cavity (**Figs. 3.2A** and **3.2B**). This phase space is encompassed by three boundary line segments, determined by geometrical conditions of collisions between different vertices of the head with different edges of the cavity. The width of the neck is assumed to be

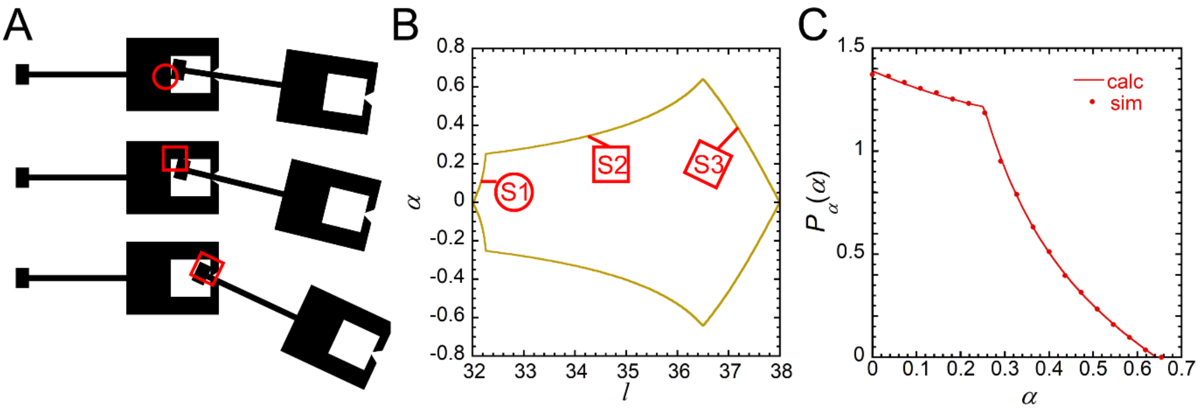

Figure 3. 2. Calculating accessible states by considering intersections of head and cavity geometries: NC=. (A) Three regimes where accessible states are controlled by different vertices of the rectangular head. (B) Their corresponding curvilinear boundaries in phase space, encompassed by the line segments of Eqs. S1-S3 (mirror-symmetric lower lines for $\alpha < 0$ are also provided to show an entire closed region of accessible states). (C) Comparison of the calculated PDF (line) with the simulated PDF (dots) for orientations of NC=.

negligible for simplicity. For NC= and LC= with rectangular cavities, these boundary line segments can be parametrized by:

$$l = F_1(\alpha) = M - [w - (b/2)\sin(\alpha)]/\cos(\alpha) \qquad 0 < \alpha < \alpha_1 \text{ and } M - w < l < l_1 \quad \text{(S1)}$$

$$= F_2(\alpha) = M - [b - (b/2)\cos(\alpha)]/\sin(\alpha) \qquad \alpha_1 < \alpha < \alpha_2 \text{ and } l_1 < l < l_2 \quad \text{(S2)}$$

$$= F_3(\alpha) = M - [c + (b/2)\tan(\alpha)] \qquad 0 < \alpha < \alpha_2 \text{ and } l_2 < l < M - c\,. \quad \text{(S3)}$$

Here, $M = 40.5$ is the fixed length of each monomer, w is the length of the cavity (8.5 for NC=, 12.5 for LC=), $b = 4$ is the height of the head, and $c = 2.5$ is the width of the head. Boundary-values $(\alpha_1, l_1) = (0.2497, 32.24)$ are found by equating Eqs. S1 and S2; also, boundary-values $(\alpha_2, l_2) = (0.6435, 36.50)$ are found by equating Eqs. S2 and S3.

Next, we analytically determine the probability density function (PDF) for both separations and orientations. As an example, we provide the calculation of $P_\alpha(\alpha)$ for NC= here. Based on the relative positions and applicable endpoints of Eqs. S1-S3, we find:

$$P_\alpha(\alpha) = A[F_3(\alpha) - F_1(\alpha)] = A\{[w - (b/2)\sin(\alpha)]/\cos(\alpha) - [c + (b/2)\tan(\alpha)]\} \qquad 0 < \alpha < \alpha_1 \tag{S4}$$

$$= A[F_3(\alpha) - F_2(\alpha)] = A\{[b - (b/2)\cos(\alpha)]/\sin(\alpha) - [c + (b/2)\tan(\alpha)]\} \qquad \alpha_1 < \alpha < \alpha \tag{S5}$$

where $A = 0.2315$ is the normalization factor. We find a nearly exact match between the calculated and the simulated $P_\alpha(\alpha)$ (see **Fig. 3.2C**). From these PDFs, we calculate the effective bonding potential energies, $U_\alpha(\alpha) = -k_B T$ In($P_\alpha(\alpha)$), assuming Boltzmann statistics. $P_l(l)$ is calculated from the inverse function $\alpha = F^{-1}(l)$; $P_l(l)$ is directly proportional to $F^{-1}(l)$ (see **Fig. 3.2B**). Once the effective potential energies of the steric bonds have been calculated, polymeric properties, such as persistence length, are determined.

3.3.2 Typical conformations for chains of different designs

For each different monomer shape, conformations of chains are constructed by self-avoidance MC growth (23) based on that shape's calculated phase space. Since self-avoidance substantially affects very long chains in 2D, our MC simulations focus on shorter chains having numbers of monomers, $N \leq 100$, yet from thousands of ensembles. We display conformations of different chains by showing normalized unitless curvatures (κl_{max}) and separations (l/l_{max}). The curvature κ at each monomer is calculated as the inverse radius of a circle uniquely determined by the centers of that monomer and its two neighbors; we define l_{max} to be the maximum possible separation between two adjacent monomers. Typical chains of NC> and NC< show different statistics of separations (see **Figs. 3.3A** and **3.3B**, respectively). Overall, consistent with their respective designs, NC> yields smaller separations (more cyan monomers),

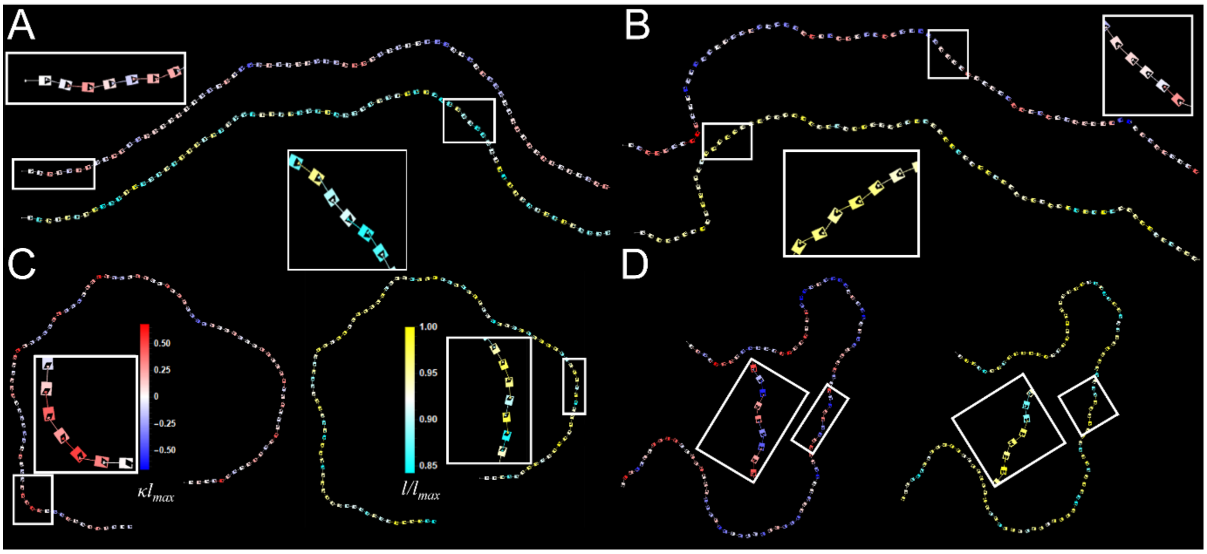

Figure 3. 3. Example conformations of chains of several different lithomers, characterized by normalized curvatures κl_{max} (blue - to white 0 to red +) and separations l/l_{max} (cyan to white to yellow): (A) NC> showing more smaller (cyan) separations; (B) NC< showing more bigger (yellow) separations; (C) chiral NC\ showing a counter-clockwise conformation as a result of a positive mean orientation; (D) NCS2 showing fewer zero values and more extreme + and - colors because of the split cavity design, influencing both local curvatures and separations.

whereas NC< yields larger separations (more yellow monomers). **Fig. 3.3C** shows a typical conformation of a NC\ chain. This clockwise conformation (using the pointing direction of the initial monomer at the starting end of the chain as a reference) is a result of stronger weighting in the distribution towards positive curvatures (red), reflecting the asymmetric cavity design of NC\. Its mirror-reflection, NC/, has a similar distribution but of opposite-sign curvatures. **Fig. 3.3D** shows a typical conformation of a chain of the bifurcated cavity design, NCS2, which exhibits larger fluctuations of both curvatures and separations (see **Figs. 3.4B** and **3.4C**) compared with the simpler NCS0 that has no internal cavity features.

3.3.3 Bonding probability density distribution

From MC ensembles of different chain conformations for particular monomers, we calculate 1D probability density distributions (PDFs) of the respective separations and

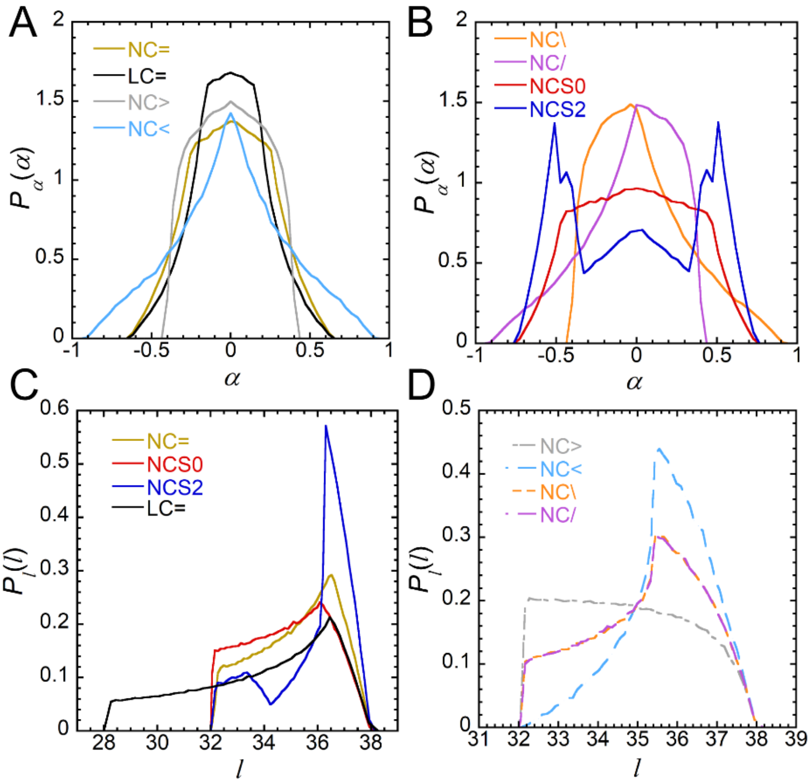

Figure 3. 4. 1D cumulative probability densities of orientations (A) and (B) and separations (C) and (D). Two plots are shown for each degree of freedom to avoid undue overlap of the numerous curves. Curves for NC\ and NC/ are combinations of NC> and NC<.

orientations. Because of self-avoidance, these distributions differ slightly from statistical results based on only two monomers, which can be calculated analytically from the corresponding phase space (**Fig. 3.2**). The shapes of these distributions are complex, reflecting the underlying complexity of designed sub-particle features in the various monomer geometries. In addition, separations and orientations are not independent but instead coupled together. For example, the PDF of LC= differs from that of NC=, not only through its broader separation (**Fig. 3.4C**), but also through its sharper distribution of orientations (**Fig. 3.4A**). This is because LC= has a greater range of accessible orientations around zero, despite the same maximum and minimum orientations. Also, besides the fore-and-aft asymmetry in the distribution of separations of NC> and NC< (**Fig. 3.4D**), NC< can have an even broader distribution of orientations at large separations. Therefore, this expands the range between the maximum and the minimum accessible orientations. Consequently, NC< would have fewer accessible states of orientations around zero (**Fig. 3.4A**). Because the designs of NC\ and NC/ effectively combine portions of NC< and NC>, the PDFs of NC\ and NC/ contain corresponding shapes of the PDFs of NC< and NC> (**Figs. 3.4B** and **3.4D**). Interestingly, the bifurcated cavity in the tail of NCS2 splits not only the distribution of orientations (**Fig. 3.4B**), but also the distribution of separations (**Fig. 3.4C**), leading to highly fluctuating conformations.

3.3.4 Chirality and bifurcation

The orientational PDFs of NC\ and NC/ result in linear growth of cumulative orientations $<\theta(N)>$ having slopes of the same magnitude but opposite sign (**Fig. 3.5A**); here, $<\theta(N)>$ is the relative orientation of the N-th monomer with respect to a starting monomer averaged over the ensemble of chains generated. Chains made using chiral cavities have higher probabilities of forming coil- or spiral-like conformations (**Fig. 3.3C** and **Fig. 3.6A**). We characterize the fluctuations of chain orientations by the standard deviations of cumulative orientations, $\sigma_\theta(N)$, which follow the square-root combination rule of random variables for small N (**Fig. 3.5B**). However, at larger N, especially for designs that more often trigger self-avoidance restrictions (e.g. NC\ and NC/ by coil-like conformations from chirality, and NCS2 by highly fluctuating orientations), the growth of $\sigma_\theta(N)$ deviates positively from this square-root rule (**Fig. 3.6B**). This is because the MC growth of these designs is more likely to become trapped in an infinite loop and hence must be discarded (see **Materials and Methods** for details).

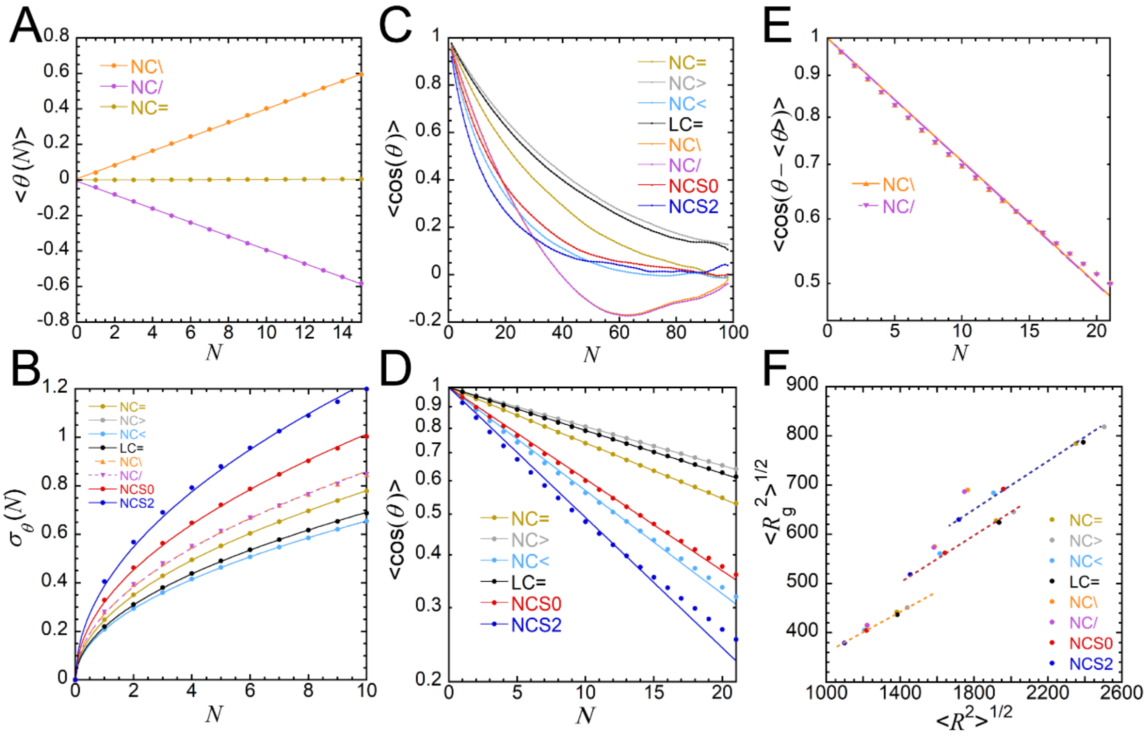

Figure 3. 5. Chirality and extensibility analysis. $\theta(N)$ is the orientation of N-th monomer with respect to the first monomer, i.e. $\theta(N) = \alpha(1) + \alpha(2) +…+ \alpha(N)$. (A) Growth of mean cumulative angles. Linear fit of NC=, NC\ and NC/. NC\ and NC/ have non-zero, opposite but nearly equal values. (B) Square-root power law fit of standard deviation $\sigma_\theta(N)$ by first 10 monomers. Larger numbers deviate from square-root growth because of self-avoidance. $\sigma_\theta(N)$ of NCS2 is larger than NCS0 because of split distribution. NC\ and NC/ are almost identical. (C) Decay of orientational correlation function. NC\ and NC/ have negative values because of chirality. (D). Fit of the first 20 monomers in (C) to exponential decays. (E) Modified orientational correlation function by $<\cos(\theta–<\theta>)>$ of NC\ and NC/. These functions also undergo an exponential decay initially. (F) Root mean square end-to-end distance $<R^2>^{1/2}$ and root mean square radius of gyration $<R_g^2>^{1/2}$. Blue dashed line: linear trend when $N = 100$, $k = 0.233$; Red dashed line: linear trend when $N = 75$, $k = 0.223$; Orange dashed line: linear trend when $N = 50$, $k = 0.209$. Chiral chains deviate from linear trend because of more coil-like conformations having smaller end-to-end distances and radii of gyration.

Next, we apply the traditional orientational analysis to the generated ensembles of semi-flexible chains to determine persistence length. **Fig. 3.5C** shows the decay of the orientational correlation function $<\cos(\theta(N))>$. For all designs, at small N, $<\cos(\theta(N))>$ decays from unity as expected; yet, at larger N, strikingly, chiral designs cause $<\cos(\theta(N))>$ to become negative, go through a minimum, and then rise again. Moreover, since NC> and LC= have the most concentrated and narrow distributions of orientations (**Fig. 3.4A**), their orientational correlation

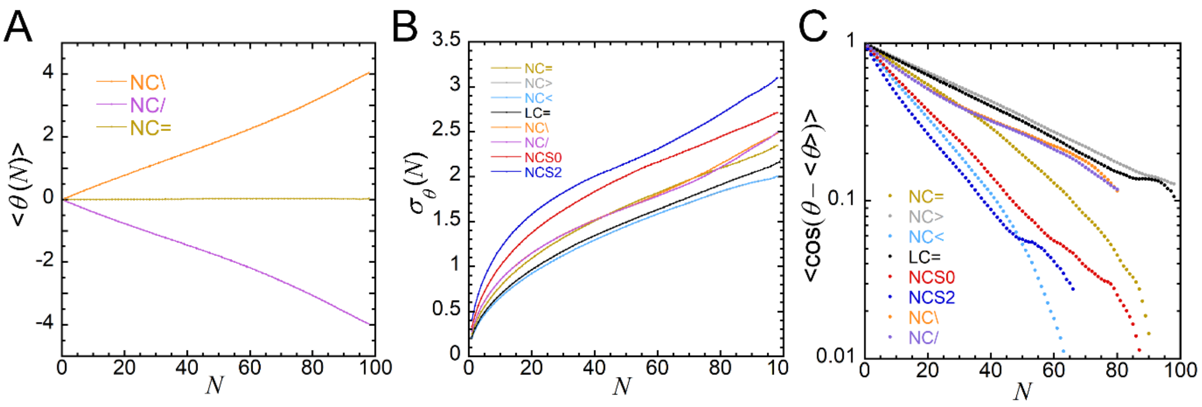

Figure 3. 6. Orientational properties at longer ranges. (A) Mean cumulative angles as a function of the number of lithomers, N, in a segment of a chain. Achiral designs have $<\theta(N)> = 0$ whereas chiral designs show either positive or negative growth. (B) Standard deviation of cumulative angle, σ_θ, versus N. NCS2 exhibits the largest fluctuations because of its split cavity design. NC\ and NC/ are almost identical. (C) Decays of orientational correlation functions corrected for designed chirality. NC/ and NC\ are modified by non-zero mean cumulative angles $<\theta>$. Exponential behavior is seen at small N and non-exponential behavior is seen at larger N. The split cavity design decays most rapidly and has the smallest effective persistence length of all cavity designs considered.

functions decay slowest; whereas NCS0 and NCS2 decay fastest due to broader orientational distributions (**Fig. 3.4B**). We fit the initial decay of $<\cos(\theta(N))>$ to an exponential decay function $\exp(-N/N_\mathrm{p})$, where N_p is proportional to the persistence length, limiting the data range up to $N = 20$ (**Fig. 3.5D**) for chains of achiral monomers. The orientational correlation functions of more orientationally flexible chains decay faster (N_p = 14.1, 17.7, 19.9, 32.9, 42.5, and 46.8 for NCS2, NC<, NCS0, NC=, LC=, and NC>, respectively). At larger N for all designs, $<\cos(\theta(N))>$ no longer follows a simple exponential decay. The non-exponential deviations at larger N have different directions in different regimes (**Fig. 3.6C**). Such deviations are a result of the correlation between monomers that are far away from each other because of possible loop-like conformations (24).

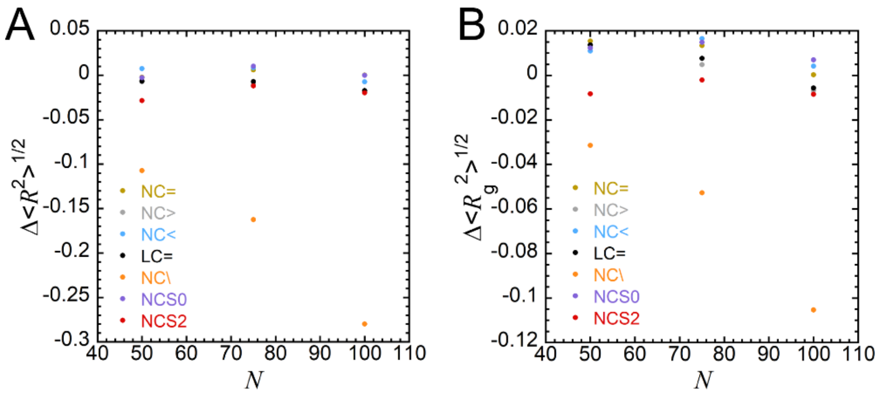

Figure 3. 7. Chain extensibility from WLC model. (A) Difference (normalized to calculated value) between calculated $<R^2>^{1/2}$ from worm-like chain (WLC) model and simulation results. Differences for achiral chains are within 3%. $<R^2>^{1/2}$ from WLC results for NC\ and NC/ are significantly larger than simulations and this difference grows with N. (B) Differences between calculated $<R_g{}^2>^{1/2}$ from WLC model and simulation results. Differences for achiral chains are within 2%. $<R_g{}^2>^{1/2}$ from WLC results for NC\ and NC/ are larger than simulations, and this difference grows with N; however, the magnitude of this difference is smaller than that of $<R^2>^{1/2}$.

Because <cos($\theta(N)$)> of chiral NC\ and NC/ decay more rapidly and even become negative due to the non-zero cumulative orientations, it is clear that the standard method to determine persistence length can be biased by chirality (*i.e.* intrinsic curvature). To exclude this influence of bond-chirality, which in turn implies a non-zero average local intrinsic curvature, and to obtain the true persistence length, here, we introduce a more general orientational correlation function <cos($\theta(N)$–<$\theta(N)$>)> (**Fig. 3.5E**). This chiral-corrected orientational correlation function decays exponentially at first few N (N_p = 29.1) and then exhibits a deviation from exponential similar to the other achiral designs at medium and larger N. (**Fig. 3.6C**). Thus, this <θ>-corrected orientational correlation function provides accurate persistence lengths for all designs, both chiral and achiral. This <θ>-corrected form is versatile since it can be used to for analyze semi-flexible chains without regard to underlying bond-chirality and intrinsic curvature.

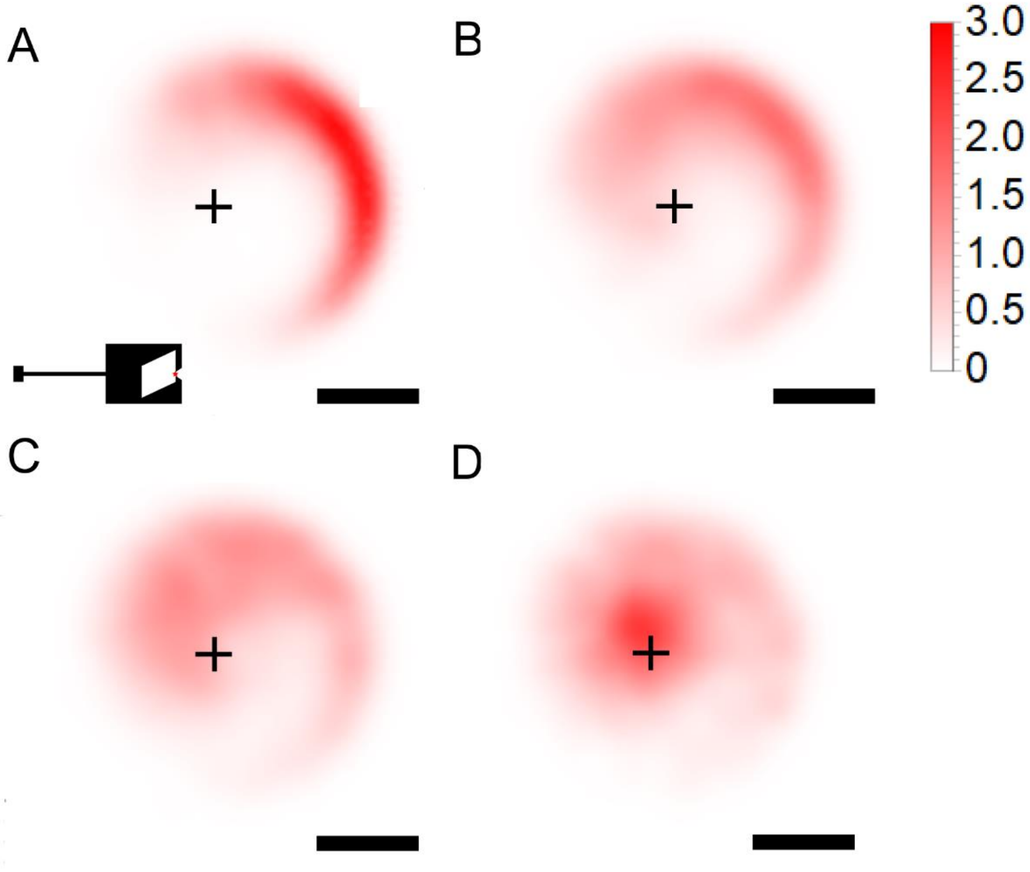

Figure 3. 8. The 2D probability density function (PDF) of end positions for several different N of chiral NC/ normalized by $x' = x/\langle l\rangle$ and $y' = y/\langle l\rangle$, fixing the position and orientation of the first monomer at (0,0), which is labeled by '+' sign in each plot. (A) $N = 25$, (B) $N = 50$, (C) $N = 75$, (D) $N = 100$. Inset in A: lower-left, design of NC/ that shows the initial orientation (pointing to right). Position (0,0) is labeled on the opening of the tail (red dot); lower right: scale bar of 15$\langle l\rangle$. Inset in B: scale bar of 30$\langle l\rangle$. Inset in C: scale bar of 45$\langle l\rangle$. Inset in D: scale bar of 60$\langle l\rangle$. $\langle l\rangle$=35.2 is the mean separation for this particular design.

We demonstrate that designed chirality in bonds also impacts the extensibility of the entire chain, on average, by calculating the root-mean-square end-to-end distance $\langle R^2\rangle^{1/2}$ and radius of gyration $\langle R_g^2\rangle^{1/2}$ (**Fig. 3.5F**). Achiral chains have $\langle R^2\rangle^{1/2}$ and $\langle R_g^2\rangle^{1/2}$ that are very close to the predictions by WLC theories (25) using their fitted persistence lengths (**Fig. 3.7**). Calculated $\langle R^2\rangle^{1/2}$ and $\langle R_g^2\rangle^{1/2}$ of achiral chains match simulated values by errors of less than 3% (**Figs. 3.7A** and **3.7B**). This calculation, however, does not apply to chiral chains (NC\ and

NC/). Because of more frequent coil-like conformations from non-zero accumulated orientations, these chiral chains have shorter $<R^2>^{1/2}$ and $<R_g^2>^{1/2}$. Notably, $<R^2>^{1/2}$, which is more sensitive to coiling, is reduced more than $<R_g^2>^{1/2}$. There is a linear relationship (dashed lines) between $<R^2>^{1/2}$ and $<R_g^2>^{1/2}$ for six achiral chains having the same number of monomers; whereas, chiral chains deviate from these linear trends, exhibiting smaller $<R^2>^{1/2}$ and $<R_g^2>^{1/2}$ as a consequence of a higher frequency of encountering coil-like conformations.

For chiral NC/, we also plot the PDF of terminal-end positions of monomers relative to a fixed starting end having the same pointing direction for the entire ensemble, yielding swirl-like patterns (**Figs. 3.8A-D**). We show the ensemble-averaged normalized end-to-end vector probability density $P_N(x', y')$ of equilibrium conformations of chiral NC/ for several different N by fixing the position and orientation of the first monomer (**Fig. 3.8**). As N increases, the most probable relative location of the monomer that is N units away from the first monomer (regions of darker red) continuously shifts leading to a spiral-like appearance; the overall distribution becomes broader, too. A second peak near the center appears when $N = 100$ and converges with the entropic peak (26); so, a brighter red spot appears near the origin.

3.3.5 Bond extensibility

While the orientational correlation functions $<\cos(\theta(N))>$ of all designs clearly reflects their corresponding limited ranges of accessible bond angles, the quasi-1D contour spatial pair correlational function $g(x)$, where x is the contour length along the chain, provides a measure of longitudinal extensibility. The decay of $g(x)$ depends on PDF of separations (**Figs. 3.4C** and

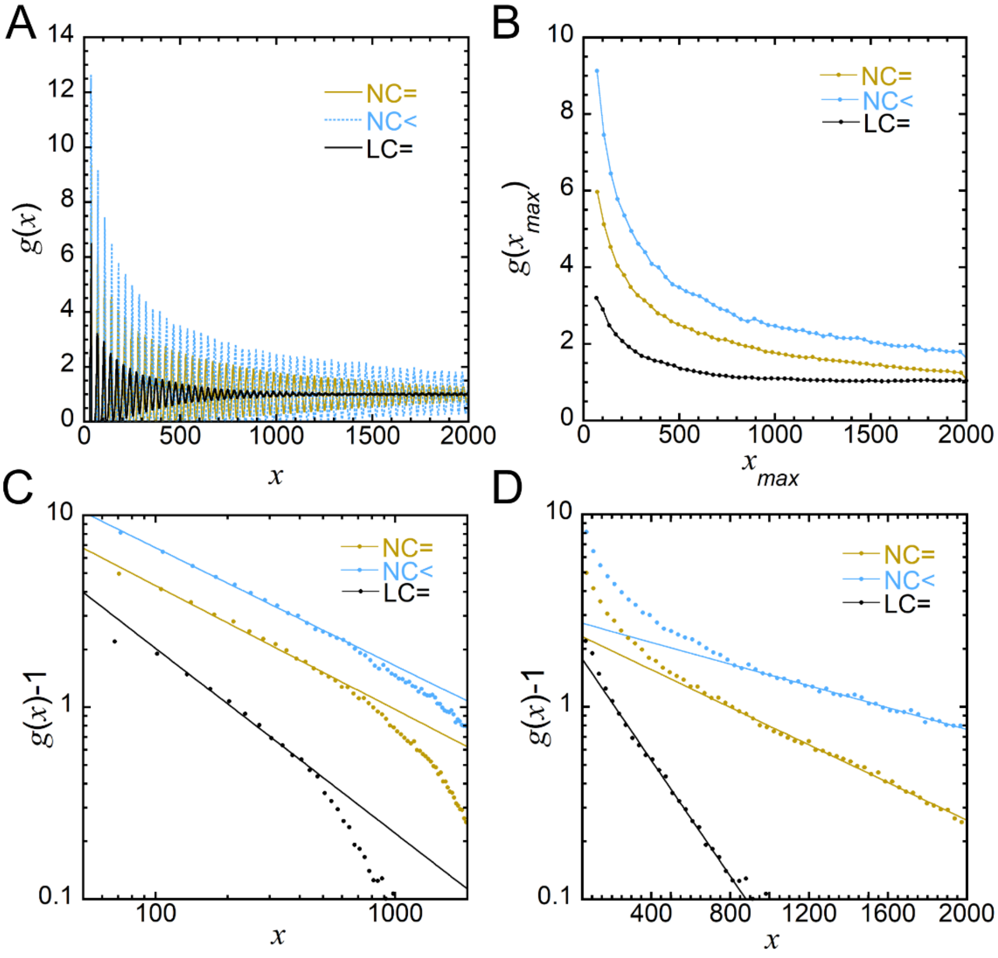

Figure 3. 9. Bond extensibilities. (A) 1D pair correlation functions along the chain. LC= decays most rapidly while NC< decays least rapidly, reflecting the distribution of lengths in Fig. 3B. (B) Peaks of local maxima from part A (lines guide the eyes). (C) A power-law decay $g(x)$-1 = ax^{-b} for small x eventually turns into (D) an exponential decay $g(x)$-1 = $A\exp(-Bx)$ at larger x. Decay constants from fits over corresponding ranges of x: $b_{\mathrm{NC=}} = 0.646$, $b_{\mathrm{NC<}} = 0.614$, $b_{\mathrm{LC=}} = 0.964$; $B_{\mathrm{NC=}} = 0.00113$, $B_{\mathrm{NC<}} = 0.000652$, $B_{\mathrm{LC=}} = 0.0346$. $R^2 > 0.990$.

3.4D): among NC=, NC< and LC=; $g(x)$ of LC= clearly decays most rapidly since LC= has the broadest PDF. By contrast, $g(x)$ of NC< decays most slowly, since NC< has the narrowest PDF (**Figs. 3.9A** and **3.9B**). Furthermore, the decay of $g(x) - 1$ follows the 1D and quasi-1D rule (27, 28) that its envelope first undergoes a power-law decay and later transforms to an exponential decay (**Figs. 3.9C** and **3.9D**). To quantify the bond extensibility, we have developed a model for $g(x)$ of a polymer chain having extensible bonds using the following interaction potential:

$\psi(l) = U_l(l)$ for $l_{\min} < l < l_{\max}$ and $+\infty$ for l outside this range. Following the procedures in Ref. (29), the pair correlation function is a damped sinusoid function with exponentially decaying envelopes at larger distance (see **Figs. 3.9A**, **3.9B**, and **3.9D**). This explains the exponential decay at large x in $g(x)$ (see line in **Fig. 3.9D**).

3.4 Discussion and Conclusion

Our MC simulations of steric lock-and-key chains provide new insight into a broader range of polymer behavior than has been previously explored through experiments on polylithomers. By designing a variety of monomer-shapes and generating equilibrium conformations, we have been able to explore unconventional polymers that have unusual properties, in particular as a consequence of bond extensibility and chirality, which otherwise would be difficult to achieve through molecular synthesis. We demonstrate that equilibrium chain properties are highly dependent on the design of monomers in a predictable and controllable way. These methods and findings not only enrich polymer models and theories, but also pave the way for quantitative analysis of molecular and colloidal complexes which have properties that are dominated by geometries of the fundamental building blocks.

In particular, we have demonstrated that bifurcated bonds lead to enhanced fluctuations in local curvature, which can also be quantified by faster growth of the orientational standard deviation σ_θ. We also have shown that chirality, arising from steric limitations of certain bond designs, has a profound impact, yielding swirling of conformations as well as unusual polymeric properties, such as a region over which the orientational correlation function is negative. Furthermore, we have improved over the standard analysis for determining persistence length by subtracting the average accumulated angle, which matters for chiral designs. In addition, increasing bond extensibility causes the contour-dependent pair correlation function $g(x)$ to decay more rapidly, giving rise to exponentially decaying envelopes at large x (**Fig.3.9D**) (29).

In addition to polylithomers, colloidal chains can also be fabricated by other methods, such as through depletion attractions and soft interactions between building blocks. Colloidal lock-and-key shaped polymers from bottom-up methods have been synthesized and assembled by depletion (30, 31) and studied by simulation (32, 33), however chains based on these approaches do not achieve the steric interlocking that is present in the pre-assembled interlocking chains made using top-down litho-PAMs, as we have investigated here. Other than lock-and-key structures, extensible bonds in colloidal polymers have been produced by photoactive macromolecular tethers between gold nanorods (34). The extensibility of those linkages results from the folding, cross-linking, or coiling of macromolecular tethers. We anticipate that MC simulations similar to the ones we have performed here could be applied to these systems in future work.

The general inverse problem of taking an ensemble of equilibrium conformations and deducing a corresponding monomer shape is an ill-posed problem; yet, the PDFs calculated from this ensemble will limit the allowed range of sub-particle features. It is possible that an iterative method could be developed to refine shapes of the monomers by imposing a constraint and fitting the PDFs while adjusting the geometry. This approach could be helpful in optimizing the bond-design of monomers to yield certain desired equilibrium conformations and vice-versa. More complex structures can be designed by lifting the constraint on the dimension of the opening size in the tail, thereby increasing the degrees of freedom to three: two positional variables and one orientational variable. Alternatively, it would also be possible to modify the shapes and sizes of the head and neck, as well as valencies of monomers (*e.g.* two or more heads and necks, two or more tails and cavities), resulting in even more complicated conformations and properties.

Our platform of analyzing polylithomers of mechanical lock-and-key linkages, or MICs, provides a simple and visualized model to understand the properties of MIMs related to geometries. While different in several ways, 2D polylithomers, based on steric colloidal bonds, share some similar aspects with 3D interlocking catenanes (14), which also have rotational and sliding degrees of freedom. For example, bifurcated NCS2 can be viewed as a station of molecular switches or molecular shuttles (35), and a super-molecular chain with multiple MIM nodes ('stations') could be represented by copolymers consisting of NCS2 and normal types. We can alter the states at each bifurcated node either by customizing the designed shapes or changing the external stimuli. Different equilibrium on-and-off (up-and-down) distributions under different local circumstances on each node, which can be modeled by different accessible states, can affect the chain conformations and properties. In the future, extending our 2D investigation into 3D will yield additional levels of complexity, which could be investigated both through simulations and experiments.

Our studies of 1D linear homopolymer chains, covering a wide variety of monomer shapes, could also be readily generalized in the future to 2D mesh (4) or 3D network structures. Although exact 2D theories have not been developed completely (36-39), molecular dynamics and MC simulations are useful tools in studying 2D and 3D fluids such as phase transitions (40, 41). In 2D, it is still an open question as to whether or not this bounded extensional potential preserves long-range order; however, for harmonic and other unbounded potentials long-range order is destroyed by long-wavelength Mermin-Wagner fluctuations. Thus, theoretically studying bounded potentials in the context of Kosterlitz-Thouless phenomena (42) is also an intriguing possibility.

References

1. A. Hirao *et al.*, Precise syntheses of chain-multi-functionalized polymers, star-branched polymers, star-linear block polymers, densely branched polymers, and dendritic branched polymers based on iterative approach using functionalized 1,1-diphenylethylene derivatives. *Prog. Polym. Sci.* **30**, 111-182 (2005).
2. C. A. Mirkin, R. L. Letsinger, R. C. Mucic, J. J. Storhoff, A DNA-based method for rationally assembling nanoparticles into macroscopic materials. *Nature* **382**, 607-609 (1996).
3. K. Zhao, T. G. Mason, Directing colloidal self-assembly through roughness-controlled depletion attractions. *Phys. Rev. Lett.* **99**, 268301 (2007).
4. T. Yu, T. G. Mason, Brownian lithographic polymers of steric lock-and-key colloidal linkages. *Sci. Adv.* **7**, eabg3678 (2021).
5. H.-P. Hsu, W. Paul, K. Binder, Polymer chain stiffness vs. Excluded volume: A Monte Carlo study of the crossover towards the worm-like chain model. *Europhys. Lett.* **92**, 28003 (2010).
6. J. Z. Zhang *et al.*, The persistence length of semiflexible polymers in lattice Monte Carlo simulations. *Polymers* **11**, 295-306 (2019).
7. A. Morriss-Andrews, J. Rottler, S. S. Plotkin, A systematically coarse-grained model for DNA and its predictions for persistence length, stacking, twist, and chirality. *J. Chem. Phys.* **132**, 035105 (2010).
8. S. Ouhajji *et al.*, Wet-chemical synthesis of chiral colloids. *ACS Nano* **12**, 12089-12095 (2018).

9. T. Hugel *et al.*, Elasticity of single polyelectrolyte chains and their desorption from solid supports studied by afm based single molecule force spectroscopy. *Macromolecules* **34**, 1039-1047 (2001).

10. X. Liu, G. H. Pollack, Mechanics of F-actin characterized with microfabricated cantilevers. *Biophys. J.* **83**, 2705-2715 (2002).

11. F. Manca *et al.*, Elasticity of flexible and semiflexible polymers with extensible bonds in the Gibbs and Helmholtz ensembles. *J. Chem. Phys.* **136**, 154906 (2012).

12. Q. Wu *et al.*, Poly[n]catenanes: Synthesis of molecular interlocked chains. *Science* **358**, 1434-1439 (2017).

13. T. Ma *et al.*, Catenated covalent organic frameworks constructed from polyhedra. *Nat. Synth.* **2** (2023).

14. P. R. Ashton *et al.*, The self-assembly of a highly ordered [2]catenane. *J. Chem. Soc., Chem. Commun.*, 634-639 (1991).

15. J. F. Stoddart, Mechanically interlocked molecules (MIMs)—molecular shuttles, switches, and machines (Nobel Lecture). *Angew. Chem. Int. Ed.* **56**, 11094-11125 (2017).

16. P. E. Rouse, A theory of the linear viscoelastic properties of dilute solutions of coiling polymers. *J. Chem. Phys.* **21**, 1272-1280 (1953).

17. X. Cai, H. Liu, G. Zhang, Control of the threading ratio of rings in a polypseudorotaxane: A computer simulation study. *Polymer* **268**, 125705 (2023).

18. X.-Z. Cao, H. Merlitz, C.-X. Wu, Mechanical strength management of polymer composites through tuning transient networks. *J. Phys. Chem. Lett.* **11**, 710-715 (2020).

19. P. M. Rauscher, S. J. Rowan, J. J. de Pablo, Topological effects in isolated poly[n]catenanes: Molecular dynamics simulations and rouse mode analysis. *ACS Macro Lett.* **7**, 938-943 (2018).

20. B. Cichocki, K. Hinsen, Dynamic computer simulation of concentrated hard sphere suspensions: I. Simulation technique and mean square displacement data. *Phys. A: Stat. Mech. Appl.* **166**, 473-491 (1990).

21. W. Schaertl, Brownian dynamics of colloidal hard spheres. 3. Extended investigations at the phase transition regime. *J. Stat. Phys.* **79**, 299-312 (1995).

22. P. Strating, Brownian dynamics simulation of a hard-sphere suspension. *Phys. Rev. E* **59**, 2175-2187 (1999).

23. A. D. Sokal, Monte Carlo methods for the self-avoiding walk. *Nucl. Phys. B - Proc.s Suppl.* **47**, 172-179 (1996).

24. D. Shirvanyants, S. Panyukov, Q. Liao, M. Rubinstein, Long-range correlations in a polymer chain due to its connectivity. *Macromolecules* **41**, 1475-1485 (2008).

25. H. Benoit, P. Doty, Light scattering from non-gaussian chains. *J. Phys. Chem.* **57**, 958-963 (1953).

26. A. J. Spakowitz, Z.-G. Wang, End-to-end distance vector distribution with fixed end orientations for the wormlike chain model. *Phys. Rev. E* **72**, 041802 (2005).

27. Y. Hu, P. Charbonneau, Comment on ``kosterlitz-thouless-type caging-uncaging transition in a quasi-one-dimensional hard disk system". *Phys. Rev. Res.* **3**, 038001 (2021).

28. A. Huerta, T. Bryk, V. M. Pergamenshchik, A. Trokhymchuk, Kosterlitz-Thouless-type

caging-uncaging transition in a quasi-one-dimensional hard disk system. *Phys. Rev. Res.* **2**, 033351 (2020).

29. M. E. Fisher, B. Widom, Decay of correlations in linear systems. *J. Chem. Phys.* **50**, 3756-3772 (1969).

30. Y. Wang *et al.*, Three-dimensional lock and key colloids. *J. Am. Chem. Soc.* **136**, 6866-6869 (2014).

31. S. Sacanna, W. T. M. Irvine, P. M. Chaikin, D. J. Pine, Lock and key colloids. *Nature* **464**, 575-578 (2010).

32. D. J. Ashton, R. L. Jack, N. B. Wilding, Self-assembly of colloidal polymers via depletion-mediated lock and key binding. *Soft Matter* **9**, 9661-9666 (2013).

33. H.-Y. Chang *et al.*, Assembly of lock-and-key colloids mediated by polymeric depletant. *Langmuir* **31**, 13085-13093 (2015).

34. A. Lukach, K. Liu, H. Therien-Aubin, E. Kumacheva, Controlling the degree of polymerization, bond lengths, and bond angles of plasmonic polymers. *J. Am. Chem. Soc.* **134**, 18853-18859 (2012).

35. A. M. Brouwer *et al.*, Photoinduction of fast, reversible translational motion in a hydrogen-bonded molecular shuttle. *Science* **291**, 2124-2128 (2001).

36. J. A. Barker, Statistical mechanics of almost one-dimensional systems. *Aust. J. Phys.* **15**, 127-134 (1962).

37. D. A. Kofke, A. J. Post, Hard particles in narrow pores. Transfer-matrix solution and the periodic narrow box. *J. Chem. Phys.* **98**, 4853-4861 (1993).

38. I. E. Kamenetskiy, K. K. Mon, J. K. Percus, Equation of state for hard-sphere fluid in

restricted geometry. *J. Chem. Phys.* **121**, 7355-7361 (2004).

39. V. M. Pergamenshchik, Analytical canonical partition function of a quasi-one-dimensional system of hard disks. *J. Chem. Phys.* **153**, 144111 (2020).

40. A. Huerta, D. Henderson, A. Trokhymchuk, Freezing of two-dimensional hard disks. *Phys. Rev. E* **74**, 061106 (2006).

41. C. L. Hicks, M. J. Wheatley, M. J. Godfrey, M. A. Moore, Gardner transition in physical dimensions. *Phys. Rev. Lett.* **120**, 225501 (2018).

42. J. M. Kosterlitz, D. J. Thouless, Ordering, metastability and phase transitions in two-dimensional systems. *J. Phys. C: Solid State Phys.* **6**, 1181 (1973).

Chapter 4 – Heptatic Liquid Seven-Fold Quasi-Crystals by Lithographic Colloidal Pre-Assembly

4.1 Introduction

A rich variety of phases exist in two-dimensional (2D) Brownian systems, composed of differently shaped building blocks, as a function of particle area fraction ϕ. Kosterlitz-Thouless-Halperin-Nelson-Young (KTHNY) theory has established that a 2D system of uniform disks experiences a continuous melting transition from a solid hexagonal crystal to a disordered isotropic fluid mediated by a hexatic phase (1-3). This hexatic phase exhibits long-range bond orientational order, yet only short-range positional order, and was first identified experimentally in a 2D monolayer of spheres (4). In addition to isotropic disks, Onsager first predicted the dependence of liquid crystalline (LC) order on molecular geometry (5) and showed that other LC phases, which reflect the symmetry and shape of constituent particles, could exist. Through 2D simulations of hard-interacting squares, Wojciechowski and Frenkel identified a tetratic phase (6). Subsequently, through 2D experiments on slowly crowded lithographic prismatic tiles, Zhao and Mason observed a triatic phase of regular triangles having nearly hard interactions (7). Surprisingly, similar experiments on slowly crowded lithographic squares having a minor degree of corner rounding did not reveal a tetratic phase but rather a rhombic (RB) phase with rhombic symmetry (8). As suggested by Zhao and Mason, corner-rounding turned out to be the reason that the tetratic phase was not observed in the experiments, as F. A. Escobedo and co-workers demonstrated through systematic simulations of corner-rounded squares (9). Later, simulations confirmed the triatic phase associated with triangles (10). Also, simulations demonstrated a hexatic phase of perfect regular hexagons (11); however, experiments on lithographic regular hexagon tiles did not reveal a hexatic phase (11) All of these findings provide evidence for and beyond KTHNY scenarios (12-14). Thus, 3-fold, 4-fold, and 6-fold regular polygons can form crystal phases in their respective close packing limits as ϕ approaches unity, and, in principle, corresponding '*x*-atic' LC phases exist. Assemblies of more complex shapes, such as Penrose kites, exhibit glassy states as a consequence of diversity and incommensurability of local polymorphic configurations (LPCs) (15, 16) or tetratic rectangular phases (17) towards high densities. No pentatic phase was observed in experiments (18) and simulations (19) of slowly crowded regular pentagons as a consequence of imperfect spatial tiling arising from the 5-fold forbidden symmetry.

However, quasi-crystals (QCs) can provide a way of creating systems having such forbidden symmetries. QCs have long-range positional order but no translational periodicity and were first discovered in metal alloys having novel 5-fold symmetry in 1980s (20). Since then, self-assembled QCs of 10-, 12-, and 18-fold symmetries have been observed for several different shapes and interactions of constituent building blocks, such as molecules (21), micelles (22-25), polyphilic polymers (26-28), metal nanoparticles (29), and quantum dots (30) at molecular and colloidal length scales. However, these bottom-up self-assembly methods are typically limited by slow formation rates, small crystalline regions, and defects. Moreover, these self-assembled QCs usually do not follow strict inflation rules as a consequence of entropy. In order to overcome these limitations, a top-down method, known as lithographically pre-assembled monolayers (litho-PAMs) (31), has been developed. As a first example, a perfect 5-fold Penrose 2D QC of colloidal prismatic tiles of kites and darts has been fabricated and subsequently released into a liquid dispersion; these tiles are subject to Brownian fluctuations and have nearly hard in-plane interactions. Motions of many tile-particles can be readily visualized using optical microscopy and thereby analyzed by digital particle tracking in a large area over a long time period. A fluctuating pentatic liquid quasi-crystal (LQC) phase, reflecting the initial 5-fold QC symmetry, was observed at high ϕ. This litho-PAMs approach thus provides a potential route for investigating colloidal Brownian systems that have forbidden symmetries beyond 5-fold.

Fluctuating LQCs composed of mobile tiles not only possess unconventional symmetries, but also show heterogeneity of order and dynamics for different constituent particles and motifs at different length scales. Heterogeneity in structures and dynamics has been identified in super-cooled glass-forming liquids due to spatial differentiation of ordered and disordered regions and collective motions via cage rearrangement (32-36). In addition, heterogeneity is also observed in multi-component systems, such as the binary liquid crystal made from long and short rods because of different effective mean-field potentials determined by geometries and LPCs as a result of ineffectiveness towards dense packing (37). Furthermore, heterogeneities can also arise from hierarchical structures. In QC patterns, various motifs may behave very differently from constituent individual tiles. As a result, these features would further contribute to the breaking of perfect 2D order in addition to Mermin-Wagner fluctuations (38).

Here, in order to demonstrate and study a heptatic LQC phase, we extend litho-PAMs to fabricate and release 7-fold QCs consisting of three different types colloidal rhombic tiles; moreover, we show that this heptatic LQC is a good model for studying such heterogeneities of various origins, which can be identified by tracked trajectories and Fourier transforms. Although Voronoi analysis (39) has been applied to non-trivial, relatively compact shapes such as Penrose kites (15), we show that Voronoi analysis is problematic for this 7-fold QC and for a wide range of other non-compact shapes, because portions of constituent tiles may lie outside their respective Voronoi cells. To overcome this limitation, we develop a new edge-proximity tessellation method based on equal distances between edges of tiles, rather centroids of tiles, to analyze local structure and to determine nearest neighboring tiles. Edge-proximity tessellation can be readily generalized to a wide variety of systems containing many different non-compact shapes. These findings provide additional insight into how shapes of mobile interacting building blocks influence the properties of pre-assembled colloidal hierarchical assemblies having unusual symmetries.

4.2 Materials and Methods

4.2.1 Generating seven-fold QC pattern digitally

An ideal seven-fold quasi-crystal pattern is built from three types of rhombi having different interior angles: type-1 ($3/7\pi$, $4/7\pi$), type-2 ($2/7\pi$, $5/7\pi$), and type-3 ($1/7\pi$, $6/7\pi$) (40). Edges of about $5*10^5$ tiles are digitally generated as thin line segments in lithographic layout software (L-edit, Tanner Research, **Fig. 4.1A**) by two-dimensional projection of a planar slice through a seven-dimensional hyper-lattice (41). The thickness of these lines (red) is customized so that the tile region (white) outside these lines would have the desired area fraction. The designed edge lengths in L-Edit are $D_1 = 46$ μm, $D_2 = 45$ μm, and $D_3 = 40$ μm. Rigid confining walls (thickness of 500 μm), which are fused together with the outermost tiles, are designed to maintain a fixed area fraction after release.

4.2.2 Fabrication by optical lithography

We have used our previously established protocol for fabricating polylithomers (42), modified as described below (see **Chapter 2.2** for more details). Before pre-baking, we clean the glass wafer with Piranha solution (3:1 mixture of sulfuric acid and 30% hydrogen peroxide). To create different area fractions from the same designed pattern, we use different energy dose (140 mJ /cm^2 for the ϕ_{low} and 160 mJ/cm^2 for ϕ_{high}) when exposed in the stepper (PAS 5500/200, ASML, 5X reduction, UV i-line 365 nm). After photoresist development, we subsequently use different descumming procedures (Matrix 105 Asher, Matrix Inc. 4:6 Oxygen/Nitrogen flow, RF power = 100 W, chamber temperature = 50 °C; descumming time = 180 s for ϕ_{low} and 30 s

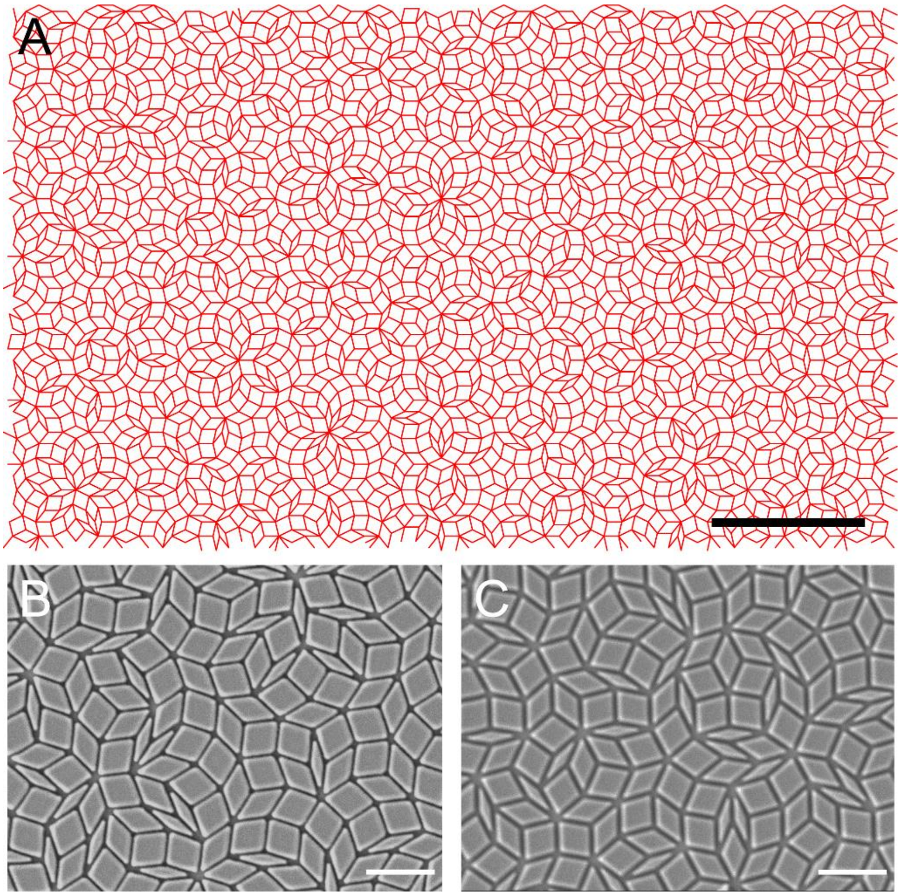

Figure 4. 1. Design and printing of a 7-fold QC. (A) Designed mask pattern using line segments having controlled thickness in L-edit. The area fraction of tiles (white) depends on the thickness of these line segments. Scale bar: 500 μm. These patterns are lithographically produced at 5x reduction using an optical stepper, followed by oxygen plasma descumming (see text), which further modifies ϕ. (B) SEM image of the higher ϕ pattern with $\phi_{\text{high}} = 0.792$. (C) SEM image of the lower ϕ pattern with $\phi_{\text{low}} = 0.663$. Scale bar: 20 μm.

for ϕ_{high}, respectively.) to make sure that all tiles are disconnected and also to modify the printed tile area fraction.

4.2.3 Release and imaging of seven-fold QC

The actual scale and area fraction of printed pattern is determined from SEM images (JEOL, JSM-6700F FE-SEM). Conductivity of the sample is enhanced by deposition of a thin gold film by sputtering (HUMMER 6.2 Sputtering system, Anatech LTD.) before taking SEM. To calculate the area fraction, the interior regions of all tiles in SEM images are identified and colored using *Magic Wand* in Photoshop. Total number of colored pixels inside the tiles are counted in Mathematica using *ComponentMeasurements*, and the area fraction is calculated by to ratio of the number of pixels inside the tiles divided by the total number of pixels inside the field of view. The printed edge lengths of each tile after five-times-reduction stepper on the wafer are estimated to be D_1 = 9.1 μm, D_2 = 8.8 μm, and D_3 = 7.2 μm for ϕ_{high} (**Fig. 4.1B**), and D_1 = 8.6 μm, D_2 = 8.0 μm, and D_3 = 6.7 μm for ϕ_{low} (**Fig. 4.1C**).

We use similar release protocols as reported previously (31), modified as described below. A small acrylic wall is implemented to help keep the pre-configured area fraction. This acrylic wall is made using a laser cutter (K40 laser cutter, OMTech) and has a suitable size to cover the boundary of the printed pattern. Next, we apply superglue (Epoxy power ultra-strong, Araldite) onto the bottom side of the acrylic wall, attach the wall onto the QC boundary and wait for 12 hours. Then we follow the previous protocol with slightly modified release solution–dispersion (RSD) consisting of 0.5% tetramethylammonium hydroxide (TMAH), 1% 30 nm dia. polystyrene spheres (Latex microsphere suspensions 5003A, Thermo Scientific), and 20 mM sodium dodecyl sulfate (SDS) surfactant. We then use an inverted optical microscope (Nikon TE2000, 10x CFI plan achromat objectives) to take brightfield transmission high-resolution images (Nikon Z7 camera) every 60 seconds, yielding time-lapse movies of fluctuating tiles having a 7-fold QC as an initial condition before release.

4.2.4 Image analysis and particle tracking

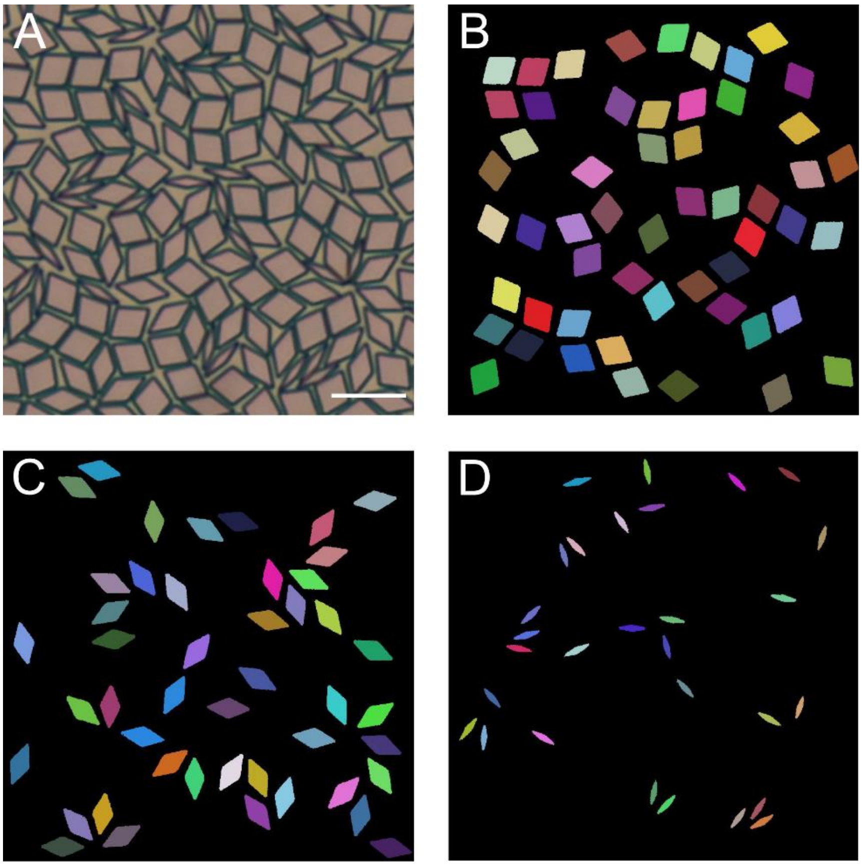

Figure 4. 2. Particle tracking based on tile-shapes. (A) Brightfield micrograph. (B) Type-1, (C) type-2, and (D) type-3 rhombi are recognized by distinct geometrical properties. For one particle in a certain frame, a particle in its subsequent frame is considered to be its successor if (1) it has the nearest distance (2) the distance does not exceed a certain range. Only the particles present in all the frames are tracked. Scale bar: 20 μm.

We have written a particle tracking routine in Mathematica (Wolfram Research, version 12.0) that tracks the centroids and orientations of different tiles from recorded time-lapse images. This routine first adjusts, binarizes, and then identifies these rhombic tiles by *MorphologicalComponents*. Different types of tiles are identified using *SelectComponents* through quantitative differences in their geometrical properties by parameters related to *FilledCount*, *Elongation*, and *Rectangularity* (**Fig. 4.2**). Centroids and orientations of tiles are then calculated using *ComponentMeasurements*. Identities of particular tiles are maintained throughout the video analysis as follows: the successor of each tile in the next frame is

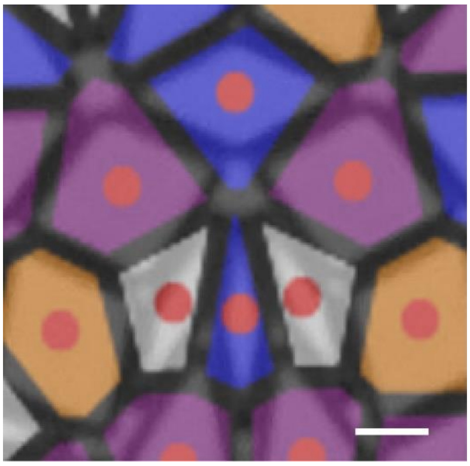

Figure 4. 3. Problems of Voronoi tessellation on non-compact shapes. Portions of some tiles lie outside the corresponding Voronoi cell. Scale bar: 5 μm.

identified by calculating the distance between this particular tile in the current frame and all local tiles up to nearest neighboring tiles in the next frame; the smallest distance corresponds to the same tile. By repeating this, a tile's trajectory is determined. To handle tiles at the boundaries, some of which can leave the field of view over long times, and also to handle tile selection issues, which sometimes occur when using *SelectComponents*, we filter incomplete tile trajectories out of the subsequent analyses.

To overcome limitations of Voronoi analysis for non-compact shapes (**Fig. 4.3**), we develop an edge-proximity tessellation method based on the shapes and edges of tiles instead of the center positions of tiles. In Mathematica, we first use the extracted center positions, orientations, and the measured interior angles and edge lengths of different tiles to digitally reconstruct the particular configuration of tiles in each optical microscopic image using more accurate SEM-parameters. Then we apply *Thinning* with *MedialAxis* to the uncovered regions to obtain the network of equal distance to the edges of neighboring tiles. Next, we convert this network into a graph that preserves the connectivity by *MorphologicalGraph*, and then we find the corresponding tessellation polygonal cell for each tile. Therefore, we can colorize these polygonal cells by their number of edges, which reflect the number of nearest edge-proximate neighbors. Very small lengths of cell edges in the morphological graphs have been excluded due to experimental uncertainties.

To calculate the motif superstructural orientational pair correlation function ($g_{\mathrm{MSO\text{-}PCF}}$), we identify and colorize the tiles forming the desired motifs (*e.g.* a heptagonal star, which may contain different constituent tiles) and superstructures (*e.g.* one heptagonal star motif surrounded by seven heptagonal star motifs) in Photoshop. Superstructural angles and the $g_{\mathrm{MSO\text{-}PCF}}$ are defined and calculated using equations in (31), modified for the 7-fold symmetry here.

4.3 Results

4.3.1 Release and kinetics of seven-fold QC

Pre-assembled patterns of seven-fold QCs are digitally designed and lithographically fabricated to have different ϕ (**Figs. 4.4A** and **4.4B**). Area fractions are determined by SEM images (**Figs. 4.1B** and **4.1C**) to be $\phi_{\mathrm{low}} = 0.663$ and $\phi_{\mathrm{high}} = 0.792$. To create monolayers that undergo 2D Brownian fluctuations at fixed tile area fraction, we enclose the printed region with acrylic and PDMS walls, and add the RSD. The RSD dissolves the Omnicoat sacrificial layer through the base TMAH, keeps the released tiles in a 2D monolayer just above the wafer by roughness-controlled depletion attractions (43), and prevents the released SU-8 tiles from aggregating or sticking to the glass substrate through surface adsorption of dodecyl sulfate (DS-) anions. Brownian fluctuations of the rhombic tiles are then recorded as time-lapse movies using

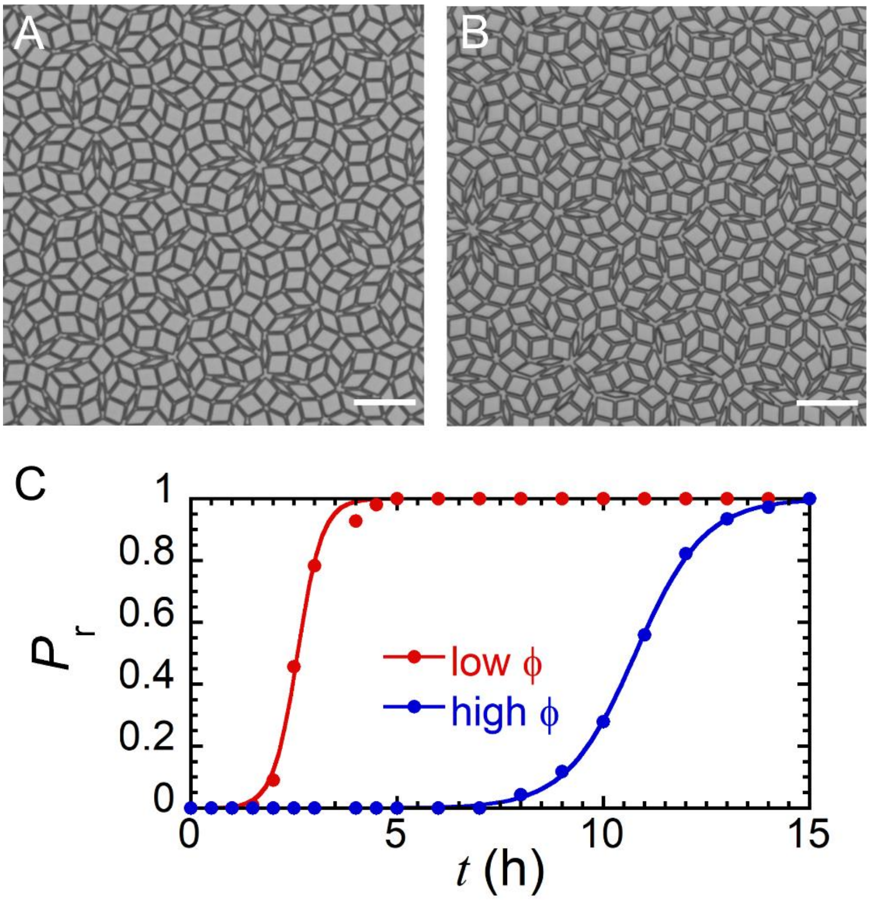

Figure 4. 4. Release and kinetics. (A) Optical micrograph before release of a higher density 7-fold QC of rhombic tiles having an area fraction $\phi_{\text{high}} = 0.792$. Scale bar: 30 μm. (B) A lower density 7-fold QC before release at $\phi_{\text{low}} = 0.663$. Scale bar: 30 μm. (C) Release fraction P_r as a function of time t for lower ϕ (red) and higher ϕ (blue) system. Tiles are excited slowly at first, then this release process accelerates later and saturates in the end. The release process of the higher ϕ pattern is slower but follows similar rules.

a high-resolution camera mounted on an inverted optical microscope (**Movies 4.1 and 4.2**). We analyze the release dynamics by calculating the fraction of tiles that have moved, $P_r(t)$, after adding the RSD at time $t = 0$. The shapes of $P_r(t)$ at different ϕ are similar; however, tiles at ϕ_{low} are released much faster than at ϕ_{high} (**Fig. 4.4C**). The release curve can be fit by a Fermi-like function: $P_r(t) = 1–1/(\exp(t/\tau–b)+1)$, where $\tau_{\text{low}} = 0.298$ h and $\tau_{\text{high}} = 0.840$ h are the characteristic time scales of release, and $b_{\text{low}} = 8.66$ and $b_{\text{high}} = 12.87$ are the characteristic release midpoints. Slower release rate of ϕ_{high} may result from fewer uncovered areas of the sacrificial layer. Therefore, the contact and permeation of RSD and the sacrificial layer is slowed down, which in turn decelerates the dissolution of Omnicoat and subsequent release of the SU-8 tiles above. This also explains the fastest release of thinnest tiles (type-3) because of their relatively smallest ratio of the sacrificial layer covered by the tile and uncovered in the neighborhood.

4.3.2 Heptatic LQC phase

Brownian fluctuations alter the degree of 7-fold quasi-crystalline order compared to the initial pre-release state. We take the Fourier transforms (FTs) of the grayscale micrographs, which mimic light-scattering patterns, to analyze the structural order before and after release at different ϕ. In the pre-released pattern (**Fig. 4.5A**), fourteen thin rays, which emanate from the center towards high scattering wavenumbers q in the FT, indicate the high degree of orientational alignment of all tiles along certain axes in the plane (**Fig. 4.5D**). Sets of discrete peaks in these rays, which have 14-fold symmetry extending to high q, are signatures of crystalline order (44). Sharp and intense Bragg-like peaks at low q (**Fig. 4.5G**) demonstrate the ordering of superstructures at larger length scales. At long times for ϕ_{high}, 72 hours after release (**Fig. 4.5B**), peaks disappear at larger and intermediate q, indicating that perfect crystalline order no longer exists. Instead, ring-like intensities with fourteen-fold modulations are observed (**Fig. 4.5E**); these modulations reflect the underlying degree of edge alignment of constituent tiles (8). Nevertheless, at the very lowest q, peaks are broadened but still observable (**Fig. 4.5H**), reflecting that superstructural order at larger scales is still evident. The FTs at ϕ_{high} obtained long after release provide evidence for a novel heptatic LQC phase. The degree of alignment of tile orientations can be quantified by the orientational standard deviations σ_θ. Tile long-axis orientations are normalized to [0, π/7]. In the pre-release pattern, σ_θ arises from

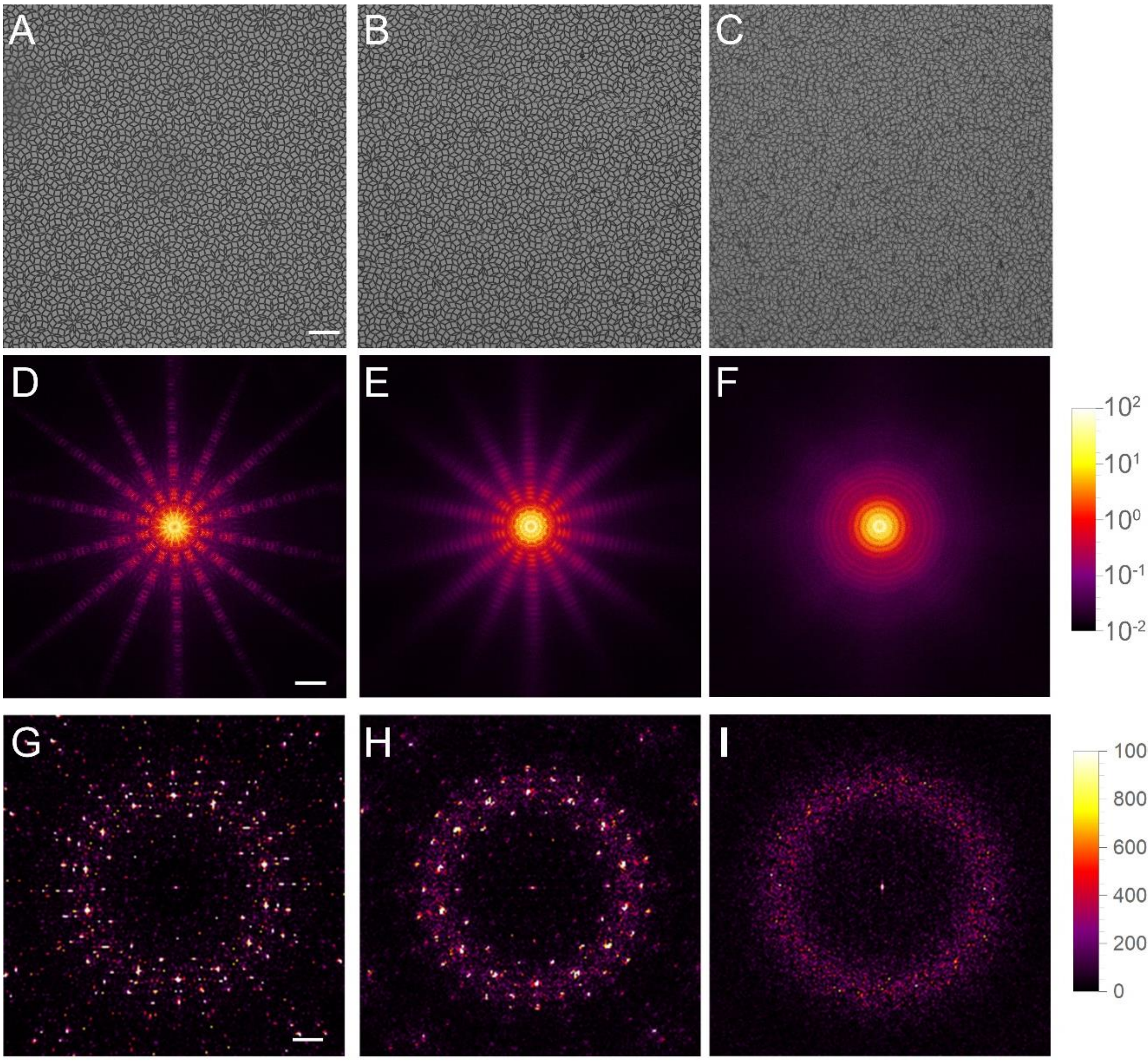

Figure 4. 5. Fourier analysis of fluctuating patterns with different area fractions. Optical micrographs of 7-fold QCs at *t* after release: (A) ϕ_{high} at $t = 0$; (B) ϕ_{high} at $t = 72$ h; and (C) ϕ_{low} at $t = 25$ h. (A)-(C) Scale bar: 50 μm. (D)-(F) Fourier analysis of (A)-(C). Scale bar: 50 μm^{-1}. Intensity color scale: see color bar to the right of (D)-(F) in arb. units. (D) Fourteen narrow rays that extend from the center towards high wavenumbers *q* indicate a high degree of orientational alignment of the edges of all tiles before release only along specific axes in the plane. (E) After 72 h release, fourteen-fold modulations in ring-like intensity patterns are still present for ϕ_{high}. (F) By contrast, for ϕ_{low} at $t = 25$ h, only isotropic rings, indicative of a completely disordered system, are observed. (G-I) Central regions of (D-E), magnified by a factor of 20, using a different signal intensity scale (see color bar to the right of (I)). Scale bar: 2.5 μm^{-1}. Strong Bragg peaks at low *q* in (G) before release show a very high degree of superstructural order at large length scales. Bragg peaks are broadened in (H), and completely disappear in (I).

uncertainties in image acquisition and analysis: $\sigma_{\theta,1} = 1.32°$ for type-1, $\sigma_{\theta,2} = 0.48°$ for type-2, and $\sigma_{\theta,3} = 0.51°$ for type-3. After release, the distributions are broadened: $\sigma_{\theta,1} = 4.46°$,$\sigma_{\theta,2} = 4.56°$, and $\sigma_{\theta,3} =4.77°$. At ϕ_{low} (**Fig. 4.5C**), only isotropic rings are seen in the FT at higher q (**Fig. 4.5F**) and Bragg peaks no longer exist at lower q (**Fig. 4.5I**), indicative of the complete disappearance of any order (*i.e.* melting) 25 hours after release.

Unlike '*x*-atic' phases present in systems of regular *x*-polygons, this heptatic LQC phase is characterized by heterogeneous hierarchical structures arising from different building blocks and motifs at different length scales. The 14-fold ring-like modulations at intermediate q and the broadened Bragg peaks at low q (**Fig. 4.5E**) are indicative of such hierarchical heterogeneities. This implies that individual tiles, motifs, and superstructures at different length scales do not have the same degree of structural order.

4.3.3 Heterogenous structure for different tiles

We take partial FTs of centroids only of each type of tile, which reveal different degrees of order for different tile-types. We extract the center positions for each tile-type through morphological particle tracking (**Fig. 4.6**). Only FTs at intermediate and lower q are shown for clarity, since FTs at higher q depend on the sizes of dots used to mark the center positions of the tiles. Strikingly, these partial FTs show different Bragg peaks and 14-fold modulations for different tile-types in the same micrograph. At ϕ_{high} after 72 hours, the partial FT of type-1 tiles exhibits 14-fold modulations at intermediate q and broadened Bragg peaks at lower q (**Fig. 4.7B**); the partial FT of type-2 tiles shows that the 14-fold modulation at intermediate q is lost, but weaker Bragg peaks at lower q are still present (**Fig. 4.7F**). By contrast, the partial FT of

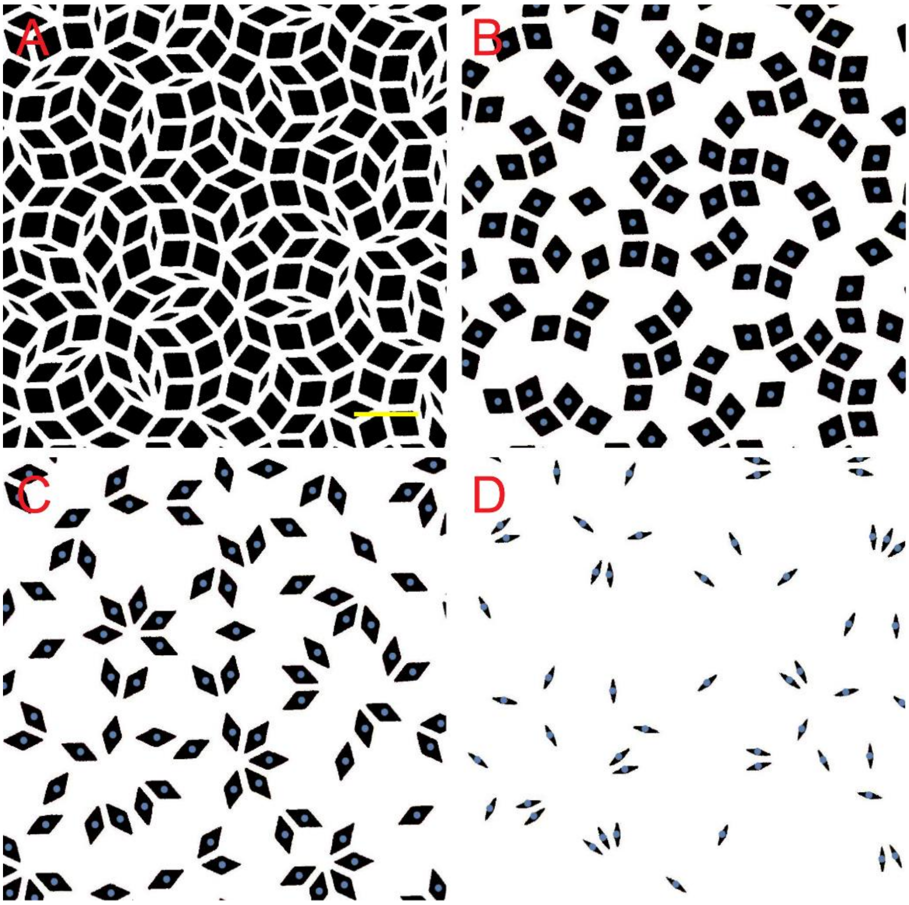

Figure 4. 6. Calculating partial FTs. (A) From the full QC, we identify different types of tiles: (B) type-1, (C) type-2, and (D) type-3. The center positions (blue dots) are calculated and labeled. We then take the FTs of center positions only. Scale bar: 20 μm.

type-3 tiles is isotropic and has no observable 14-fold modulations or Bragg peaks (**Fig. 4.7J**). At ϕ_{low} after 5 hours, the partial FT of type-1 tiles only exhibits weaker Bragg peaks at lower q (**Fig. 4.7C**); whereas, Bragg peaks in the partial FT of type-2 tiles are nearly lost (**Fig. 4.7G**). At ϕ_{low} after 25 hours, all partial FTs are isotropic (**Figs. 4.7D, H, L**).

Even in the initial 7-fold QC pattern, the presence of different tile-types creates different center-to-center tile-tile separations, r, that become convolved together in the full spatial pair correlation function (PCF), $g(r)$, that includes all tiles. This full PCF is thus difficult to interpret, other than the overall decay of positional order. Consequently, we also calculate the partial and mixed pair correlation functions, $g_{ij}(r)$, to reveal more detailed structures of

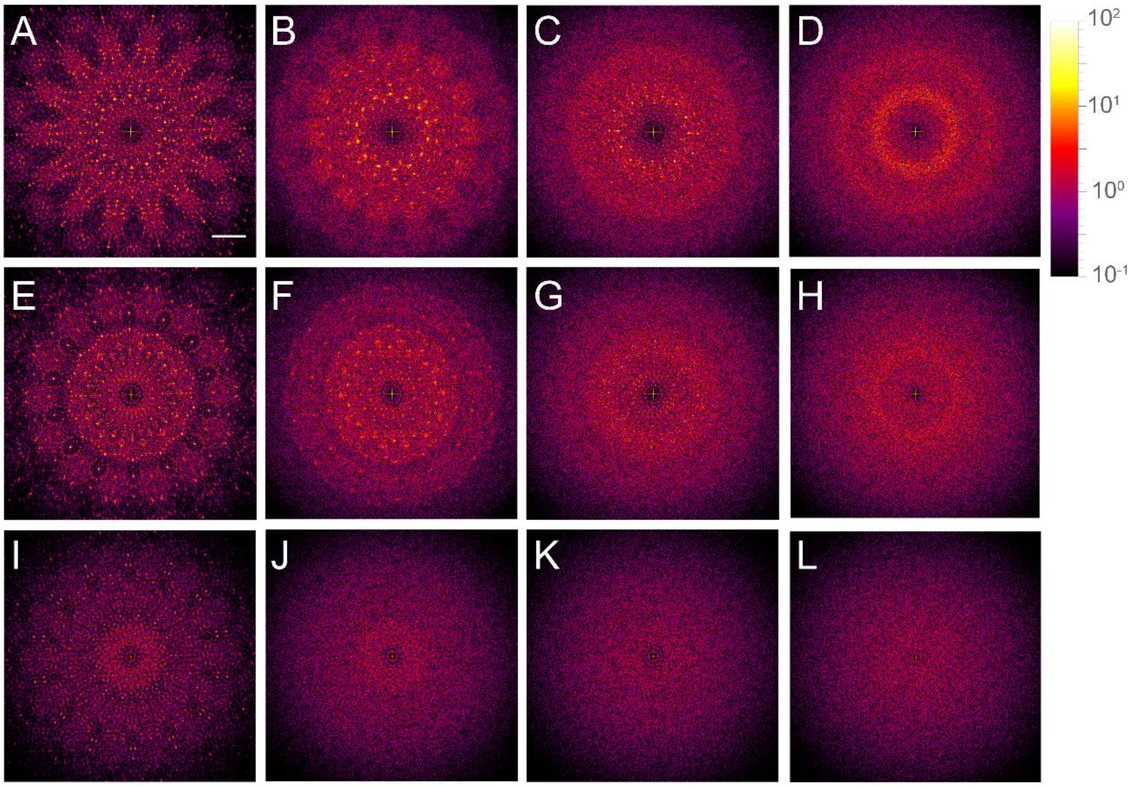

Figure 4. 7. Partial FTs at different stages reveal structural heterogeneity for different types of tiles. Intermediate and lower q values are shown for clarity. (A)-(D) Partial FTs of center positions of type-1 tiles in lithographic 7-fold QCs: (A) ϕ_{high} at $t = 0$; (B) ϕ_{high} at $t = 72$ h; (C) ϕ_{low} at $t = 5$ h; and (D) ϕ_{low} at $t = 25$ h. 14-fold modulations at intermediate q are not seen in (C) and low-q Bragg peaks have disappeared in (D). (E)-(H) Partial FTs of center positions of type-2 tiles calculated from the same micrographs as in (A)-(D). 14-fold modulations are not clearly visible in (F), and Bragg peaks have completely disappeared in (G). (I)-(L) Partial FTs of center positions of type-3 tiles calculated from the same micrographs as in (A)-(D). 14-fold modulations and Bragg peaks are only present in (I). Scale bar for all partial FTs (in (A)): 10 μm^{-1}. Intensity scale bar (to right of (D)): logarithmic from 10^{-1} to 10^2 (all partial FTs).

tile-type i with respect to tile-type j. The position of the first peak shows the relative proximity, the height shows the relative abundance, and the width shows the diversity between different local configurations of nearest neighbors. In the pre-released pattern, the first peak gradually shifts to the origin from g_{11} (**Fig. 4.8A**) to g_{22} (**Fig. 4.8B**), and to g_{33} **(Fig. 4.8C**), consistent with their relative tile sizes. The first peak of the mixed partial PCF g_{ij} when $i \neq j$, exactly lies in between the first peaks of g_{ii} and g_{ij} (**Figs. 4.8D** and **4.8E**). Type-1 tiles

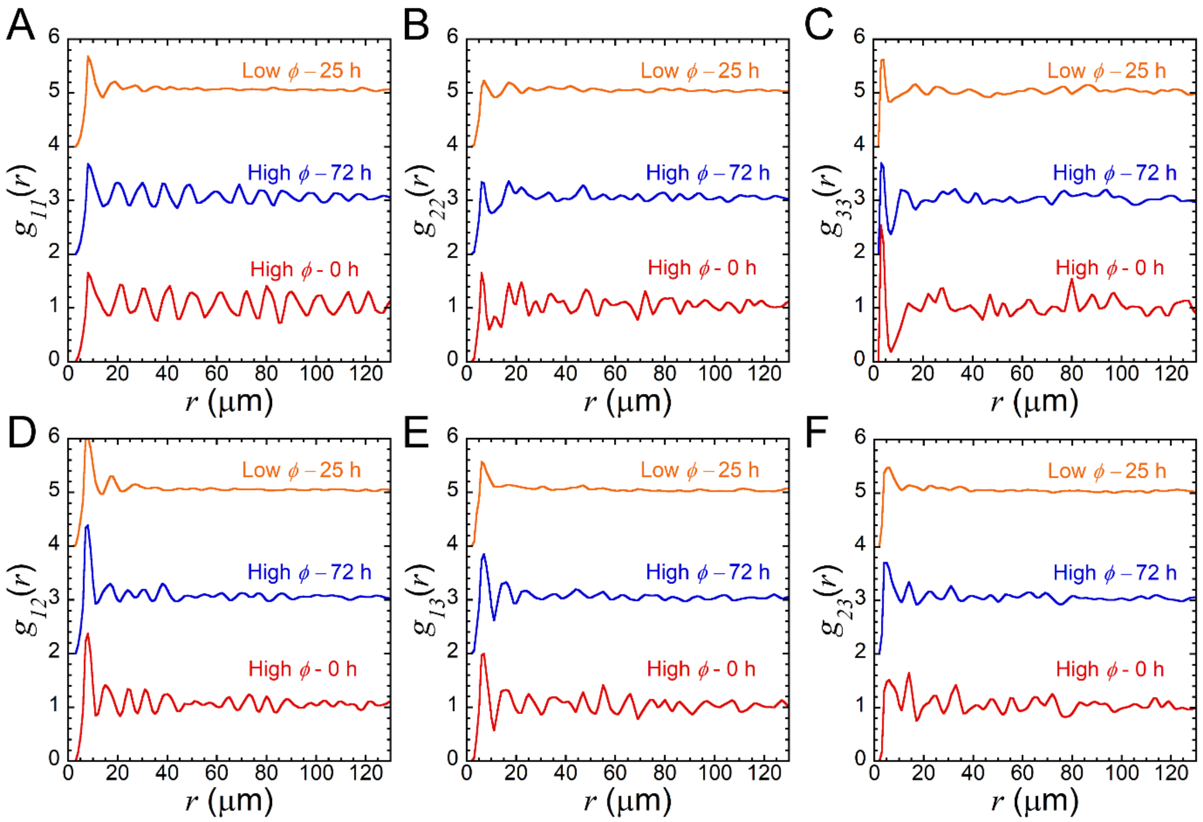

Figure 4. 8. Partial (A)-(C) and mixed partial (D)-(F) spatial pair correlation functions $g_{ij}(r)$, where i and j indicate particle types. Type-1 tiles retain the highest degree of order 72 h after release at ϕ_{high}, consistent with partial FT results. The position and height of the first peak show relative proximity and abundance between neighboring tile pairs.

preserve the most degree of order 72 hours after release at ϕ_{high} (**Fig. 4.8A**), reflecting the strongest 14-fold modulation and strongest Bragg peaks in the corresponding partial FT **(Fig. 4.7B**). The depletion zones after the first peak do not exist except in g_{33}, because there are many diverse, intermediate local tile configurations, compared with the finite sampling interval. For example, two type-1 tiles can contact each other, or can be separated by one or two type-3 tiles. The distances between two type-1 tiles in these situations are very close. However, for g_{33}, the first peak is responsible for two tiles stacked together or alternatively separated by one type-3 tile. No intermediate distances exist until two type-3 tiles are separated by one type-2 tile; this local configuration contributes to the second peak. In disordered systems, the random orientations of tiles generate many intermediate pair distances, so the depletion zone after the first peak disappears (**Fig. 4.8C**).

4.3.4 Heterogeneous shape-dependent tile and motif dynamics

Structural heterogeneity is related to dynamical heterogeneity, which can arise from different shapes of tiles. We track the trajectories of the centroids for different types of tiles at ϕ_{low} after release until 12.5 h when all evidence of crystalline structure is lost (**Movie 4.3**). The distinct degree of order of different types of tiles (**Fig. 4.7**) can be attributed to both their intrinsic Brownian dynamical property and diverse local configurations. Such diversity of local configurations of different tile-types would dominate the fluctuating dynamics of dense systems. In order to decouple these factors, two separate periods are displayed: before 5 hours when tiles begin to release (**Figs. 4.9A-C**), and from 5 to 12.5 hours when all tiles are released

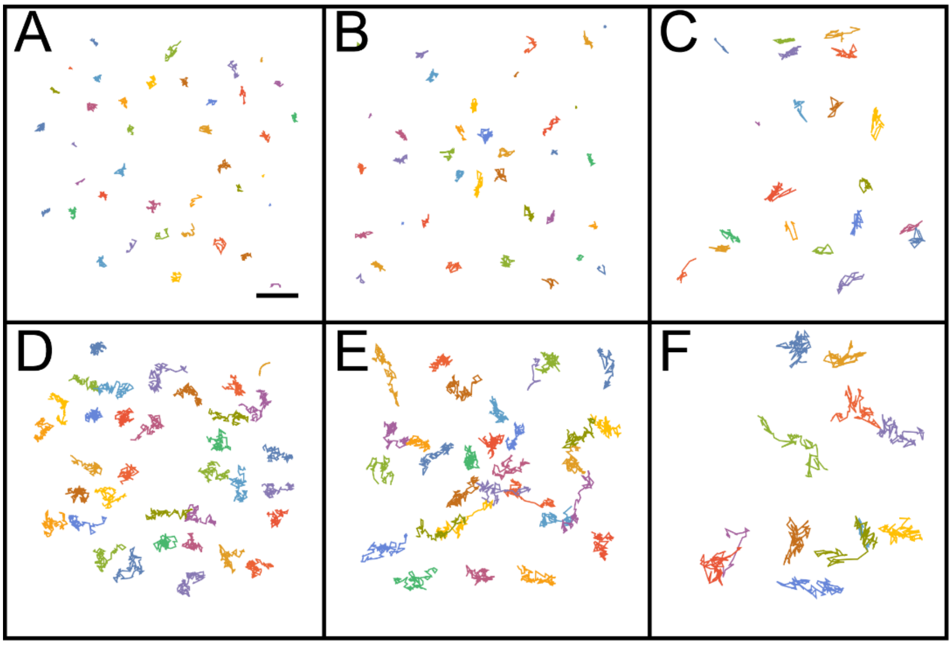

Figure 4. 9. Trajectories of different types of tiles after release. (A)-(C) Before 5 h when tiles start to be released. Type-3 tiles are released first. (D)-(E) From 5-12.5 h when all tiles are released. Type-3 tiles have longest displacement. Scale bar: 15 μm.

and undergo Brownian fluctuations (**Figs. 4.9D-E**). Some of the particles in the first period are not tracked during the second period because they may occasionally move out of the field of view. In the first period, type-3 are released faster than type-2 than type-3 tiles, and consequently have larger displacement. Therefore, at t = 5 h, type-1 tiles preserve the most degree of order (**Fig. 4.7C**). In the second period, all tiles have been released. We calculate mean-square displacement (MSD) for different tiles, $<\Delta r_1^2>^{1/2} = 7.5$ μm, $<\Delta r_2^2>^{1/2} = 9.9$ μm, and $<\Delta r_3^2>^{1/2} = 13.1$ μm to show their relative mobility. We can further calculate the free MSD in very sparse systems. By comparing free MSD with the restricted MSD in relatively dense local environment, we can study the influence of local structural heterogeneity on the dynamical heterogeneity of different tiles.

Dynamical heterogeneities can also arise from diverse motifs of tiles and superstructures of motifs at successively larger length scales, especially at ϕ_{high} where Brownian fluctuations are highly restricted. Corrugated motifs, such as the heptagonal star composed of 7 type-2 tiles, undergo bounded Brownian motions that maintain the 7-fold symmetry (**Figs. 4.10A-D, Movie 4.4**). We digitally track the fluctuations of center positions and orientations of tiles in the heptagonal star motif (**Figs. 4.10E** and **4.10F**). Translational fluctuations are bounded within ≈5 μm, and rotational fluctuations are limited within 17°. By contrast, non-corrugated motifs, such as the ellipse-like motif (**Figs. 4.11A** and **4.11B,** inside yellow-dashed line), which contains several different kinds of tiles, exhibits collective motion even at very high density without cage breaking. Such collective motif-rotation breaks the local 7-fold symmetry of a

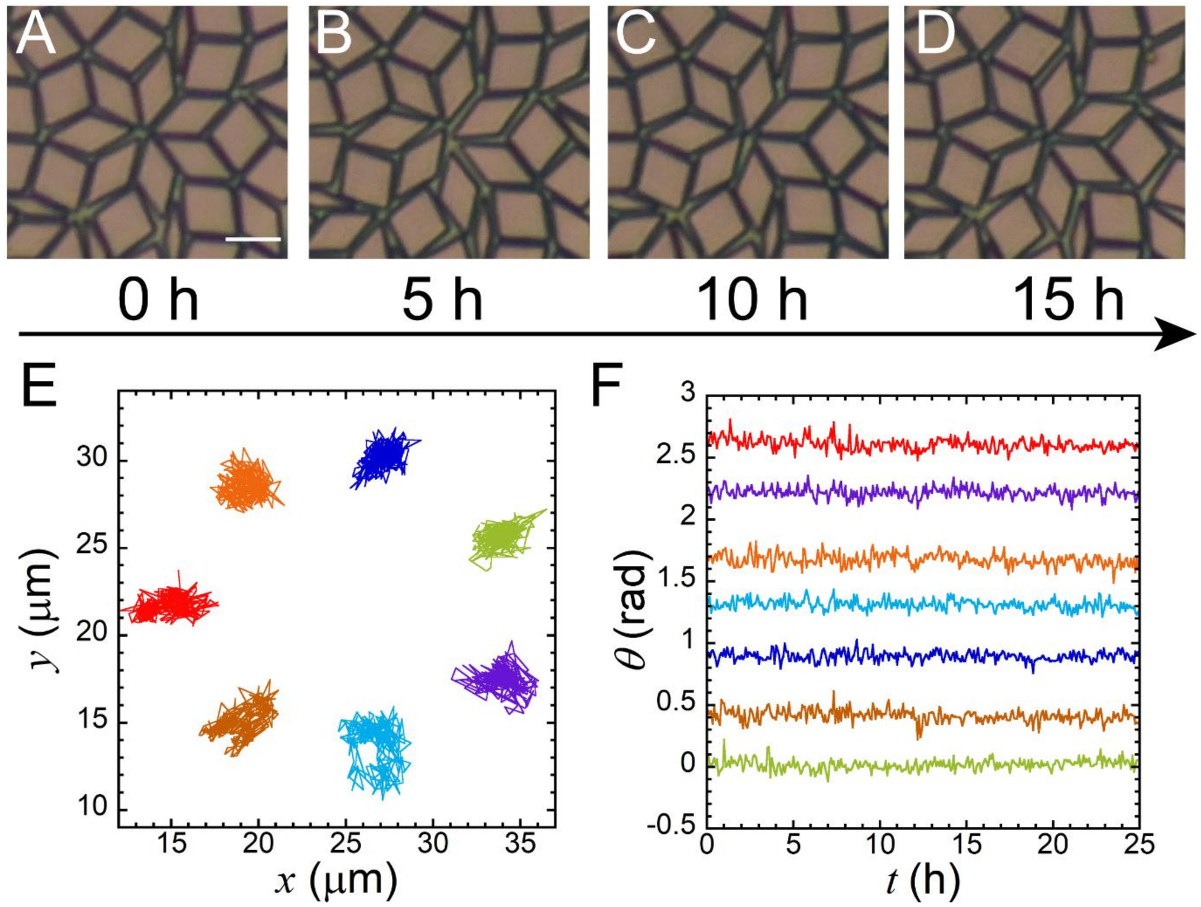

Figure 4. 10. Collective rotation of a non-corrugated, ellipse-like motif at ϕ_{high}. (A)-(B) Collective rotation of tiles in the motif encompassed by yellow dashed line. White arrow indicates rotation direction. Scale bar: 10 μm (white). (C)-(D) Trajectories of centers and orientations of each type-2 tile, using the same color as in (A)-(B). These tiles inside the motif undergo significant displacement compared with neighboring ones. (E) One superstructure is made of one heptagonal star surrounded by other seven heptagonal stars. Those heptagonal stars need not be identical. White solid arrows denote the vector having distance r between superstructure centers. Yellow dashed arrows denote the vector from the center of the superstructure to the center of each surrounding motif, having motif superstructural angle θ. Scale bar: 50 μm (yellow). (F) $g_{\text{MSO-PCF}}(r)$ at different times. Long-range orientational order of superstructures of motifs largely stabilizes and persists in equilibrium after 48 hours of release. Continued loss of superstructural order can be attributed to collective motions that destroy the nearby motif symmetry even at high density.

nearby heptagonal star. This process of collective motif rotation and internal tile reconfiguration results from small local density fluctuations (**Movie 4.5**). As an example, we have digitally tracked the trajectories of type-2 tiles both inside (colored) and outside (gray) this ellipse-like motif (**Figs. 4.11C** and **4.11D**). Tiles near the outer edge of the ellipse-motif translate directionally in an arc over about 10 μm; whereas, those outside only

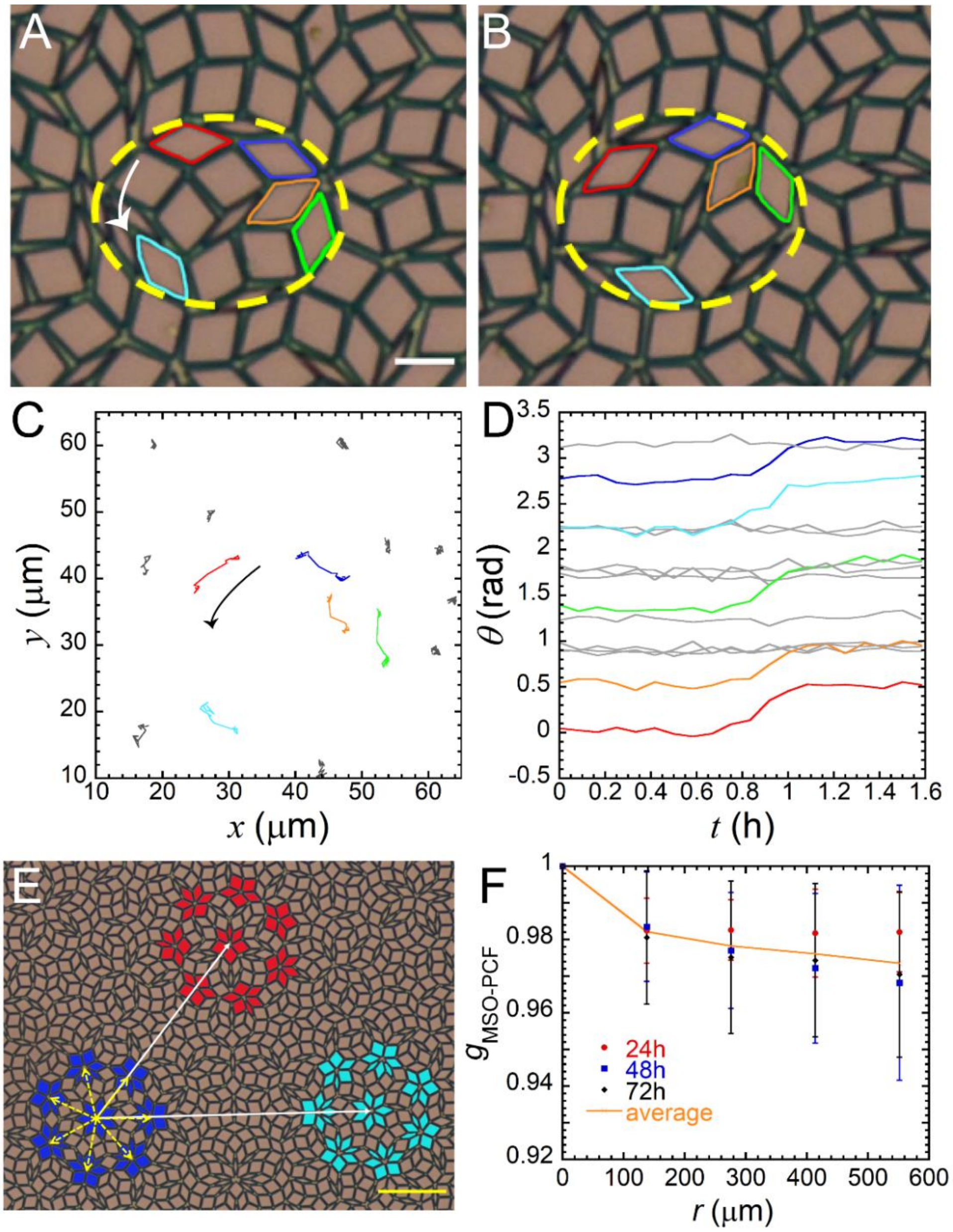

Figure 4. 11. Collective rotation of a non-corrugated, ellipse-like motif at ϕ_{high}. (A)-(B) Collective rotation of tiles in the motif encompassed by yellow dashed line. White arrow indicates rotation direction. Scale bar: 10 μm (white). (C)-(D) Trajectories of centers and orientations of each type-2 tile, using the same color as in (A)-(B). These tiles inside the motif undergo significant displacement compared with neighboring ones. (E) One superstructure is made of one heptagonal star surrounded by other seven heptagonal stars. Those heptagonal stars need not be identical. White solid arrows denote the vector having distance r between superstructure centers. Yellow dashed arrows denote the vector from the center of the superstructure to the center of each surrounding motif, having motif superstructural angle θ. Scale bar: 50 μm (yellow). (F) $g_{\mathrm{MSO\text{-}PCF}}(r)$ at different times. Long-range orientational order of superstructures of motifs largely stabilizes and persists in equilibrium after 48 hours of release. Continued loss of superstructural order can be attributed to collective motions that destroy the nearby motif symmetry even at high density.

undergo restricted random fluctuations within about 5 μm. Interestingly, orientations of these tiles after this collective motion approximately match the set of discretized values corresponding to their initial configurations. This indicates that the tiles immediately outside the ellipse-motif retain a memory of the initial 7-fold orientational alignments of the tiles in the QC pattern, leading to collective hopping behavior. This collective motion without cage breaking is only possible in multi-component, hierarchical systems, which partially account for the loss of long-range order, in addition to other mechanisms such as Mermin-Wagner fluctuations (38).

To quantify long-range orientational order of superstructures, we calculate $g_{\mathrm{MSO\text{-}PCF}}(r)$, where r is the distance between centers of two superstructures (white arrow, **Fig. 4.11E**). The motif superstrutural angle $\theta_{a,i}$ is associated with the orientation, relative to the horizontal axis in the lab frame, of the vector connecting the center of superstructure a and one motif i within this superstructure (yellow arrow, **Fig. 4.11E**). By adapting an equation for $g_{\mathrm{MSO\text{-}PCF}}(r)$ (31) to motifs and superstructures in the 7-fold system, we calculate $g_{\mathrm{MSO\text{-}PCF}}(r)$, which initially shows a small decay after release and nearly stabilizes after 48 hours (**Fig. 4.11F**).

4.3.5 Edge-proximity tessellation method for analyzing nearest neighbors

We construct polygonal cells based on edges of tiles, instead of centroids as in Voronoi analysis, to analyze the number of nearest neighbors of each tile. Equal distances between nearby edges of tiles (white lines, **Fig. 4.12A**) and the corresponding graph, which preserves the connectivity, are shown (**Fig. 4.12B**). In an ideally perfect 7-fold QC pattern, all tiles should have four nearest neighboring tiles. However, in the printed pattern, the edge lengths for different types of tiles are not the same as a consequence of digital design and

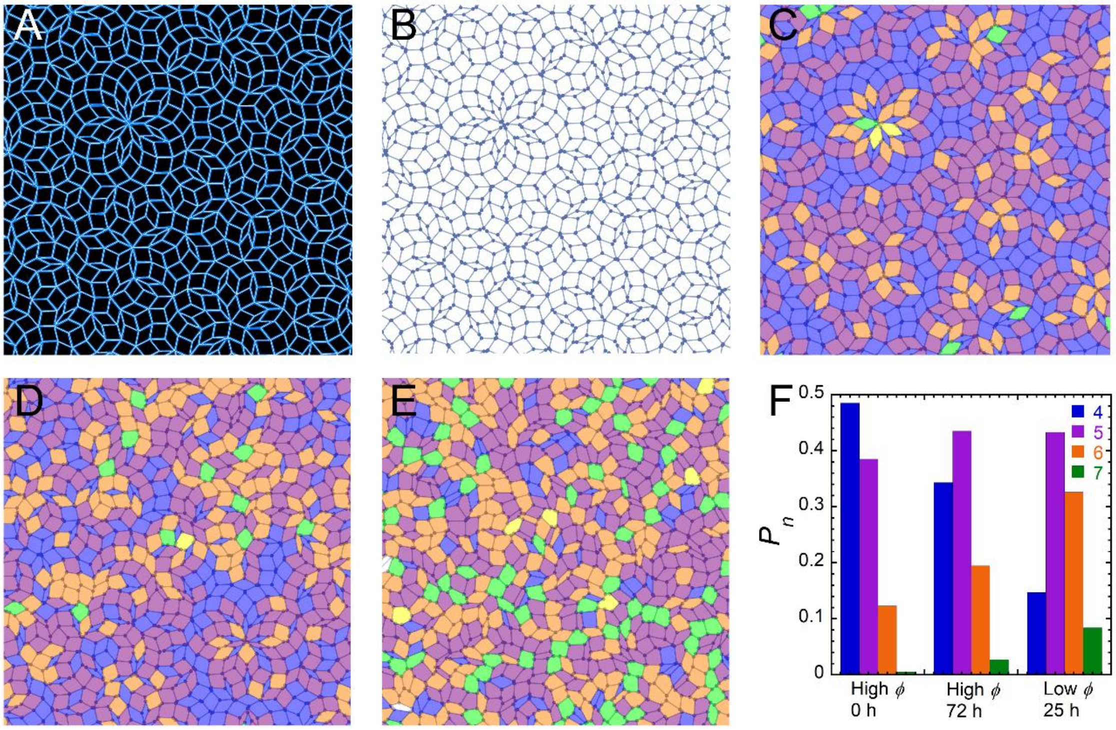

Figure 4. 12. Analysis and evolution of nearest neighbors after release through edge-proximity tessellation method. (A) Medial-axis of uncovered region having equal distance to nearby tile edges. Tiles are reconstructed from calculated positions, orientations, and edge lengths through particle tracking. (B) Graph extracted from (A), preserving the connectivity of the network. (C) Each polygonal cell is colorized by the number of edges: 4-blue, 5-purple, 6-orange, 7-green, and 8-white. Very short edges are not counted. More 4-edged polygon cells are observed in the printed pattern before release. The sliding and rotation of tiles result in less tiles with four nearest neighbors but more tiles with 5, 6, and 7 nearest neighbors at (D) ϕ_{high} after 72 h release and (E) ϕ_{low} after 25 h release. (F) Fewer tiles having 4 nearest neighbors but more having 5, 6, 7 nearest neighbors are found in less ordered systems after release.

lithographic fabrication. Therefore, in the printed pattern before release, some tiles (~ 50%) can have five or six nearest neighbors, but their corresponding polygonal cells would have smallest edge lengths that are very short compared to the rest (**Fig. 4.12C**). After release, the translational and rotational displacement of tiles result in more five-, six-, or seven-edged polygonal cells (**Figs. 4.12D** and **4.12E**), showing a distinct evolution of local structures. The ratio of tiles having four nearest neighbors is correlated with the structural degree of order:

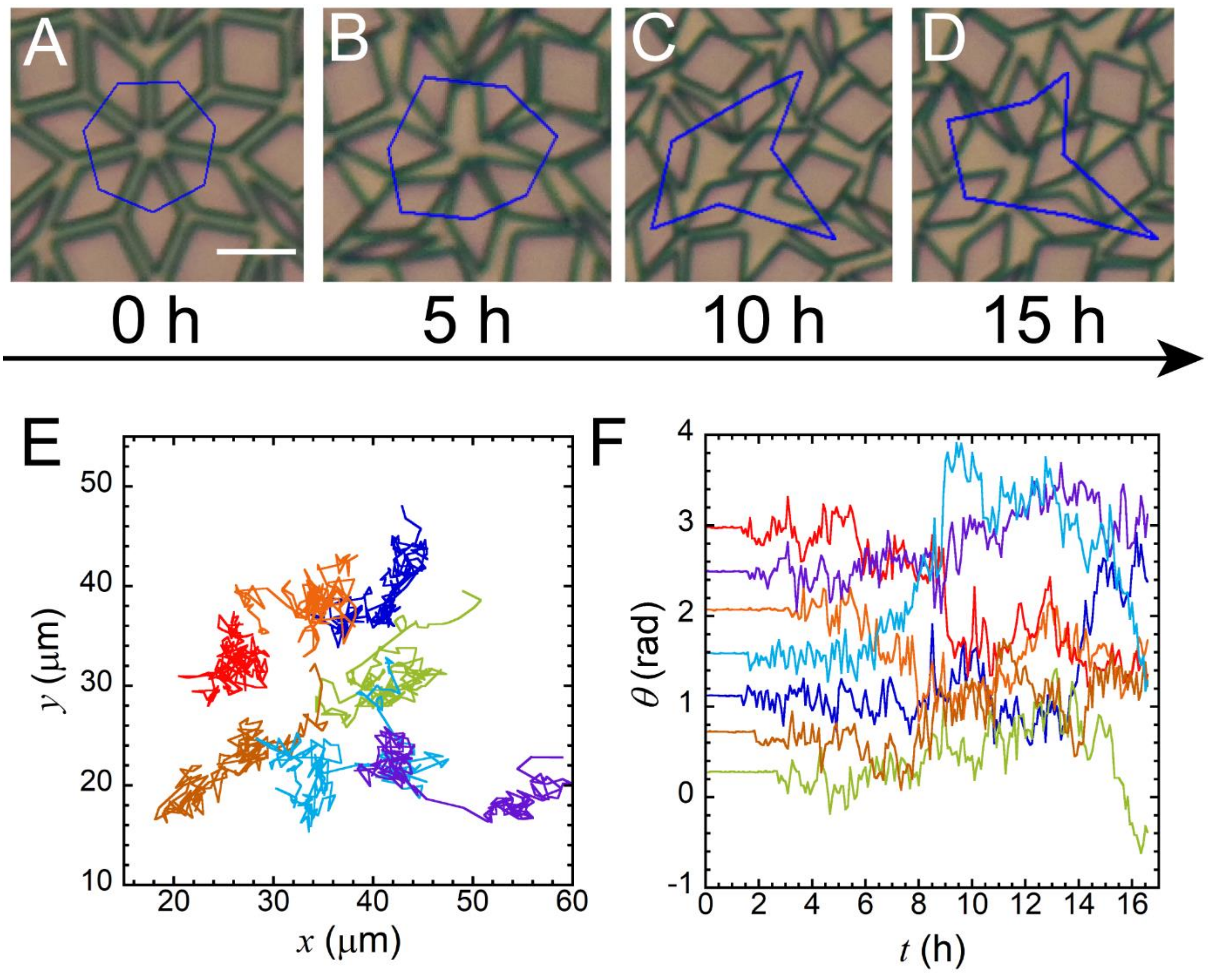

Figure 4. 13. Analysis of fluctuation and melting of a heptagonal star at ϕ_{low}**.** (A)-(D) Deformation of the star motif at t=0, 5, 10, and 15 h. Centers of each tile are connected by blue polygons. Scale bar: 10 μm. (E)-(F) Translational and orientational trajectories of each type-2 tile within the motif. Cross-overs happens and collective motion is not observed.

for ϕ_{high} at 72 hours, which is more ordered, more four-edged polygonal cells indicate greater structural order, as compared to fewer for ϕ_{low} at 25 hours (**Fig. 4.12F**).

We illustrate the frame-to-frame evolution of nearest neighbors of a heptagonal star for ϕ_{low} (**Movie 4.5**). For this low tile density, random fluctuations completely destroy the heptagonal star motif (**Figs. 4.13A-D)**. Overall, the average number of edge-proximate nearest neighbors increases during this process (**Movie 4.6**). Their trajectories of center positions and orientations indicate strong fluctuations up to 20 μm and 90°, respectively, far beyond the localized area of an individual tile (**Figs. 4.13E-F**). Also, $g_{\mathrm{MSO\text{-}PCF}}(r)$ at ϕ_{low} long after release cannot be obtained because motifs and superstructures are no longer recognizable.

4.4 Discussion and Conclusions

While self-assembly of shape-designed hard-interacting tiles by slow crowding has its own merits, such as the role of particle-shape in crystallization (45, 46), this method has limitations in rapidly forming large-scale, defect-free colloidal crystals, especially those having complex shaped, multi-component, or hierarchical structures. We have used litho-PAMs to overcome these limitations and fabricate a fluctuating 7-fold QC, which has a high degree of geometrical and structural complexity, in a top-down manner. This approach circumvents out-of-equilibrium jamming due to nearly degenerate ground states by slow crowding (15) and preserves a fixed and pre-configured area fraction over large regions for long durations. Litho-PAMs can be readily extended to other 2D pre-configured colloidal crystals or patterns, which would have other diverse phases, dynamics, hierarchies, and structures. Printing significantly smaller colloidal tiles, having faster Brownian dynamics, would also be feasible utilizing more advanced latest-generation lithographic equipment.

Although real-time observations down to atomic or molecular scales, such as grain boundary deformations (47) and glass transition (48), using aberration-corrected transmission electron microscopy (ac-TEM), have been reported in recent years, these examples require a conductive substrate and suffer from high electron beam damage. Therefore, further extension of real-time ac-TEM onto soft matter having non-trivial molecular shapes is experimentally challenging. The *in-situ* observation of colloidal tiles, which share structural similarities with molecular counterparts, by optical microscopy has enabled us to study dynamical and structural evolution in both equilibrium and non-equilibrium systems consisting of virtually any shapes of building blocks. It would be interesting to generate and study additional 7-fold QCs at different ϕ in order to create a comprehensive phase diagram. Also, 7-fold QCs composed of differently shaped tiles, other than the three rhombic tiles, would likely have different phase diagrams and different motif dynamics. Alternatively, other tile shapes, such as from 'shields', 'skates', and 'kites', could be used instead (49). While different 7-fold QC patterns would possess the same rotational symmetry irrespective of tile shapes, other 7-fold QC patterns would have very different motifs and superstructures of motifs, compared to the system we have studied that is based on three different rhomb tiles. Specifically, non-corrugated, purely convex motifs that can undergo collective rotation even at very high density, which are present in the 7-fold QC that we studied, are not present in some alternative 7-fold QC designs using other tile shapes. Also, avoiding slender shapes, such as type-3 rhombic tiles, would reduce the infrequent flipping or lift-off during Brownian motion and improve the fidelity of particle tracking.

Edge-proximity tessellation extends nearest neighbor analysis to a wide variety of non-compact shapes. In addition to the number of nearest neighbors, which is calculated from the number of edges in the corresponding polygonal cells, the effective contact length between nearest neighbors can also be calculated using the lengths of edges of the polygonal cells. Moreover, the average coordination number per tile evolves during the melting process (**Fig. 4.12F, Movie S6**). By contrast, according to KTHNY theory, 2D melting is mediated by dislocations and coordination number is conserved (50). Also, in the classic 2D hexagonal crystal having a six-fold coordinated lattice, dislocation pairs are composed of a five-fold coordinated point and a seven-fold coordinated point. Thus, our findings for the 7-fold system call for a broader theory of 2D phase transitions of crystals and quasi-crystals made from differently shaped building blocks, particularly building blocks that are non-compact.

In conclusion, we have used litho-PAMs to design and produce pre-assembled 2D 7-fold QCs having tunable area fractions. We have revealed a heptatic LQC phase reflecting the underlying 7-fold symmetry, and we have shown heterogeneous dynamics and order for different constituent particles and motifs, such as the collective rotation of ellipse-like motifs even at very high density. We have also developed an edge-proximity tessellation method based on tile edges, which is useful for analyzing nearest neighbors in systems of non-compact particles which undergo structural evolution, through processes such as fluctuations and melting. We anticipate that these findings will enrich the understanding of dynamic multi-component and hierarchical structures made from different building blocks of complex shapes.

Appendix B. Description for supplementary movies

Movie 4.1. Release and Brownian fluctuations of lower ϕ 7-fold QC. The crystalline structure is completely lost and the fluctuations are not restricted. Acquisition: 1 frame every 5 min. Acquisition time interval: 0 min – 1195 min (*i.e.* 239 frames) where 0 min corresponds to the addition of the RSD. Video playback: duration 23.9 s at 10 frames per second (FPS). Scale bar: 30 µm. Camera: Nikon Z7.

Movie 4.2. Equilibrium Brownian fluctuations of higher ϕ 7-fold QC. The crystalline structure is largely preserved and the fluctuations are highly restricted and localized. Acquisition: 1 frame every 5 min. Acquisition time interval: 4400 min – 6085 min (*i.e.* 337 frames). Video playback: duration 33.7 s at 10 frames per second (FPS). Scale bar: 30 µm. Camera: Nikon Z7.

Movie 4.3. Tracking the trajectories of different types of tiles. Two time periods are tracked separately: before 5 hours when tiles begin to release (**Figs. 4.9A-C**), and from 5 to 12.5 hours when all tiles are released and undergo Brownian fluctuations (**Figs. 4.9D-E**). Type-3 tiles are released first and have the largest mobility. Acquisition: 1 frame every 5 min. Acquisition time interval: 0 min – 1195 min (*i.e.* 239 frames). Video playback: duration 23.9 s at 10 frames per second (FPS). Scale bar: 20 µm. Camera: Nikon Z7.

Movie 4.4. Localized Brownian fluctuations of a heptagonal star motif in higher ϕ. This highly corrugated motif consisting of 7 type-2 tiles undergoes highly restricted Brownian fluctuations. The motif structure is preserved Acquisition: 1 frame every 5 min. Acquisition time interval: 4400 min – 6085 min (*i.e.* 337 frames). Video playback: duration 33.7 s at 10 frames per second (FPS). Scale bar: 10 µm. Camera: Nikon Z7.

Movie 4.5. Collective motion of an ellipse-like motif in higher ϕ. This non-corrugated motif undergoes collective motion without cage rearrangement even at high tile densities. The nearby heptagonal star motif is broken. Acquisition: 1 frame every 5 min. Acquisition time interval: 4800 min – 4900 min (*i.e.* 20 frames). Video playback: duration 2 s at 10 frames per second (FPS). Scale bar: 10 μm. Camera: Nikon Z7.

Movie 4.6. **Analysis of nearest neighbors through our new tessellation method**. This movie shows the evolution of nearest neighbors of the heptagonal star motif in **Movie 4.3**. Each polygon cell obtained from the new tessellation method is colorized by its edge numbers. During melting process, there are fewer tiles having 4 nearest neighbors but more tiles have 5, 6, or 7 nearest neighbors. Acquisition: 1 frame every 5 min. Acquisition time interval: 0 min – 685 min (*i.e.* 137 frames). Video playback: duration 13.7 s at 10 frames per second (FPS).

References

1. P. J. Steinhardt, D. R. Nelson, M. Ronchetti, Bond-orientational order in liquids and glasses. *Phys. Rev. B* **28**, 784-805 (1983).
2. D. R. Nelson, Orientational ordering in 2- and 3-dimensional systems. *J. Non-Cryst. Solids* **61-62**, 475-485 (1984).
3. B. I. Halperin, D. R. Nelson, Theory of two-dimensional melting. *Phys. Rev. Lett.* **41**, 121-124 (1978).
4. C. A. Murray, D. H. Van Winkle, Experimental observation of two-stage melting in a classical two-dimensional screened coulomb system. *Phys. Rev. Lett.* **58**, 1200-1203 (1987).
5. L. Onsager, The effects of shape on the interaction of colloidal particles. *Ann. N.Y. Acad. Sci.* **51**, 627-659 (1949).
6. K. W. Wojciechowski, D. Frenkel, Tetratic phase in the planar hard square system? *Comp. Met. Sci. Technol* **10**, 21 (2004).
7. K. Zhao, R. Bruinsma, T. G. Mason, Local chiral symmetry breaking in triatic liquid crystals. *Nat. Commun.* **3**, 801 (2012).
8. K. Zhao, R. Bruinsma, T. G. Mason, Entropic crystal–crystal transitions of brownian squares. *Proc. Natl. Acad. Sci. U.S.A.* **108**, 2684-2687 (2011).
9. C. Avendaño, F. A. Escobedo, Phase behavior of rounded hard-squares. *Soft Matter* **8**, 4675-4681 (2012).
10. A. P. Gantapara, W. Qi, M. Dijkstra, A novel chiral phase of achiral hard triangles and an entropy-driven demixing of enantiomers. *Soft Matter* **11**, 8684-8691 (2015).

11. Z. Hou, K. Zhao, Y. Zong, T. G. Mason, Phase behavior of two-dimensional brownian systems of corner-rounded hexagons. *Phys. Rev. Mater.* **3**, 015601 (2019).

12. J. A. Anderson, J. Antonaglia, J. A. Millan, M. Engel, S. C. Glotzer, Shape and symmetry determine two-dimensional melting transitions of hard regular polygons. *Phys. Rev. X* **7**, 021001 (2017).

13. Y. Zong, K. Zhao, Manipulation of self-assembled structures by shape-designed polygonal colloids in 2D. *Curr. Opin. Solid State Mater. Sci.* **26**, 101022 (2022).

14. K. Zhao, T. G. Mason, Assembly of colloidal particles in solution. *Rep. Prog. Phys.* **81**, 126601 (2018).

15. K. Zhao, T. G. Mason, Shape-designed frustration by local polymorphism in a near-equilibrium colloidal glass. *Proc. Natl. Acad. Sci. U.S.A.* **112**, 12063-12068 (2015).

16. Y. Zong, K. Chen, T. G. Mason, K. Zhao, Vibrational modes and dynamic heterogeneity in a near-equilibrium 2D glass of colloidal kites. *Phys. Rev. Lett.* **121**, 228003 (2018).

17. Z. Hou *et al.*, Emergent tetratic order in crowded systems of rotationally asymmetric hard kite particles. *Nat. Commun.* **11**, 2064 (2020).

18. K. Zhao, T. G. Mason, Frustrated rotator crystals and glasses of Brownian pentagons. *Phys. Rev. Lett.* **103**, 208302 (2009).

19. T. Schilling, S. Pronk, B. Mulder, D. Frenkel, Monte Carlo study of hard pentagons. *Phys. Rev. E* **71**, 036138 (2005).

20. D. Shechtman, I. Blech, D. Gratias, J. W. Cahn, Metallic phase with long-range orientational order and no translational symmetry. *Phys. Rev. Lett.* **53**, 1951-1953 (1984).

21. N. A. Wasio *et al.*, Self-assembly of hydrogen-bonded two-dimensional quasicrystals. *Nature* **507**, 86-89 (2014).

22. S. Fischer *et al.*, Colloidal quasicrystals with 12-fold and 18-fold diffraction symmetry. *Proc. Natl. Acad. Sci. U.S.A.* **108**, 1810-1814 (2011).

23. X. Zeng *et al.*, Supramolecular dendritic liquid quasicrystals. *Nature* **428**, 157-160 (2004).

24. T. M. Gillard, S. Lee, F. S. Bates, Dodecagonal quasicrystalline order in a diblock copolymer melt. *Proc. Natl. Acad. Sci. U.S.A.* **113**, 5167-5172 (2016).

25. R. Zhang, X. Zeng, G. Ungar, Direct AFM observation of individual micelles, tile decorations and tiling rules of a dodecagonal liquid quasicrystal. *J. Phys.: Condens. Matter* **29**, 414001 (2017).

26. K. Hayashida, T. Dotera, A. Takano, Y. Matsushita, Polymeric quasicrystal: Mesoscopic quasicrystalline tiling in *ABC* star polymers. *Phys. Rev. Lett.* **98**, 195502 (2007).

27. J. Zhang, F. S. Bates, Dodecagonal quasicrystalline morphology in a poly(styrene-b-isoprene-b-styrene-b-ethylene oxide) tetrablock terpolymer. *J. Am. Chem. Soc.* **134**, 7636-7639 (2012).

28. X. Zeng *et al.*, A columnar liquid quasicrystal with a honeycomb structure that consists of triangular, square and trapezoidal cells. *Nat. Chem.* 10.1038/s41557-023-01166-5 (2023).

29. D. V. Talapin *et al.*, Quasicrystalline order in self-assembled binary nanoparticle superlattices. *Nature* **461**, 964-967 (2009).

30. Y. Nagaoka, H. Zhu, D. Eggert, O. Chen, Single-component quasicrystalline

nanocrystal superlattices through flexible polygon tiling rule. *Science* **362**, 1396-1400 (2018).

31. P.-Y. Wang, T. G. Mason, A Brownian quasi-crystal of pre-assembled colloidal Penrose tiles. *Nature* **561**, 94-99 (2018).
32. R. Yamamoto, A. Onuki, Heterogeneous diffusion in highly supercooled liquids. *Phys. Rev. Lett.* **81**, 4915-4918 (1998).
33. A. Z. Patashinski, M. A. Ratner, B. A. Grzybowski, R. Orlik, A. C. Mitus, Heterogeneous structure, heterogeneous dynamics, and complex behavior in two-dimensional liquids. *J. Phys. Chem. Lett.* **3**, 2431-2435 (2012).
34. P. Zhang, J. J. Maldonis, Z. Liu, J. Schroers, P. M. Voyles, Spatially heterogeneous dynamics in a metallic glass forming liquid imaged by electron correlation microscopy. *Nat. Commun.* **9**, 1129 (2018).
35. I. Tah, A. Mutneja, S. Karmakar, Understanding slow and heterogeneous dynamics in model supercooled glass-forming liquids. *ACS Omega* **6**, 7229-7239 (2021).
36. E. R. Weeks, J. C. Crocker, A. C. Levitt, A. Schofield, D. A. Weitz, Three-dimensional direct imaging of structural relaxation near the colloidal glass transition. *Science* **287**, 627-631 (2000).
37. S. Belli, A. Patti, R. van Roij, M. Dijkstra, Heterogeneous dynamics in columnar liquid crystals of parallel hard rods. *J. Chem. Phys.* **133** (2010).
38. N. D. Mermin, Crystalline order in two dimensions. *Phys. Rev.* **176**, 250-254 (1968).
39. J. M. Tarp, L. Angheluta, J. Mathiesen, N. Goldenfeld, Intermittent dislocation density fluctuations in crystal plasticity from a phase-field crystal model. *Phys. Rev. Lett.* **113**,

265503 (2014).

40. A. E. Madison, Tiling approach for the description of the sevenfold symmetry in quasicrystals. *Struct. Chem.* **28**, 57-62 (2017).

41. M. E. Rule (2020) Algorithms for rendering quasicrystal tilings.

42. T. Yu, T. G. Mason, Brownian lithographic polymers of steric lock-and-key colloidal linkages. *Sci. Adv.* **7**, eabg3678 (2021).

43. K. Zhao, T. G. Mason, Directing colloidal self-assembly through roughness-controlled depletion attractions. *Phys. Rev. Lett.* **99**, 268301 (2007).

44. J. D. Brock, R. J. Birgeneau, J. D. Litster, A. Aharony, Liquids, crystals and liquid crystals. *Phys. Today* **42**, 52-59 (1989).

45. P.-Y. Wang, T. G. Mason, Colloidal lock-and-key dimerization reactions of hard annular sector particles controlled by osmotic pressure. *J. Am. Chem. Soc.* **137**, 15308-15314 (2015).

46. P.-Y. Wang, T. G. Mason, Dimer crystallization of chiral proteoids. *PCCP* **19**, 7167-7175 (2017).

47. L. Wang *et al.*, Tracking the sliding of grain boundaries at the atomic scale. *Science* **375**, 1261-1265 (2022).

48. P. Y. Huang *et al.*, Imaging atomic rearrangements in two-dimensional silica glass: Watching silica's dance. *Science* **342**, 224-227 (2013).

49. T. P. Schaad, A minimal 7-fold rhombic tiling. *arXiv preprint arXiv:2006.03453* (2020).

50. D. R. Nelson, B. I. Halperin, Dislocation-mediated melting in two dimensions. *Phys.*

Rev. B **19**, 2457-2484 (1979).

Chapter 5 – Summary

In this dissertation, we have studied pre-assembled colloidal polymers and quasi-crystals fabricated by litho-PAMs. These new types of materials, assembled from customized building blocks, have diverse morphologies and structures that are not accessible in molecular counterparts. Real-time visualization of Brownian fluctuations, using optical microscopy and a high-resolution camera, enables particle tracking down to even sub-monomer scale, thereby providing precise spatio-temporal particle tracking for analyzing dynamical and structural evolution in both equilibrium and non-equilibrium processes. Through simulations, we have also explored polylithomers having a broader range of lock-and-key linkages than in prior experiments. Our findings and discoveries provide new insight into and elucidate new relationships between shapes of mobile interacting building blocks and the corresponding properties of pre-assembled colloidal materials composed of these shapes.

Our studies of lock-and-key polylithomers, coupled together by purely hard in-plane steric interactions, have revealed how bond extensibility and chirality can affect conformations and statistical properties of Brownian colloidal linkages. We demonstrate the versatility of this method by fabricating diverse polymer structures, such as highly branched polymers dendrimers, crosslinked chiral spirals, and 2D meshes that mimic and go beyond what have been previously synthesized in either molecules or colloids. We have extended the scope of litho-PAMs to create self-integral polylithomer structures that are long-lived, free-standing, pre-configured assemblies without the need for any external confining wall. Also, we have studied the shape-related equilibrium bonding properties by tuning bond extensibilities and chiralities. We have also demonstrated the potential of litho-PAMs for studying far-from-equilibrium colloidal systems by creating and studying the dynamical evolution of chains having no intrinsic curvatures from a highly curved initial conformation.

Second, we have implemented MC simulations of polylithomers having more diverse lock-and-key bonds in order to explore broader range of unusual polymer behavior and properties, which would be very difficult to access with low defects and high yield through molecular synthesis. We show that the properties of equilibrium chains are closely related to the design of the monomers in a foreseeable and customizable manner. The results we present not only enhance models and theories about polymers, but also establish a possibility for analyses of molecular and colloidal complexes which have properties that depend on core-shapes of constituent building blocks. We show that bifurcated-cavity bonds contribute to increased fluctuations in local curvature, which can be measured by a more rapid increase in the orientational standard deviation. We also highlight how chirality, emerging from the geometrical constraints of specific lock-and-key bond designs, can have a significant influence on more frequent coil-like conformations and chain extensibilities as well as lead to negative orientational correlation functions. As a result, we have refined the conventional analysis for calculating persistence length by deducting the average accumulated angle. This is an improved analysis procedure that would work even when the chirality of the bond is unknown and only an ensemble of conformations is known.

Third, we extend the previously established litho-PAMs protocol to construct a novel 7-fold QC pre-assembled composed of three types of rhombic lithographic colloidal tiles. Once released, these tiles become mobile, and at sufficiently high tile densities, we have shown that this 7-fold QC becomes a novel heptatic liquid quasi-crystal phase under equilibrium Brownian fluctuations. Moreover, this 7-fold symmetric LQC contains diverse motifs and superstructures and exhibits heterogenous dynamics and order for different types of rhomb tiles at different length scales. In particular, we have experimentally revealed the collective motion of motifs without cage rearrangement, which could account at least in part for the decay in this system's spatial order even at high particle densities. Methodologically, we have developed a new tessellation diagram applicable to any arbitrary shapes to examine the evolution of nearest neighbors; this new approach is appropriate for dense systems of particles having complex shapes and thus goes beyond conventional Voronoi analysis. We believe that this approach will be useful in future theories that explain 2D phase transitions of systems consisting of building blocks having rich geometrical complexity.